

# **THERMAL CONDUCTIVITY AND CHARACTERISTICS OF COPPER FLASH SMELTING FLUE DUST ACCRETIONS**

Doctoral Thesis

Dissertation for the degree of Doctor of Science in Technology to be presented with due permission of Faculty of Chemistry and Materials Sciences, Helsinki University of Technology for public examination and debate in Auditorium V1 at Helsinki University of Technology (Espoo, Finland) on December 5<sup>th</sup> 2008, at 12 o'clock noon.

**Miettinen Elli**

Helsinki University of Technology  
Faculty of Chemistry and Materials Sciences  
Department of Materials Science and Engineering

Teknillinen korkeakoulu  
Kemian ja materiaalitieteiden tiedekunta  
Materiaalitekniikan laitos

Distribution:

Helsinki University of Technology

Laboratory of Materials Processing and Powder Metallurgy

P.O. Box 6200

FIN-02015 TKK, Finland

Available in pdf-format at <http://lib.tkk.fi/Diss/>

Cover: Cross sectional SEM-image of flue dust, SEM-image of flue dust accretion, flue dust accretion sample near boiler tube wall, Anter Flashline 5000 measurement device CSIRO

Minerals

© Elli Miettinen

ISBN 978-951-22-9561-6

ISBN 978-951-22-9562-3 (electronic)

ISSN 1795-0074

Multiprint Oy  
Helsinki 2008

---

## ABSTRACT

In Copper Flash Smelting, flue dust can cause severe problems in the gas handling system, which typically consists of a heat recovery boiler and electrostatic precipitator. If the process is not operated properly, the flue dust may form accretions on the boiler wall, reducing boiler heat transfer and subjecting the surfaces to corrosion. Flue dust accretions on heat recovery boiler tube walls have a reducing effect on the heat transfer efficiency of the boiler. No previous data on the thermal conductivity of metallurgical dust accretion layer have been published and it is the main focus of this work to provide these data. This work also focuses on the physical and chemical characterisation of the accretions and understanding their formation mechanism. The results can be used in the dimensioning of metallurgical heat recovery boilers and they also provide accurate input data for process models.

Flue dust accretions, loose process flue dust, and their pure chemical components were characterised and their thermal transportation properties were determined through experimental research. Flue dust particles were found to consist of two layers: oxides of copper and iron in the core of the particles and sulphate layers on the surface. The sulphation reactions take place in the atmosphere of the heat recovery boiler and are believed to participate in the accretion formation mechanisms. Sulphate bridges found between the flue dust particles in the accretions suggest that the sulphate phase is the binding component that results in the formation of accretions. Dust accretions consist of several layers possessing varying particle sizes, densities, and thermal properties. The initial deposition of fine particles takes place through thermophoresis or condensation, after which larger particles are able to deposit by sedimentation or inertial impaction. Sufficient time and temperature exposure results in the sintering and condensation of the layer structure and species migration and recrystallisation, resulting in higher density and thermal conductivity of the layer.

The thermal diffusivities and thermal conductivities of flue dust accretions, particulate samples of process dust, and pure chemical sulphates were determined. All the samples can be regarded as effective thermal insulators with thermal conductivity values of less than 2 W/mK for fused deposit and less than 0.7 W/mK for porous samples. The thermal diffusivity values for all samples were less than 0.005 cm<sup>2</sup>/s. Thermal diffusivity values show a decreasing temperature dependence, but an increase in the temperature dependence of the specific heat capacities results in slightly increased values for the thermal conductivity of the flue dust accretions. The particulate samples show slight decreasing temperature dependence for the thermal conductivity values, which is typical of crystalline structures. All the samples have thermal transportation values of the same order of magnitude and also resemble the values of the literature data on similar fouling layers found in other processes, indicating that chemical composition may not significantly affect the thermal properties of fouling layers. Porosity may be regarded as a fairly good indicator of the thermal transport efficiency of these types of materials, but the material microstructure must also be considered.

Keywords: thermal conductivity, thermal diffusivity, accretion formation, flue dust, flash smelting, heat recovery boiler

---



---

## PREFACE

The research work of this thesis was carried out in the Laboratory of Materials Processing and Powder Metallurgy, Helsinki University of Technology during the years 2003-2008 and at CSIRO Minerals, Clayton Australia during the year 2006.

I am deeply grateful to my supervisor, Professor Michael Gasik, and for all his help during the course of this study. My gratitude towards Professor Pekka Taskinen goes beyond words; his constant support and kind advice over the years have helped me enormously. His expertise in the field has been a great source of learning and a great professional inspiration for me.

I would like to thank the staff of the Laboratory of Materials Processing and Powder Metallurgy at Helsinki University of Technology for a pleasant working atmosphere and for all their help in conducting the experiments of this research: Laura Stykki; Markus Rouvinen; Kyösti Vänskä; Iina Kainulainen; Matti Vaajamo; Tuomo Kuikka; Ari Kruskopf; Mikael Friman; Kaija Pehkonen; Jorma Laine, and Tuomas Hirsi.

I would like to present my gratitude to CSIRO Minerals for enabling a part of this work to be conducted at their facilities in Clayton, Australia. I would also like to thank them for their help with the experiments and for their comments during the reporting of the results: Dr. Shouyi Sun; Dr. Sharif Jahanshahi; Dr. Steven Wright; Justen Bremmel; Mandie Matheson, and Rowan Davidson.

I am also very thankful to the Department of Materials Science and Engineering at Helsinki University of Technology for providing the facilities for this research and for the staff for all their help and support. I am especially grateful to Professor Heikki Jalkanen and Professor Lauri Holappa for their valuable comments and support and to Janne Vuori, Dr. Erkki Heikinheimo, and the workshop for their help with the experimental apparatus. I would especially like to thank my dear friend Lic. Sc. Mari Lundström for being my partner in combat, my support, a pair of listening ears and enormous help.

I want to thank Outotec for the financial support for this work. I would also like to thank CSIRO Minerals, the Finnish Cultural Foundation, the Outokumpu Foundation, and Tekniikan edistämissäätiö for their financial support.

I would like to thank my colleagues at Outotec for their comments and support and for providing wonderful role models: Dr. Tiina-Ranki-Kilpinen; Dr. Kim Fagerlund; Lic. Sc. Tero Kolhinen; Dr. Ilkka Kojo, and Dr. Ari Jokilaakso. Thank you also for Juha Järvi.

Neil Smith, Dr. Rob Stephens, and Dr. Caisa Samuelsson deserve my gratitude for their comments and the advice and help they have given me over the years.

My friends I love for their constant support and for all the fun and relaxing times within the past years that have enabled me to live life to the fullest, outside work too.

My very deepest gratitude goes to my husband Simo and my family for always believing in me, showing endless support and patience, and for letting me grow into the person I am.

Espoo, May 2008

Elli Miettinen

---

---

## TABLE OF CONTENTS

1. INTRODUCTION.....	1
1.1 Flue dust in Copper Flash Smelting .....	1
1.2 The objective of the study.....	1
2.THEORETICAL PART .....	1
2.1 Copper Flash Smelting flue dust .....	1
2.1.1 Dust formation.....	3
2.2 Previous characterisation studies on flue dusts.....	5
2.3 Heat transfer in porous media .....	9
2.4 Thermal conductivity of boiler deposits.....	18
2.5 The deposition mechanism of fouling layers.....	28
2.6 Discussion.....	38
3. EXPERIMENTAL .....	39
3.1 Characterisation of materials .....	39
3.1.1 Sample materials .....	39
3.1.2 SEM Characterisation .....	41
3.1.3 Particle size distribution.....	47
3.1.4 Particle density .....	49
3.1.5 TGA-DSC experiments.....	50
3.2 Equipment.....	53
3.2.1 Transient Plane Source .....	53
3.2.2 Laser Flash Analyser .....	55
3.2.3 Differential Scanning Calorimeter.....	57
3.3 Comparison of the measurement techniques .....	57
4. RESULTS .....	59
4.1 Thermal Diffusivity .....	59
4.2 Thermal Conductivity.....	62
4.3 Specific heat.....	67
4.4. Conclusions of the results .....	69
5. DISCUSSION .....	71
5.1 Flue dust deposition mechanism .....	71
5.2 Flue dust deposit thermal properties .....	73
5.2.1 The effect of porosity.....	74
5.2.2 The effect of temperature .....	76
6. CONCLUSIONS.....	81
REFERENCES .....	82

## LIST OF SYMBOLS

LATIN	UNIT
$A$ surface area	[m <sup>2</sup> ]
$a$ relative proportion of resistances	[-]
$B$ particle deformation factor	[-]
$C$ material-dependent constant	[-]
$C_p$ specific heat capacity	[J/gK]
$D$ material-dependent constant	[-]
$e$ coefficient of restitution	[-]
$k$ or $\lambda$ thermal conductivity	[W/mK]
$k_c$ reduced conductivity of core of unit	[W/mK]
$k_I$ thermal conductivity of phase I	[W/mK]
$k_{II}$ thermal conductivity of phase II	[W/mK]
$k_{2Ph}$ thermal conductivity of a composite	[W/mK]
$k_p$ relation between the conductivities of the dispersed and continuous phase	[-]
$k_s$ thermal conductivity of the solid phase	[W/mK]
$k_{II}$ thermal conductivity of a pore phase	[W/mK]
$k_{conv}$ heat conduction through convection	[W/mK]
$k_{eff}$ effective thermal conductivity	[W/mK]
$k_{rad}$ heat conduction through radiation	[W/mK]
$k_{II,g}$ heat conduction in the gas phase	[W/mK]
$k_{II,e}$ heat conduction by gas emission	[W/mK]
$k_{II,s}$ heat conduction in segregation and surface-diffusion processes	[W/mK]
$L$ thickness or distance	[m]
$M$ heat barrier resistance due to grain boundaries and micro cracks	[K/W]
$m$ mass	[g]
$n$ number	[-]
$P_0$ total output of power	[W]
$Q$ heat flow rate	[J]
$r$ radius of the spiral	[mm]
$R_f$ fouling thermal resistance	[cm <sup>2</sup> K/W]
$R(t)$ time-dependent resistance	[ $\Omega$ ]
$R_0$ initial electrical resistance	[ $\Omega$ ]
$\Delta T$ temperature gradient	[°C or °K]
$T$ temperature	[°C or °K]
$t$ time	[s]
$V$ volume	[m <sup>3</sup> ]
$V_{im}$ impact velocity	[m/s]
$x$ variable	[-]

---

**GREEK**

$\alpha$	thermal diffusivity
$\alpha_{eff}$	effective thermal diffusivity
$\alpha_t$	temperature coefficient of resistivity
$\theta_D$	Debye temperature
$\lambda_{2Ph}$	conductivity of packed bed
$\lambda_P$	conductivity of the dispersed phase
$\lambda$	conductivity of the continuous phase
$\xi$	sticking probability
$\tau$	dimensionless time
$\Pi$	porosity
$\rho$	density
$\rho_P$	particle density
$\rho_B$	bulk density
$\phi$	Maxwell parameter
$\psi$	bed porosity

**UNIT**

$[\text{cm}^2/\text{s}]$
$[\text{cm}^2/\text{s}]$
$[-]$
$[\text{°C or °K}]$
$[\text{W/mK}]$
$[\text{W/mK}]$
$[\text{W/mK}]$
$[-]$
$[-]$
$[\%]$
$[\text{kg/m}^3]$
$[\text{kg/m}^3]$
$[\text{kg/m}^3]$
$[-]$
$[\%]$



## **1. INTRODUCTION**

### **1.1 Flue dust in Copper Flash Smelting**

In Copper Flash Smelting, the process off-gas is cooled down and cleaned in gas-handling equipment consisting of a heat recovery boiler (HRB) and an electrostatic precipitator (ESP). In the HRB the heat is recovered by radiation and convection to the tube wall panels and then by conduction through the tube walls into water that circulates in the tubes. In the convection section of the boiler, heat is transported by the gas through convection and recovered by conduction through the tube walls. Thus, convection tube banks collect the remaining heat prior to ESP. The HRB is typically sized to reduce the process off-gas temperature from around 1400 °C as it enters the radiation section from the furnace to around 350 °C at the exit of the convection section. In addition to hot sulphur dioxide (SO<sub>2</sub>) containing gas, flue dust is also carried into the HRB. The dust must be separated from the gas before the gas is led into the acid plant for SO<sub>2</sub> recovery. As the dust cools down in the sulphur dioxide-rich atmosphere, it reacts to form metallic sulphates from metallic oxides and sulphides. The presence of the sulphates and the reactions of the dust cause severe problems in the boiler. If the dust forms build-ups on the boiler walls it may even block the route the gas passes through in the tube bundles in the convection section.

### **1.2 The objective of the study**

The aim of this work was to characterise different dust samples and dust deposits and to determine how effective the dust build-ups are as thermal insulators and to determine whether the dust layer on the boiler walls thus dramatically affects the heat transfer through the walls of the boiler. This work also focuses on characterising the accretion layers and determining their formation mechanisms.

## **2. THEORETICAL PART**

### **2.1 Copper Flash Smelting flue dust**

The Copper Flash Smelting process currently produces over a half of the world's primary sulphide-based copper. It is an autogenous process using sulphidic minerals such as chalcopyrite concentrate (CuFeS<sub>2</sub>) as feed materials. The reaction between the fine raw material particles and oxygen produces molten matte and slag droplets and releases sulphur dioxide gas. In the process the molten droplets then settle at the bottom of the furnace, forming a copper-rich matte and an iron-rich slag. The SO<sub>2</sub>-containing gas thus formed cannot be released into the atmosphere and is therefore transferred into a cleaning process before it is used in the manufacture of sulphuric acid. A schematic presentation of the process is shown in Figure 1.

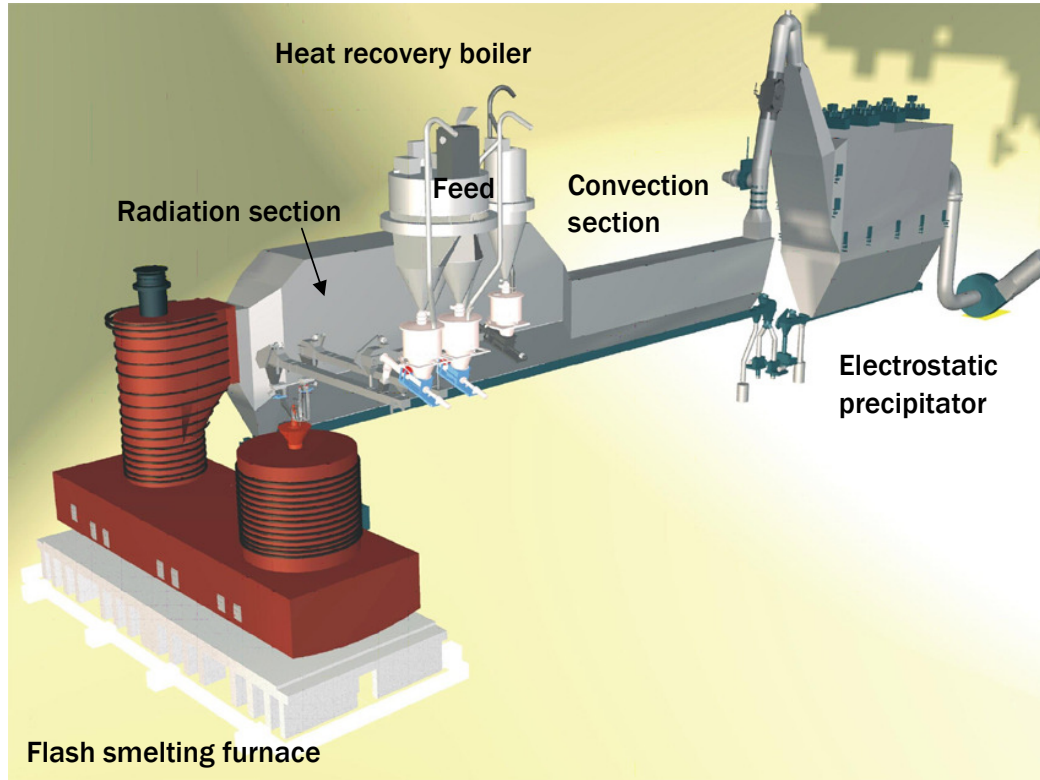


*Figure 1. Copper Flash Smelting Process (1)*

Between 3 and 15% of the feed material does not settle at the bottom of the furnace and is entrained in the process off-gas. The gas is treated to recover the heat value it contains and to separate the dust before the manufacturing of sulphuric acid. For this the gas is directed into a heat recovery boiler and an electrostatic precipitator. The heat is transferred by radiation and convection to the surface of tube wall panels and radiation screens, and conducted through the walls into high-pressure water circulating in the tubes. In the convection section of the boiler, heat is recovered by conduction into water containing tube banks. The temperature in the process off-gas cools down from around 1400 to around 350 °C. After the boiler the gas is directed into an ESP, where the rest of the dust particles are removed from the gas flow using an electric charge and associated electric field. A schematic illustration of a heat recovery boiler is shown in Figure 2.



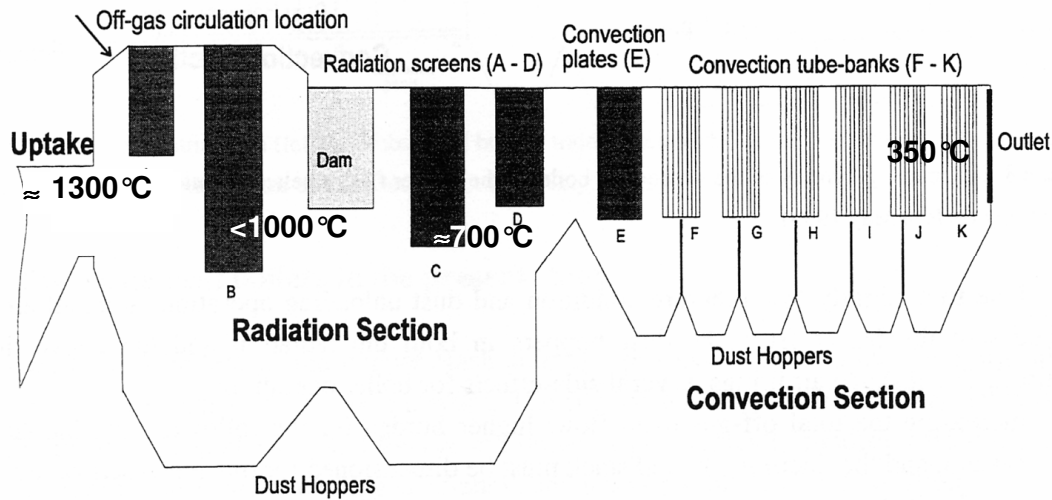


*Figure 2. Schematic illustration of a heat recovery boiler (2)*

The dust particles that enter the boiler with the gas consist mainly of metallic oxides, such as  $\text{Cu}_2\text{O}$  and  $\text{Fe}_3\text{O}_4$ . As the dust cools down in the  $\text{SO}_2$ -rich atmosphere, it reacts and forms metallic sulphates from metallic oxides. If the process is not properly operated, the reactions of the dust cause severe problems in the boiler. The dust forms build-ups on the boiler walls and may even block the route the gas passes through in the tube bundles in the convection section. Accretion layers on the tube walls may also significantly hinder the heat transfer through the walls. It is desirable that the sulphation reactions take place in the radiation section of the boiler, before the dust particles come into contact with the boiler walls. The sulphation reactions are highly exothermic and may cause overheating if they commence in the ESP.

The dust build-up on the walls consists of joined dust particles that form porous layers of material. Fouling of the boiler requires it to be cleaned using methods such as hammering and soot-blowing, or in severe cases even microblasting. Fouling and blockage problems in the boiler cause serious problems in the whole process and often the cleaning procedure requires a shut-down of the entire process. Understanding the accretion formation process and the characteristics of the dust may help in reducing the problems and in optimising the process. Knowledge of the characteristics of the dust can also be used in modelling the process more accurately.

### 2.1.1 Dust formation

Two kinds of dust forms are present in metallurgical smelting processes (3). Mechanically-formed dust consists of small particles of the charging material that get carried away with the process gas. Chemically-formed dust consists of vaporised components that condense into particles as the process off-gas temperature cools down.

Mechanical dust forms as a result of the entrainment of small solid and/or liquid particles from charged material into process off-gas (4). Mechanical entrainment involves the

elutriation by the process gas of small solid and liquid particles that travel at a relatively high velocity through the process (5). Process reactions can cause the charging material to disintegrate or fragment into smaller dust particles (6). The amount of mechanical dust in the process depends on:

- the particle size distribution of the charged material;
- the charging system, and
- the design of the reactor, which influences the gas velocity and gas path (4).

Chemical dust formation is caused by the vaporisation of components from the process, followed by the condensation of the components from the process gas at lower temperatures in the off-gas system (4). The amount of chemical dust generation depends on:

- the temperature of the process;
- the composition of the raw material, and
- the composition of the gas and the cooling of the gas (4).

Materials with a low melting point, such as As, Sb, and their oxides and sulphides, often have high vapour pressures and tend to vaporise in smelting, forming chemical dust. Chemical dust has a very fine particle size because of the nucleation and growth processes occurring as the process off-gas cools down. It may also condense on the surface of larger, mechanically-formed particles. In copper smelting processes, easily volatile components include Ag, As, Pb, Sb, and Zn. Figure 3 demonstrates the effect of temperature on element vaporisation. Copper can also vaporise in the hot combustion zone of the furnaces. Oxygen enrichment increases the combustion temperature in the flash furnace and, as a result, more copper is vaporised, as shown in Figure 4. Vaporised copper particles are very fine and easily drift out of the furnace with the off-gas.

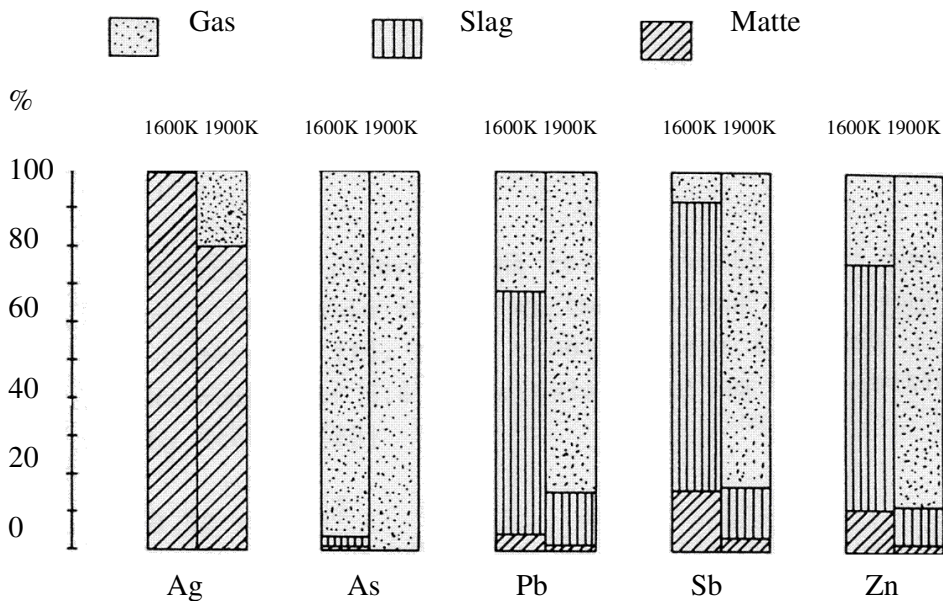
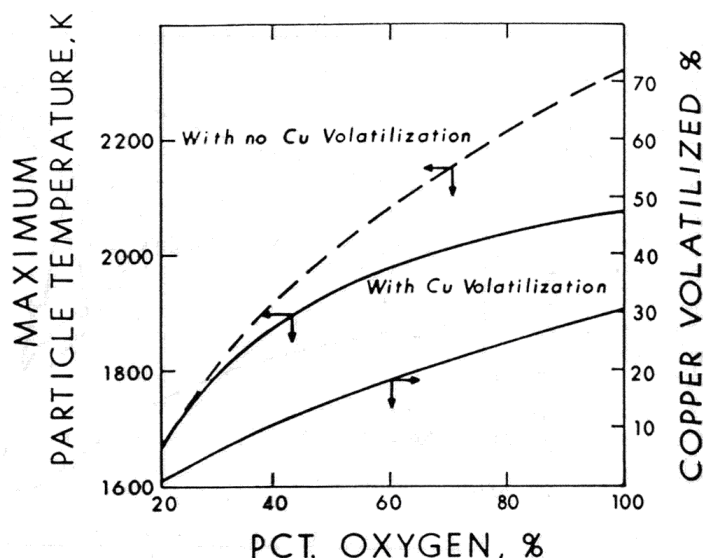


**Figure 3.** Distribution of several elements between gas, slag, and matte with 75% Cu at 1600K and 1900 K. (7)



Effect of oxygen concentration on the volatilization of copper during oxidation of  $45\text{-}\mu\text{m}$  chalcopyrite particles in a laminar-flow furnace.  $T_g = T_w = 1073\text{ K}$ ;  $d_p = 45\text{ }\mu\text{m}$ . The plot shows the change in maximum particle temperature due to the volatilization of copper.

**Figure 4.** Copper volatilisation as a function of oxygen amount in the blast (8).

Most dust particles follow the gas stream or fall to the bottom of the boiler without interacting with other particles or the boiler walls. The dust particles that do deposit on the walls experience a dramatic change in the environment. The wall is much cooler than the gas stream and the time scale for potential reactions is much longer than the normal residence time of the particles in the boiler. Deposited particles are also in close contact with other particles, providing the opportunity for an additional range of transformations. (9)

## 2.2 Previous characterisation studies on flue dusts

Swinbourne et al. (10) collected data from various dust build-up studies. Table 1 presents the composition of a few studied dust accretions:

**Table 1.** Dust Compositions

Smelter	Furnace	Location	Cu	Fe	Pb	Zn	As	S	SiO <sub>2</sub>
Kosaka	flash	uptake	10-20	31-42	2-3	7-9		6-9	4-7
		boiler	18-21	22-25	8-12	8-9		7-9	3-4
		ESP	12-14	10-12	15-19	9-14		9-10	1-1.5
Kosaka	flash	boiler	12.6	11.6	15.9	7.9	1.7	9.0	
		ESP	10.2	8.9	21.6	2.7	9.3		
Kennecott	flash	ESP	28.7	19.9	0.8	0.9	1.7	7.4	8.4
Naoshima	Mitsubishi	boiler	44.1	7.1	3.4	2.0	1.7		
		ESP	14	3	10	4	2.7		
Kidd Creek	Mitsubishi	ESP	10.6	6.0	26.2	21.3	1.8		

In the Kosaka flash furnace uptake shaft, hard, dense accretions consisting of magnetite (Fe<sub>3</sub>O<sub>4</sub>) crystals along with zinc ferrite (ZnO·Fe<sub>2</sub>O<sub>3</sub>) cemented by Cu<sub>2</sub>S matte were reported.

## THEORETICAL PART

In the radiation section of the HRB, grey-black  $\text{Cu}_2\text{S}$ -PbS matte and lead silicate glass were present, along with magnetite crystals. Accretions in oxidising conditions consisted of metallic copper,  $\text{CuO}_{0.5}$ , copper ferrites, and magnetite. In lower-temperature sections lead sulphate was also observed. In the other parts of the process off-gas system, reddish dust containing hematite ( $\text{Fe}_2\text{O}_3$ ) and Cu, Pb, and Zn sulphates was found.

In the Naoshima Mitsubishi smelting furnace off-take, the build-up consisted mainly of Cu, Pb, and Zn sulphides. In the HRB half of the Cu was present in sulphate form, with the rest as Cu oxides and sulphides. In the ESP all of the Cu, Pb, and Zn were in sulphate form. Similar results were also reported for the Kennecott ESP.

In the Kidd Creek Mitsubishi smelting furnace uptake, Cu and Pb sulphates, along with Zn ferrites, were the main components of the accretions. The boiler dust was reported to contain Cu, Pb, and Zn sulphates, Cu oxides, and ferrites. ESP dust consisted of  $\text{PbSO}_4$ , ZnO,  $\text{Cu}_2\text{O}$ ,  $\text{ZnO}\cdot\text{Fe}_2\text{O}_3$ ,  $\text{Cu}_2\text{O}\cdot\text{Fe}_2\text{O}_3$ , and  $\text{Cu}_3\text{As}$ .

Markova et al. (11) reported that the HRB dust of a Bulgarian flash smelter contained mainly oxides ( $\text{Fe}_3\text{O}_4$ ,  $\text{Fe}_2\text{O}_3$ ,  $\text{CuFe}_2\text{O}_4$ ,  $\text{CuFeO}_2$ ,  $\text{Cu}_2\text{O}$ ) and sulphates of Cu and Fe, along with some Cu and Fe sulphides and Fe silicates. The samples from the convection section of the boiler contained fewer sulphides and more sulphates than the radiation section sample, as indicated in Figure 5.

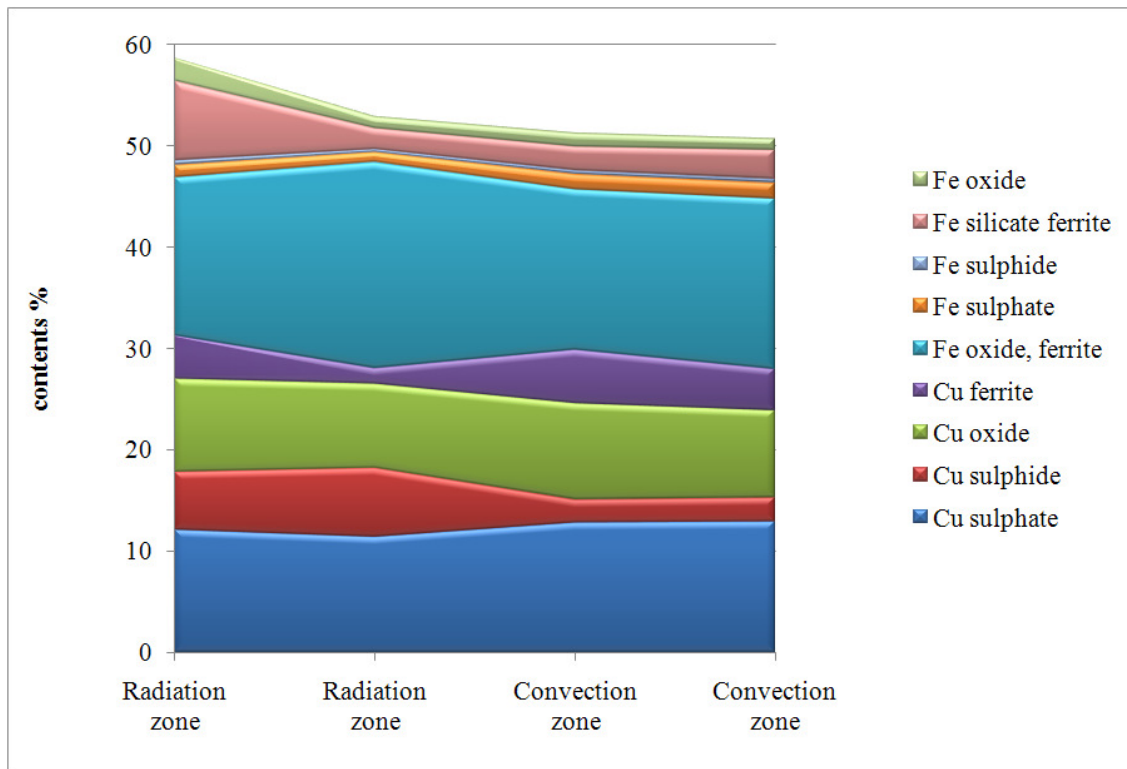


**Figure 5.** Dust composition in heat recovery boiler radiation section and convection section of Bulgarian flash smelter. (11)

Cu sulphate represented approximately 38-45% of the total copper amount,  $\text{Cu}_2\text{O}$  around 30%, and  $\text{CuS}$  represented around 10% of the total copper. 72-78% of the Fe was present in the magnetite and in the ferrite phases.

Samuelsson (4) reported a composition of sulphides ( $\text{CuFeS}_2$ ,  $\text{Cu}_5\text{FeS}_4$ ,  $\text{ZnS}$ ,  $\text{PbS}$ ,  $\text{FeS}$ ), with magnetite ( $\text{Fe}_3\text{O}_4$ ) and ferrites ( $\text{Cu}$ ,  $\text{Zn}$ ) $\text{Fe}_2\text{O}_4$  from the ESP of the Rönnskär roasting furnace. In the electric smelting furnace, dust oxides ( $\text{CuO}$ , ( $\text{Cu}$ ,  $\text{Zn}$ ) $\text{Fe}_2\text{O}_4$ ,  $\text{Fe}_3\text{O}_4$ ) and sulphates ( $\text{PbSO}_4$ ,  $\text{CuSO}_4$ ,  $\text{ZnSO}_4$ ) were found. Converter dust consisted of sulphates ( $\text{PbSO}_4$ ,  $\text{CuSO}_4$ ,  $\text{ZnSO}_4$ ),  $\text{ZnO}$ , and  $\text{Cu}_2\text{S}$ . Settling furnace dust contained  $\text{ZnO}$ ,  $\text{PbSO}_4$ , Fe oxides, Cu-Fe sulphides, and metallic phases. The dust from the roasting and smelting operations consisted mostly of mechanically-formed dust, whereas the converting and settling furnace dusts contained a larger portion of chemically-formed dust with fine particle size.

Kurosawa et al. (12) reported  $\text{Fe}_3\text{O}_4$ ,  $\text{PbSO}_4$ ,  $\text{Cu}_2\text{S}$ ,  $\text{Cu}_2\text{O}$ ,  $\text{As}_2\text{O}_5$ , and  $\text{PbS}$  in the coarse grey-black boiler dust of the Ashio flash smelter. They also investigated dust from the downstream parts of the process and concluded that Pb, Zn, Bi, Sb, As, Sn, and In tend to vaporise and condense into small dust particles that are mainly carried into the process parts following the HRB.

Kim et al. (13) investigated the ESP dusts of the Noranda smelter and found Pb sulphate, sulphates, oxides, and ferrites of Zn and Cu as metal, basic sulphate and sulphide, Fe oxide, and silicate slag. Cu-rich particles were often associated with silicates and Fe oxide and had a Pb sulphate layer on the surface. As and Bi were often found near lead phases. Half of the Cu was in sulphate form, 5% as oxide, 15% as metal, and 30% as sulphide. The vast majority of the Pb and Zn was present in sulphates.

Whyte et al. (14) detected  $\text{Fe}_3\text{O}_4$ ,  $\text{Cu}_2\text{O}$ ,  $\text{SiO}_2$ ,  $\text{PbSO}_4$  and  $\text{ZnSO}_4$  in reverberatory furnace dust from the Miami smelter. They suggested that Pb and Zn sulphates are likely to have deposited on the surface of oxide particles through vaporisation and condensation.

Evans et al. (15) reported the compositions of dust from HRB following the Kidd Creek Mitsubishi smelting furnace. The compositions of the deposits on the boiler walls and in the gas stream are presented in Figures 6 and 7, respectively.

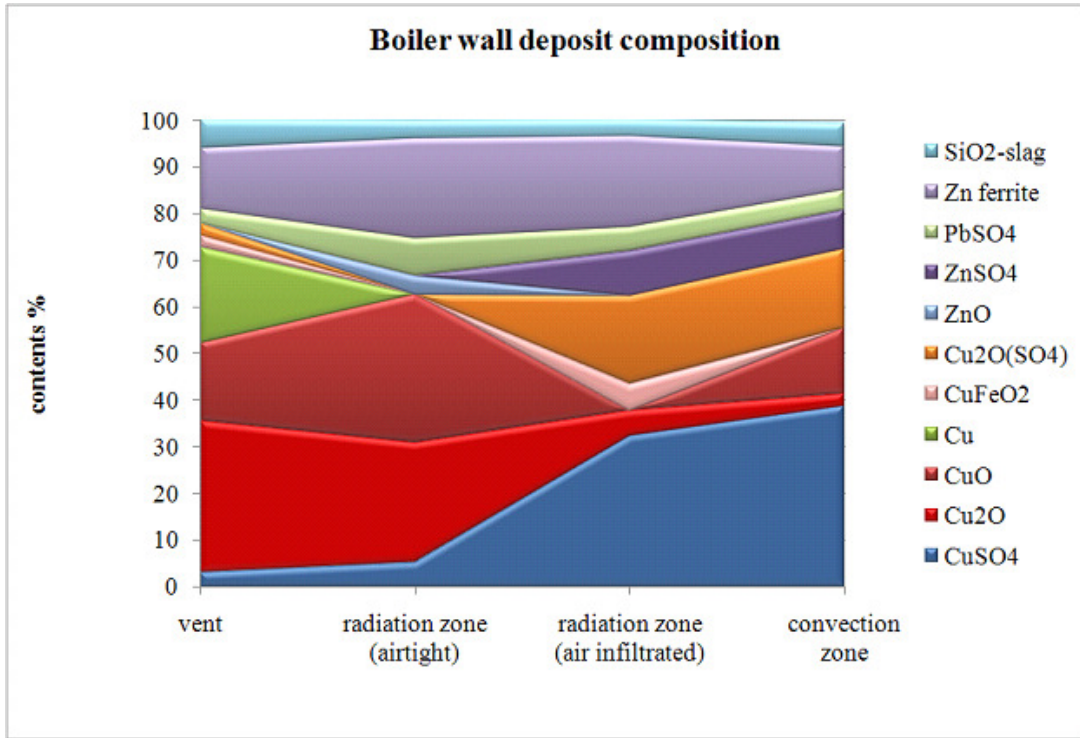


Figure 6. Composition of the boiler wall dust deposits in the Kidd Creek Mitsubishi smelter (15).

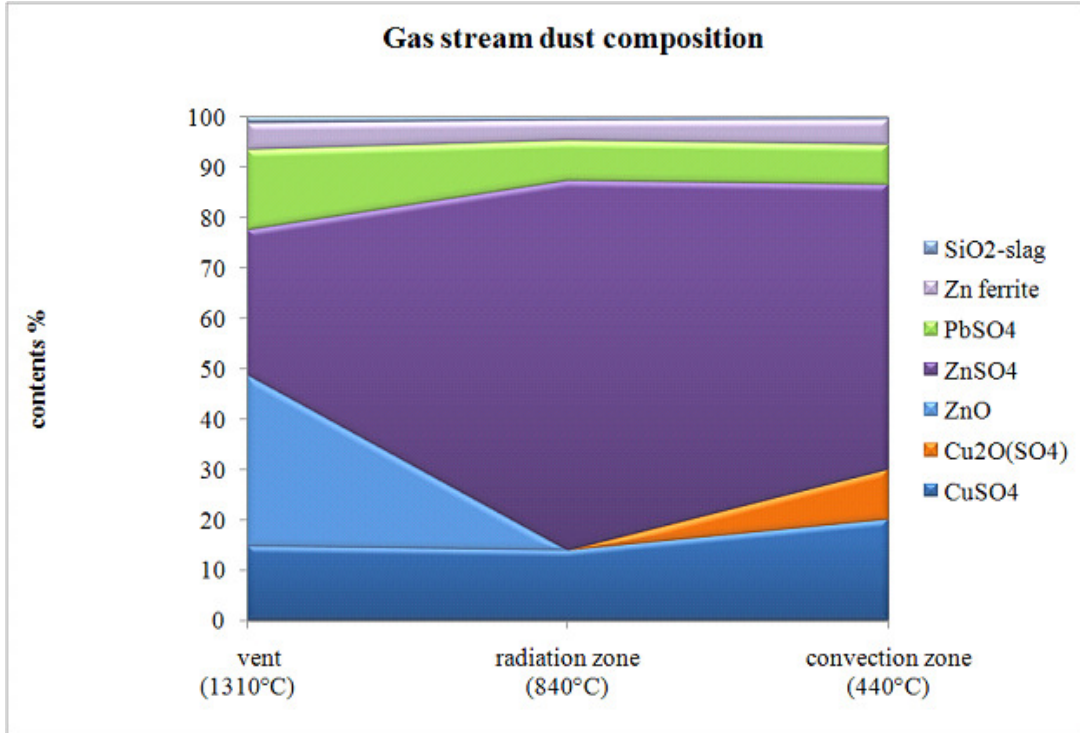
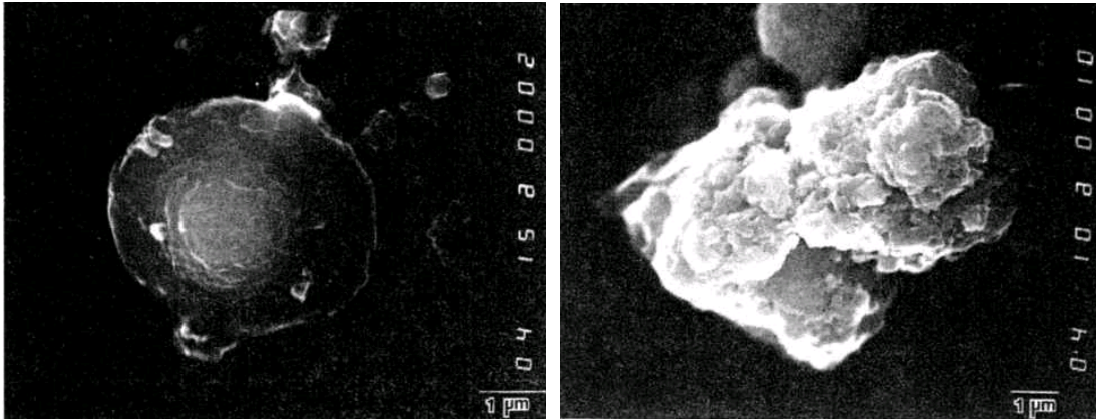


Figure 7. Composition of the gas stream dust deposits at Kidd Creek (15).



In both samples there is a clear shift from oxides to sulphates when the dust from the inlet of the HRB is compared to that at the outlet of the HRB.

Lastra-Quintero (16) et al. also investigated Kidd Creek Mitsubishi smelting furnace ESP dusts. They found two distinct morphologies in the dust particles; spherical and irregular slag-like. The spherical particles had a low Fe content, whereas the irregular particles were richer in Fe. Particles of both shapes also contained Cu, Pb, and Zn. Examples of the morphologies are presented in Figure 8.



*Figure 8. Spherical and irregularly-shaped dust particles from the Kidd Creek ESP. (16)*

Electron microscope observations showed a concentration of Fe towards the centre of the particle. All the particles were highly agglomerated and heterogeneous, indicating high gas temperatures leading to the fusion of components. It was suggested that solid Fe oxide may act as a reaction centre for Zn vapour and Cu liquid oxidation, resulting in ferrite formation. Phases such as  $\text{Fe}_3\text{O}_4$ ,  $\text{Cu}_2\text{O}$ ,  $\text{ZnO}$ ,  $\text{ZnS}$ ,  $\text{Cu}_2\text{OFe}_2\text{O}_3$ ,  $\text{ZnOFe}_2\text{O}_3$ ,  $\text{PbSO}_4$ , and  $\text{Cu}_3\text{As}$  were identified in the particles.

Kyllo et al. (17) detected two types of dusts from the samples of the Flin Flon reverberatory smelter, a coarser size originating from the furnace feed, containing solidified droplets of matte and flux and a finer size originating from condensed vapours, containing Pb, Zn, As and Cd.

Morales et al. (18) investigated flue dusts from a copper smelting furnace and detected magnetite ( $\text{Fe}_3\text{O}_4$ ), cuprospinel ( $\text{CuFe}_2\text{O}_4$ ), anhydrous copper sulphate ( $\text{CuSO}_4$ ), lead sulphate ( $\text{PbSO}_4$ ), and arsenic oxides ( $\text{As}_4\text{O}_6$ ) as major phases. Minor phases included zinc sulphate and several copper or copper/iron sulphides and copper oxide. The coarse fraction of leaching residue was copper-rich and the arsenic was enriched in the fine fraction.

## 2.3 Heat transfer in porous media

The dust build-up on the boiler walls consists of porous layers of joined particles and the heat transfer in the dust layer may thus be described by models that estimate the heat transfer in porous media. Porous material can be regarded as composites consisting of two phases, the solid and the gaseous.

The main material properties characterising the heat transfer of a medium are thermal conductivity and thermal diffusivity. Thermal conductivity,  $\lambda$  or  $k$  (W/mK), is the quantity of heat,  $Q$ , transmitted through a thickness  $L$ , in a direction normal to a surface of area  $A$ , resulting from a temperature gradient  $\Delta T$ , under steady state conditions and when the heat transfer is dependent only on the temperature gradient. (19)

Thermal conductivity = heat flow rate  $\times$  distance / (area  $\times$  temperature gradient)

$$k = QL / (A\Delta T) \quad (1)$$

Thermal diffusivity,  $\alpha$  (m<sup>2</sup>/s), is the ratio of thermal conductivity to volumetric heat capacity. Thermal diffusivity is the measure of the way heat flows through the material from the hot side to the cool side. It can also be expressed as the rate of change of temperature in a transient heat transfer process.

$$\alpha = (k/\rho C_p) \quad (2)$$

where

$k$  is thermal conductivity

Materials with high thermal diffusivity adjust fast to the surrounding temperature, because they conduct heat quickly in comparison to their thermal 'bulk'.

$\rho C_p$  is the volumetric heat capacity (density times specific heat capacity). The specific heat capacity,  $C_p$ , is the amount of heat per unit mass required to raise the temperature of the material by one degree Celsius. The required energy goes into:

- vibrational energy in which atoms vibrate around their lattice positions;
- rotational energy for molecules that have rotational degrees of freedom;
- raising the energy level of electrons, and
- changing atomic positions.

All of these correspond to an increase in configurational entropy. At low temperatures, the heat capacity is proportional to  $(T/\theta_D)^3$ , where  $\theta_D$  is the Debye temperature characteristic for each material. At higher temperatures, the heat capacity becomes independent of the temperature. Some typical values of heat capacity following the above representation are shown in Figure 9.



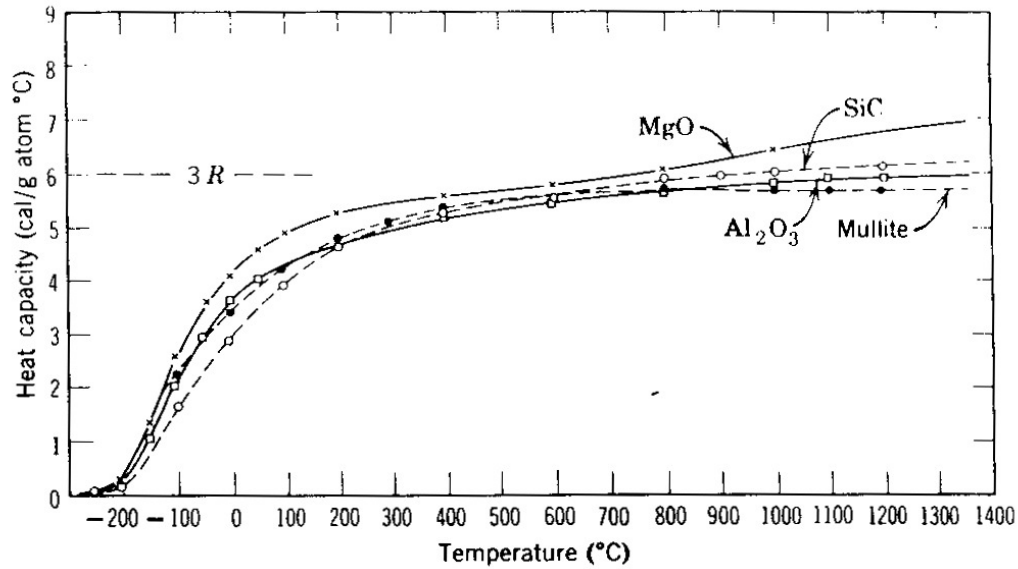


Figure 9. Heat capacity of some ceramic materials at different temperatures. (19)

Heat may be conducted in solid materials either by lattice vibrations (phonons) or, in the case of metals, also by electrons. In non-metallic solid materials, the main heat transfer method may be described as phonon-phonon interaction. At higher temperatures, usually above 500 °C, radiation (photon conductivity) becomes a significant heat transfer process. At low temperatures the phonon mean free path (the average distance between phonon collisions) becomes as large as the sample size and no heat is conducted (at 0 °K). The mean free path reaches a maximum at some point, after which it decreases until the value of lattice spacing and conductivity becomes temperature-independent (Debye temperature). Several factors influence the mean free path of the phonons. Lattice imperfections, grain boundaries, inclusions, pores, and complex crystal structures cause scattering of the lattice waves and thus lower the thermal conductivity of materials. (19)

A heterogeneous material consisting of a continuous phase and a dispersed phase may be viewed as an effective homogeneous medium, and an effective thermal conductivity value can usually be determined. The conductivity depends on the amounts, arrangement, and individual thermal conductivities of the various components. The thermal conductivity of a composite lies between the conductivities of the two components that make up the composite. In porous materials heat flows through both the gaseous and the solid phase. (20,21)

Materials consisting of separate particles have large heat-barrier resistances between the particles. This fact leads to low thermal transport values compared to dense materials with similar chemical compositions. In packed beds, the heat is transferred through solid particles, through gas, and via the contact points between the particles, which generally have a lower conductivity than the particles themselves. The classical models tend to overestimate the thermal conductivities of porous materials, since they do not take into account the micro- and macro-cracks and porous intergrain boundaries. Even though they contribute very little to the total porosity of the materials, they have a significant effect on the thermal resistance within the material. Other factors affecting the thermal conductivity of porous materials are intergrain surface diffusion and gas emission within the pores. (20-22)

There are several theoretical models for predicting the thermal conductivity of composite materials. The usual problem with most of the models is that they model very application-specific empirical data, an idealised microscopic structure, or macroscopic generalised engineering objects (23).

Three main types of heat transfer models have been reported in the literature (23):

**Type I**

The Laplace heat conduction equation is solved in and around particles and the respective temperature fields are obtained. From these, the heat fluxes and thermal conductivity of the system can be calculated. The solution method is schematically presented in Figure 10.

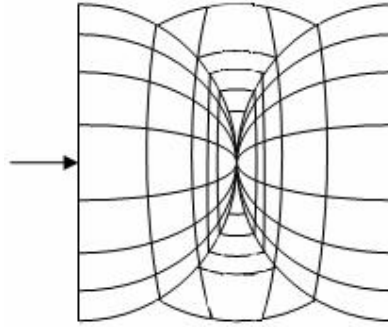


**Figure 10.** Type I heat transfer model, exact estimation of temperature profiles in each unit cell of the system. (23)

This method was originally developed by Maxwell (24). For dilute dispersion of spheres, the following is true:

$$\frac{k_{2Ph} - 1}{k_{2Ph} + 2} = (1 - \psi) \frac{k_p - 1}{k_p + 2} = \phi \quad (3)$$

where

$$k_{2Ph} = \lambda_{2Ph} / \lambda \quad \text{and} \quad k_p = \lambda_p / \lambda \quad (4,5)$$

$\lambda_{2Ph}$ =conductivity of packed bed,  $\lambda_p$ =conductivity of the dispersed phase,  $\lambda$ =conductivity of the continuous phase,  $\psi$  = bed porosity,  $\phi$ =Maxwell parameter

Rearrangement gives:

$$k_{2Ph} = \frac{1 + 2\phi}{1 - \phi} \quad (6)$$

This equation applies, in addition to dilute dispersions, to dense systems with moderate values of  $k_p$ . The addition of secondary parameters, such as radiative heat transfer and particle shape, often leads to labour-intensive calculations and convergence difficulties.

### Type II

In Type II models, the dispersed system is simulated by a combination of resistances, connected partly in parallel and partly in series, shown schematically in Figure 11.

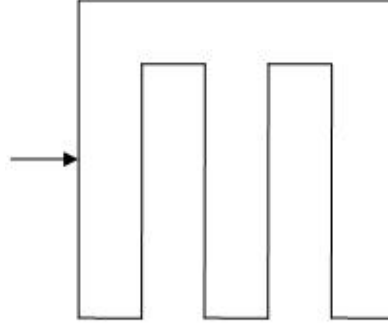


**Figure 11.** Type II heat transfer model, combination of resistances, connected partly in parallel, partly in series in order to simulate the behaviour of the binary compound. (23)

For systems having the same porosity but different conductivities, the relative proportion of resistances is  $a$ .

$$\frac{1}{k_{2ph}} = \frac{1-a}{k_1} + \frac{a}{k_{II}} \quad (7)$$

With

$$k_I = \psi + (1-\psi)k_p \quad (8)$$

$$k_{II} = \left( \psi + \frac{1-\psi}{k_p} \right)^{-1} \quad (9)$$

$$k_p = \lambda_p / \lambda \text{ and } k_{2ph} = \lambda_{2ph} / \lambda.$$

In the case  $a=1$ , maximal resistance is obtained and all the heat must pass through the poorly-conducting phase. In the case of  $a=0$ , the poorly-conducting phase can be completely bypassed.

### Type III

In Type III models, the thermal conductivity of a unit cell is assumed to represent the whole system. The model uses parallel heat flux lines or parallel isotherms, shown in Figure 12.

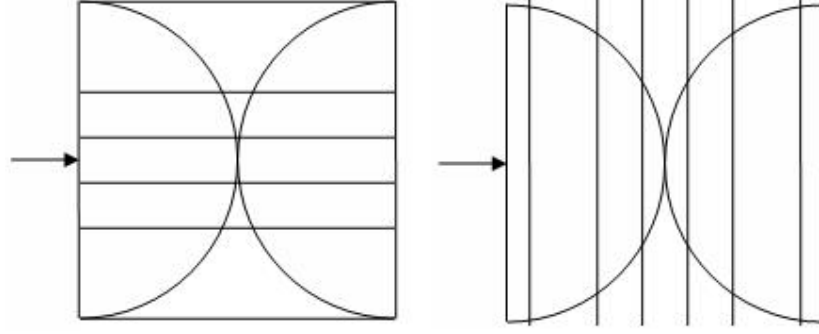


**Figure 12.** Type III heat transfer model, unit cells with parallel paths of heat flux or parallel isotherms. (23)

Type III models have also been implemented with secondary parameters such as radiation and gas pressure. In Type III models, the conductivity can be presented as:

$$k_{2Ph} = 1 - \sqrt{1 - \psi} + \sqrt{1 - \psi} k_c \quad (10)$$

with

$$k_c = \frac{2}{N} \left( \frac{B}{N^2} \frac{k_p - 1}{k_p} \ln \frac{k_p}{B} - \frac{B + 1}{2} - \frac{B - 1}{N} \right) \quad (11)$$

$$k_p = \lambda_p / \lambda, \quad k_c = \lambda_c / \lambda, \quad k_{2Ph} = \lambda_{2Ph} / \lambda. \quad (12)$$

$$N = 1 - B/k_p \text{ and } B \text{ is the particle deformation factor.} \quad (13)$$

Several heat transfer mechanisms affect the temperature dependence of the thermal conductivity of porous materials:

- Thermal conductivity of solid and gas phases
- Free molecular heat transfer of gas in pores
- Absorption and scattering of thermal radiation on solid particles and pores
- Convection in porous materials possessing various gas permeabilities
- Physical or chemical processes resulting in transfer of gaseous products through pores
- Changes of material structure during heating
- Heat barrier resistances caused by grain boundaries and cracks

A model taking into consideration the effect of the radiation, as well as grain boundaries and cracks, and describing the effective thermal conductivity of highly porous (>30%) materials has been proposed by Shapiro et al. (20):

$$k = k_s M (1 - \Pi)^{3/2} + k_{\Pi} \Pi^{1/4} + k_{conv} + k_{rad} \quad (14)$$

where  $k_{\text{conv}}$  and  $k_{\text{rad}}$  represent convection and radiation in the entire sample and  $k_{\Pi}$  the pore phase conductivity. Parameter  $M$  describes the heat-barrier resistances associated with porous grain boundaries and microcracks. The pore phase conductivity includes:

$$k_{\Pi} = k_{\Pi,g} + k_{\Pi,e} + k_{\Pi,s} \quad (15)$$

where  $k_{\Pi,g}$  is the heat conduction in the gas phase,  $k_{\Pi,e}$  heat conduction by gas emission resulting from chemical reactions such as evaporation or sublimation and  $k_{\Pi,s}$  is the heat conduction in segregation and surface-diffusion processes. (20)

All heat transfer mechanisms in porous ceramic materials are affected by the pore and grain sizes, especially over 1000 K, where radiation dominates the heat transfer.

For packed beds of ceramic powders, an almost temperature-independent (up to 300 °C) behaviour of thermal conductivity has been reported (20). Thermal diffusivity decreases slightly, but the change is offset by the moderate increase in specific heat. The effect of bulk density has been found to be significant, with values varying up to 20%, and this is believed to be due to the effect of inter-grain contacts, which improves in the re-packing of the powder.

To analyse the thermal conductivity of a porous media, a periodic structure of the material has been assumed and a unit cell then applied to represent the whole material. The concepts of effective thermal conductivity and effective pore conductivity have been introduced to help the modelling. They are directly measurable material properties that take into consideration several heat transfer mechanisms. (11, 26)

Eucken discovered that the thermal conductivities of crystal materials decrease with increasing temperature according to the formula:

$$k = (C + DT)^{-1}, \quad (16)$$

where  $C$  and  $D$  are material-dependent constants (21).

The temperature dependence of Eucken-type materials is demonstrated in Figure 13 (19).

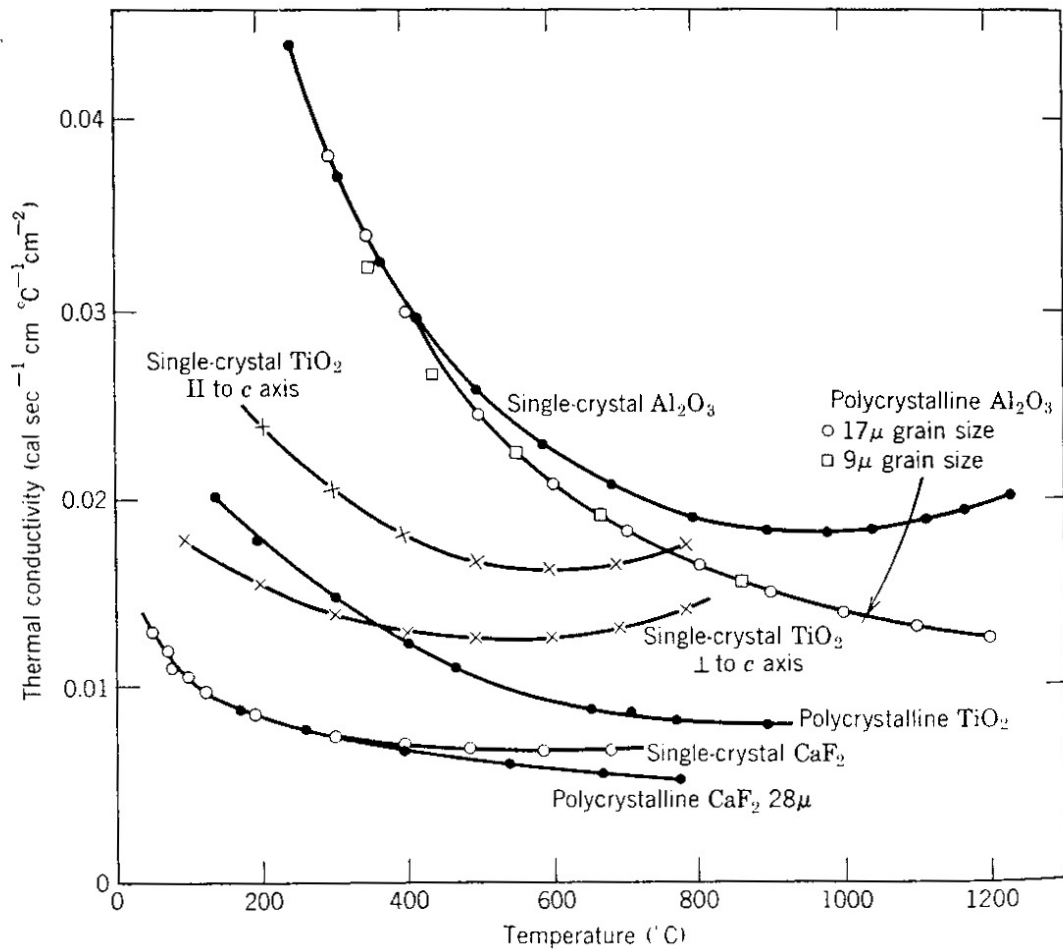


**Figure 13.** Thermal conductivity in crystal materials (19).

The Maxwell-Eucken equation can be used to describe the effect of porosity on the thermal conductivity of a material. At low temperatures, the porosity generally has a low conductivity in comparison to the solid phase, and a nearly linear decrease in conductivity with increasing porosity is found. At high temperatures, radiation across pores becomes a significant contributor to heat transfer. Large pores effectively increase the conductivity at high temperatures, whereas small pores remain a good barrier to heat flow by reducing the photon mean free path and thus limiting the conduction. Other factors that affect the thermal conductivity of a porous material are the transmissivity of the material and, for especially powdery materials, the gas pressure. Different factors affect the thermal conductivity of the material at different temperatures, and all comparisons between conductivity values should be made for similar temperatures. (19)

For higher temperatures, where the mean free path of phonons is comparable to the crystal lattice size, thermal conductivity is either independent of temperature or increases with temperature in proportion to the temperature dependence of the specific heat (21).

Eucken's law effectively describes the thermal behaviour of crystal-like materials. Refractory materials such as magnesia and alumina typically follow Eucken's law. The thermal

conductivity of materials such as quartz and silica, however, presents a different kind of thermal dependence. In glass-like structures the thermal conductivity has an increasing dependence on temperature. An example of the temperature dependence of a glass-like material is presented in Figure 14 (19):

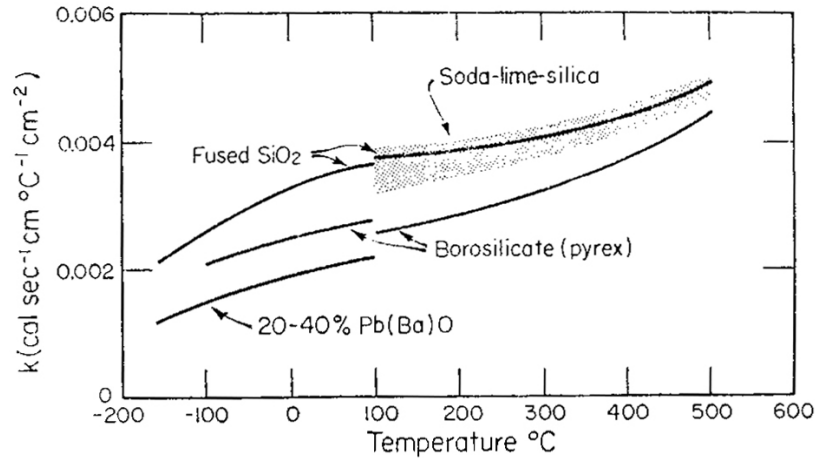
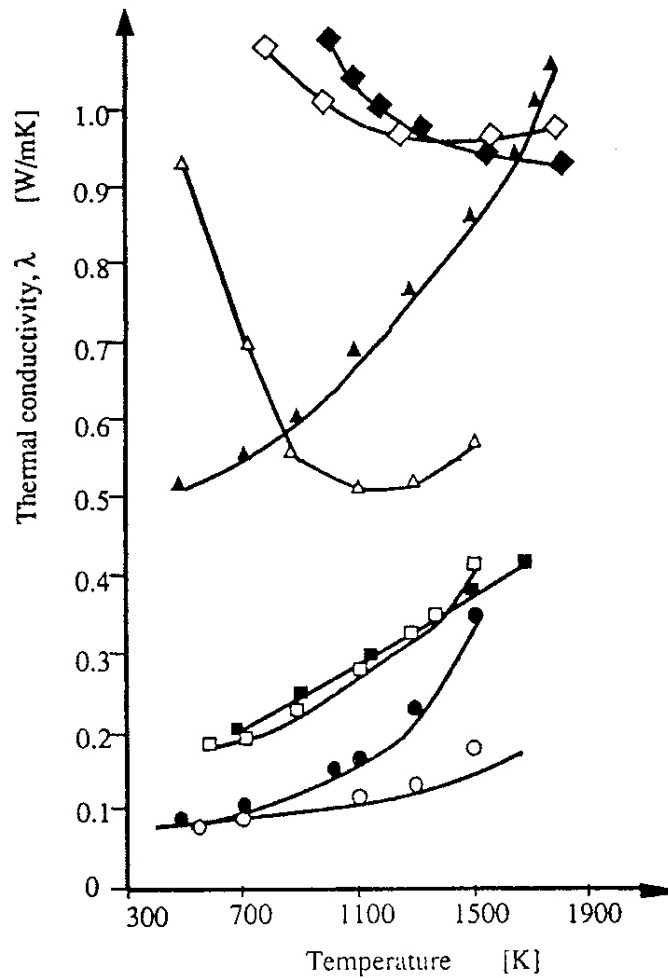


**Figure 14.** Thermal conductivity of several glass compositions (19).

The difference in the temperature dependence between a crystal and a glasslike structure is clearly shown in Figure 15, which shows the temperature dependence of the thermal conductivity of several refractory materials. (22)



$\lambda$  of insulating refractories in air (atmospheric pressure):  
 (○) quartz glass fiber refractory ( $d = 1-3 \mu\text{m}$ ,  $\rho = 0.12 \text{ g}\cdot\text{cm}^{-3}$ );  
 (●) quartz glass fiber refractory ( $d = 10-15 \mu\text{m}$ ,  $\rho = 0.12 \text{ g}\cdot\text{cm}^{-3}$ );  
 (□) porous quartz glass ( $\Pi = 0.55$ ,  $\rho = 1.0 \text{ g}\cdot\text{cm}^{-3}$ ); (■) fire clay  
 ( $\Pi = 0.85$ ,  $\rho = 0.4 \text{ g}\cdot\text{cm}^{-3}$ ); (▲) silica ( $\Pi = 0.57$ ,  $\rho = 1.0 \text{ g}\cdot\text{cm}^{-3}$ );  
 (◆) magnesia ( $\Pi = 0.68$ ,  $\rho = 1.13 \text{ g}\cdot\text{cm}^{-3}$ ); (◇) magnesia ( $\Pi = 0.72$ ,  
 $\rho = 1.11 \text{ g}\cdot\text{cm}^{-3}$ ); and (△) alumina produced by foam technology  
 ( $\Pi = 0.88$ ,  $\rho = 0.49 \text{ g}\cdot\text{cm}^{-3}$ )

**Figure 15.** Temperature dependence of thermal conductivity values of refractory materials.  
 (22)

## 2.4 Thermal conductivity of boiler deposits

Information on the thermal conductivity values of fouling deposits in metallurgical processes is virtually non-existent and providing that information is the main focus of this research. Some information on the thermal conductivities of coal ash deposits in the coal combustion industry has been reported. Rezaei et al. (27), Wall et al. (28-30), Anderson et al. (31), Boow et al. (32), Abryutin et al. (33, 34), and Mills (35) have reported the thermal conductivity values of several coal ash deposits. They observed an increasing trend in the thermal



conductivity values as a function of increasing temperature. A decrease in the porosity of the sample was also observed to increase the thermal conductivity. The physical structure of the ash deposit was reported to have a greater influence on the thermal conductivity than the chemical composition of the sample. Increasing the mean particle size increases the thermal conductivity, while increasing porosity reduces the values. The effect of the particle size has been reported to be greater than the effect of porosity (29). The  $\text{SiO}_2$  content of the ash is an important parameter affecting thermal conductivity at higher temperatures.

A clear increase in thermal conductivity was observed with an increase in particle size, as shown in Figure 16 (27).

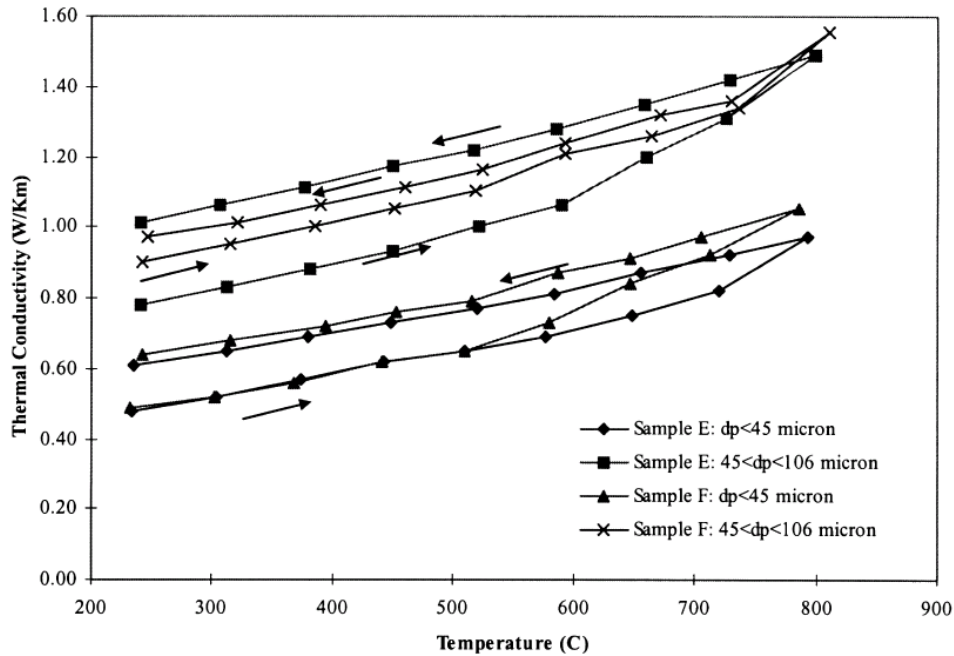
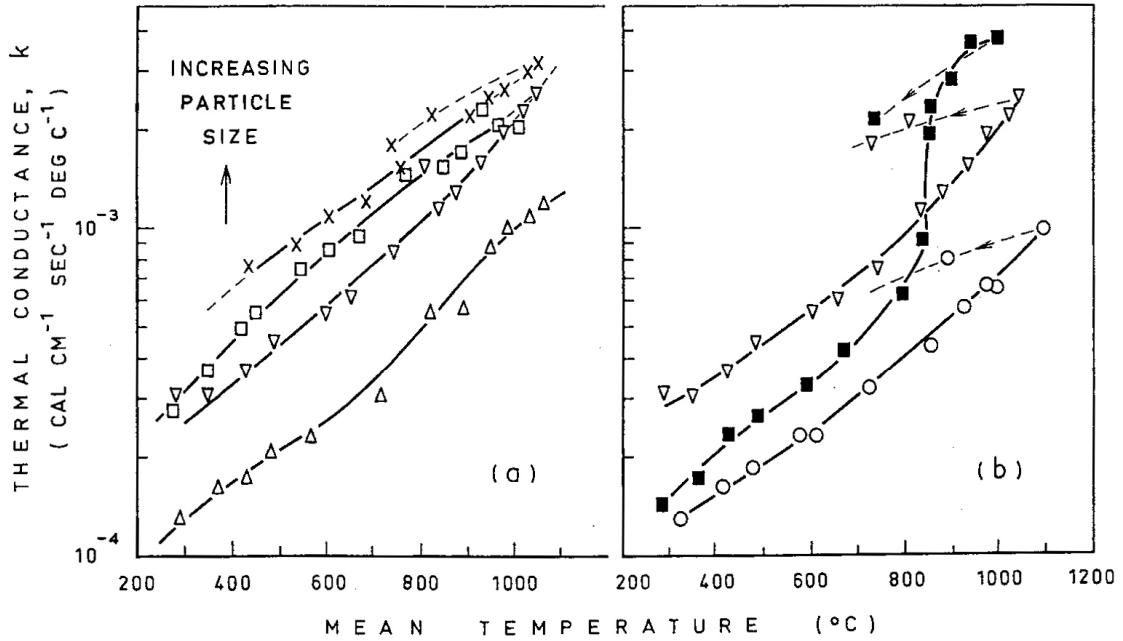


**Figure 16.** Effect of particle size distribution on thermal conductivity of synthetic ash samples E and F. E= 53%  $\text{SiO}_2$ , 22%  $\text{Al}_2\text{O}_3$ , 15%  $\text{Fe}_2\text{O}_3$ , 10%  $\text{CaO}$ . F= 55%  $\text{SiO}_2$ , 33%  $\text{Al}_2\text{O}_3$ , 12%  $\text{CaO}$ . (27)

Boow et al. (32) reported that the thermal conductivity of the particles almost quadruples as the average size increases from <44  $\mu\text{m}$  to 211-422  $\mu\text{m}$ , as shown in Figure 17.



Influence of particle size on thermal conductance of synthetic slag containing 5% Fe<sub>2</sub>O<sub>3</sub>.  
 (b) Influence of 'colour' on thermal conductance of 53 to 104 μm size fraction of synthetic slags.  
 × 36, □ 37, ▽ 38, △ 39, ○ 34, ■ 42.

Figure 17. Influence of particle size on thermal conductivity of coal ash deposit slags. (32)

Wall et al. (28-30) also reported the influence of the particle size on thermal conductivity for ash deposits, as shown in Figure 18.

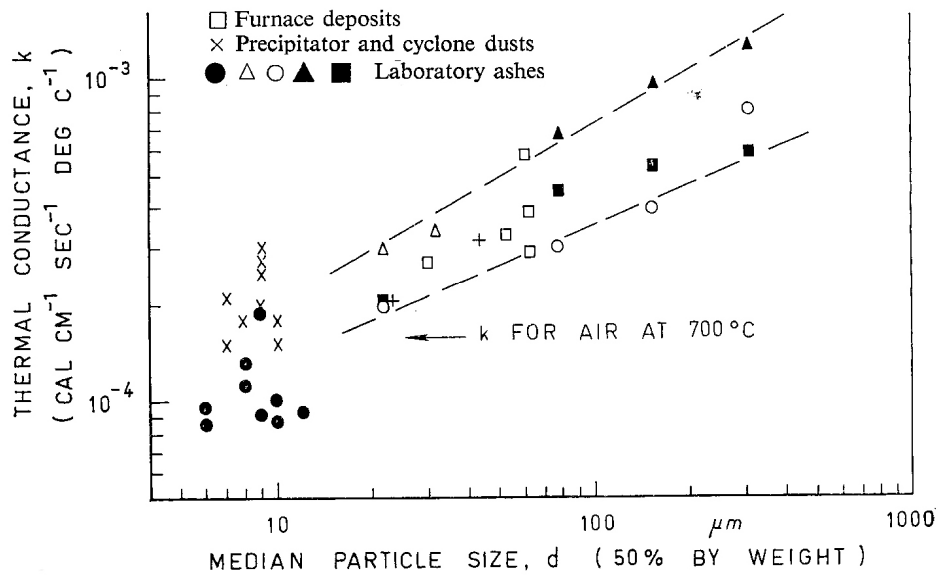
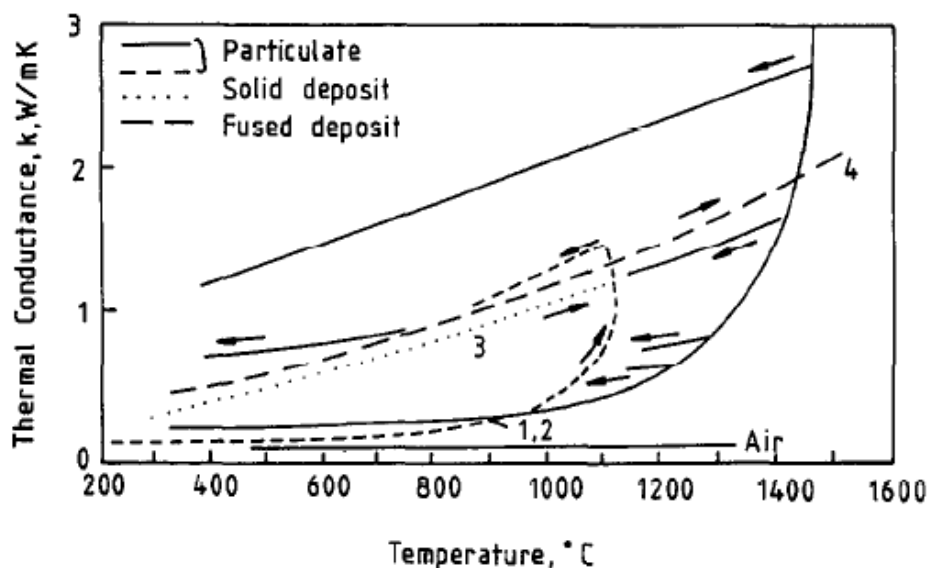


Figure 18. Influence of median particle size of materials on thermal conductivity at a mean temperature of 700 °C. (28-30)

Wall et al. (28-30) and Anderson et al. (31) reported that the thermal conductivity values are fairly temperature-independent below the sintering temperature of around 900-1200 °C, as demonstrated in Figure 19. Further heating softens the sample and improves the contact between the particles. The chemical and physical changes in the structure cause increasing thermal conductivity. The coal ash deposits contain a large amount of SiO<sub>2</sub> and the thermal conductivity behaviour of the deposits as a function of temperature seems to be similar to the temperature behaviour of SiO<sub>2</sub>, thus having an increasing temperature dependence, rather than the typically decreasing trend typical of materials such as alumina or magnesia.



**Figure 19.** Collected data on thermal conductance reported by Anderson et al. (31) as ash is heated and cooled. The arrows indicate the direction of temperature change. 1, 2 - particles; 3 - solid deposits; 4 - fused deposits.

The transformations taking place in the microstructure of materials during exposure to high temperatures involve the nature of the grain-grain contacts, elimination of porosity, and grain growth (36). Increasing the grain size generally increases thermal conductivity. The formation of grain boundaries and the increasing contact area between the grains cause a strong increase in the thermal conductivity of the material.

The effect of the thermal history of the deposit is visible in Figure 20 from Boow et al. (32). The deposits extracted from the high-temperature zones of the process show clearly higher original conductivity values than the loose dust particles or ashes, but, as the samples are subjected to sintering temperatures or higher, the conductivities of the loose particles approach the values of the high-temperature deposits.

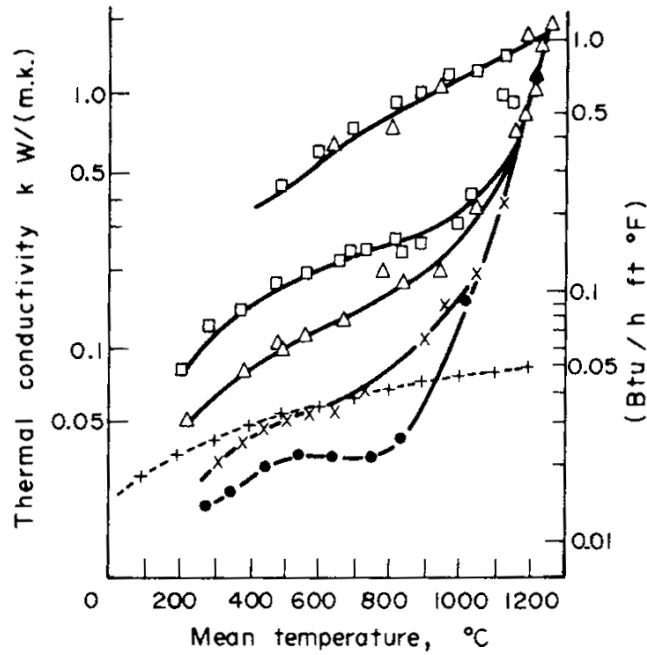


**Figure 20.** Thermal conductivity of combustion chamber deposit ( $\square$ ), primary superheater deposit ( $\Delta$ ), ESP dust ( $x$ ), and laboratory ashes ( $\circ \bullet +$ ). (32)

Figure 21 shows the decrease in thermal conductivity values resulting from increasing porosity.

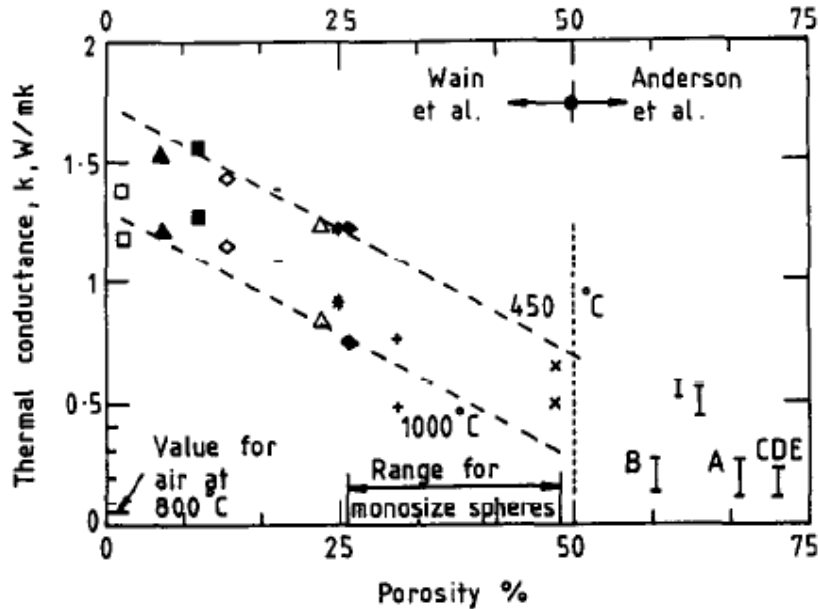
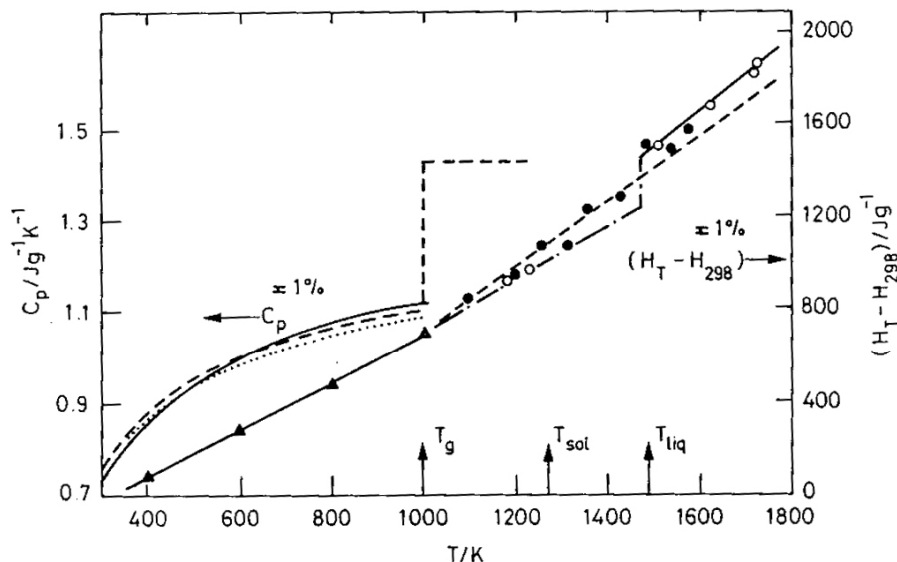


**Figure 21.** Summary of data showing the variation of thermal conductance of deposits with porosity with data from Wain et al. and Anderson et al. (31), reported by Wall et al. (29).

Mills et al. (35) investigated the specific heat capacity values and thermal diffusivity values of several coal gasification slags. The slagging process softens and melts the matter and takes

place on the surface of the deposit when high enough temperatures are present. Specific heat measurement results are presented in Figure 22.



Heat capacity values for slag A:  $\blacktriangle$ , d.s.c. results;  $\bullet$ ,  $\circ$  drop calorimetry results for a.r. and pure slag samples, respectively;  $-\cdots-$ , extrapolation from the glassy phase;  $---, \dots$ , estimated values for a.r. and pure slag samples, respectively

**Figure 22.** Specific heat capacity and enthalpy of coal gasifier slags. (35)

Specific heat capacity values increase fairly steadily until a glass transition temperature of around 1000 K takes place and values increase dramatically. Above the glass transition temperature the material softens into a supercooled liquid state. Mills et al. (35) reported the Kopp-Neumann mixing rule to reliably estimate the heat capacities of slag mixtures. The rule states that the heat capacity of a mixture is proportional to the heat capacities of its components in relation to their mole fractions.

A schematic presentation of the temperature behaviour of the slag heat capacity is shown in Figure 23. A clear increase step in the specific heat capacity values can be seen when the physical stage of the material changes.

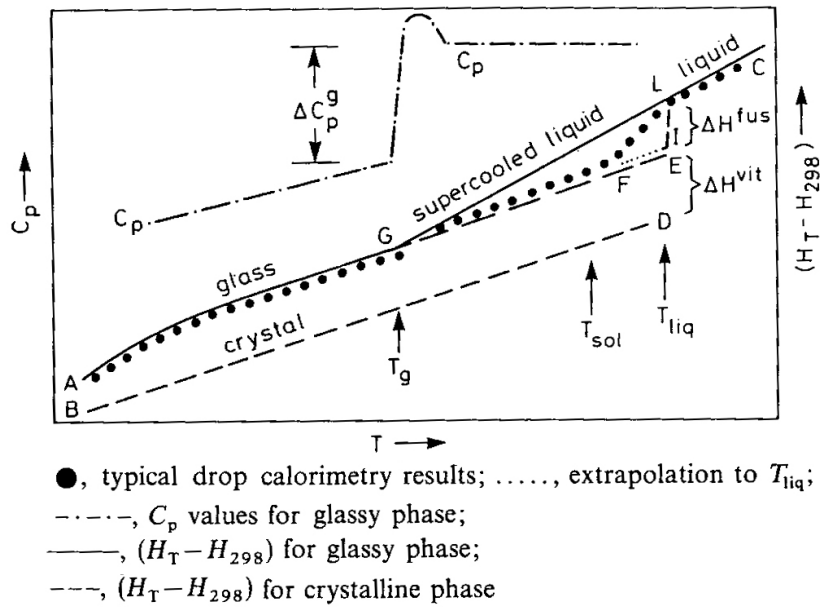


**Figure 23.** Schematic representation of heat capacity and enthalpy values for glass and crystalline phases of a slag. (35)

Mills et al. (35) also used the laser pulse method to determine the thermal diffusivity values of the slags. Their results are presented in Figures 24, 25, and 26.

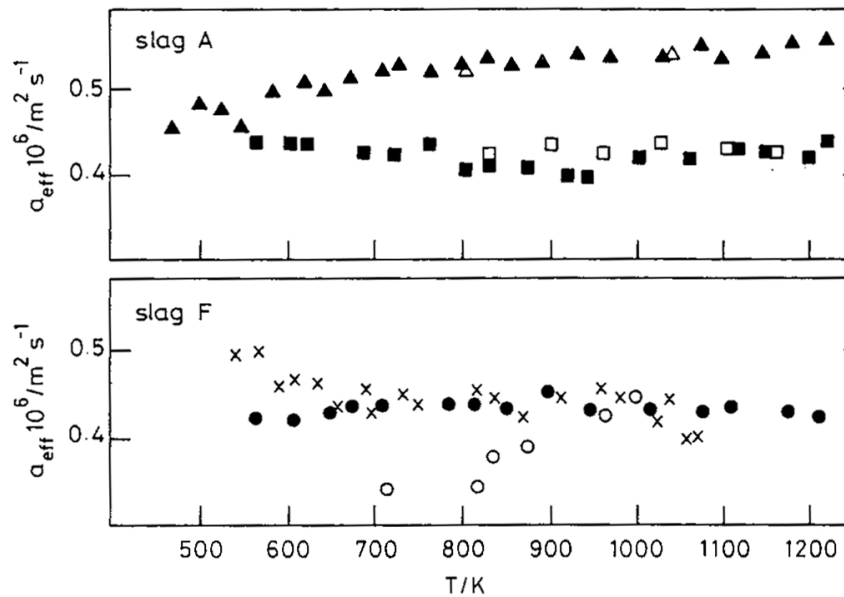


**Figure 24.** Thermal diffusivities of coal gasifier slags: filled symbols heating cycle, open symbols, cooling cycle.  $\Delta, \blacktriangle$ , A (I) (1 mm thick);  $\square, \blacksquare$ , A (II) (3 mm thick),  $x$ , F(II) (1 mm thick);  $\bullet, \circ$  F(II) (3 mm thick) (35)

All specimens had fairly stable values of thermal diffusivity, showing a slight decrease as a function of temperature. Slag A (I) was obtained by a different cooling method than the

others and, probably because of a different crystallisation structure, does not follow the same trend.

A decrease in the thermal diffusivity values above the glass transition temperature and a dramatic increase above the melting temperature are shown in Figure 25.

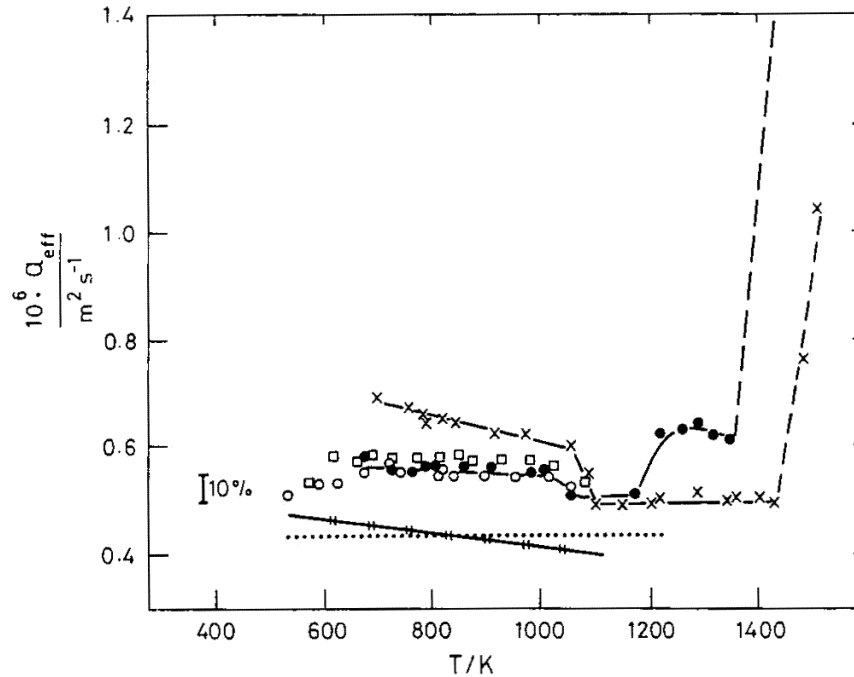


**Figure 25.** Thermal diffusivities of coal gasifier slags:  $\square$  Slag A; free-standing,  $x$  Slag A; in cassette,  $\dots\dots$  Slag A; previous results with free-standing specimen,  $\circ$  Slag F; free-standing,  $\bullet$  Slag F; cassette,  $\text{---}$  Slag F; previous results. (35)

The comparison of glassy and crystalline slags in Figure 26 shows higher values for the crystalline ones, as a result of the higher radiation conductivity contribution of that material.

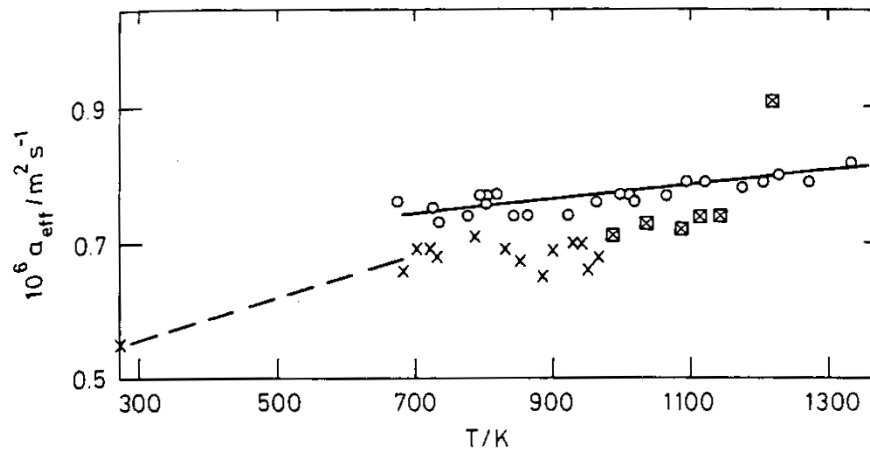


**Figure 26.** Thermal diffusivities of coal gasifier slags:  $\circ$  crystalline,  $x$  glassy,  $\boxtimes$  results obtained in a sapphire cassette. (35)

The thermal conductivity values calculated on the basis of the thermal diffusivity and specific heat measurements and density data are shown in Figure 27:

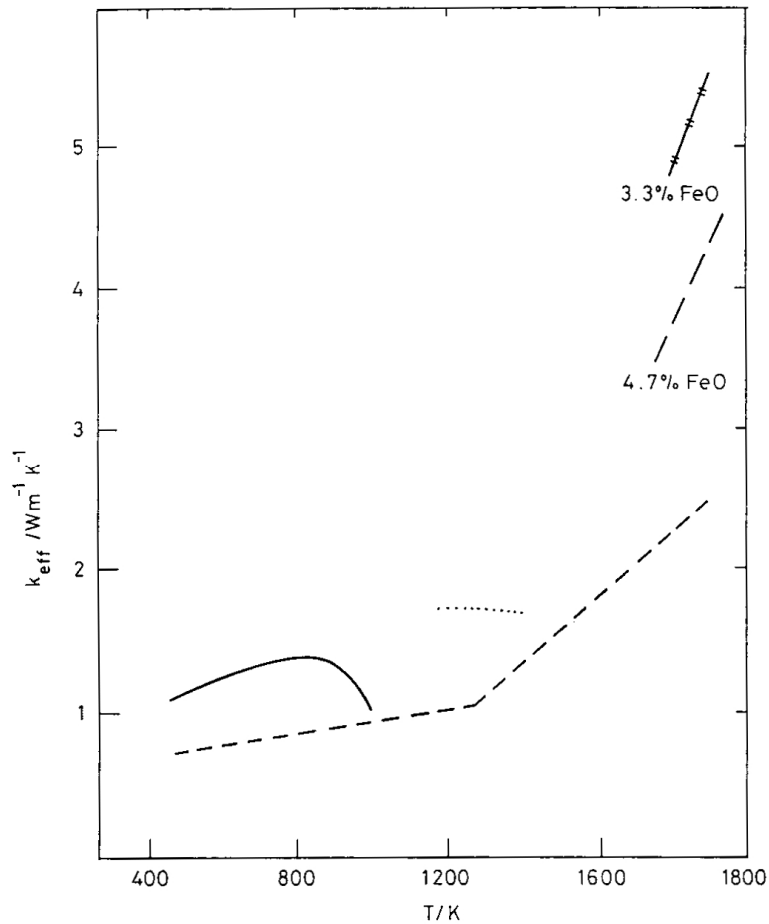


**Figure 27.** Thermal conductivity of coal gasifier slag A: ——— experimental;  
 .....extrapolation of  $C_p$ ,  $\rho$  and thermal diffusivity values;  
 -----, -//—previous work (35)

The glass transition reduces the thermal conductivity values around 900K. The thermal conductivity of ash deposits depends on several factors, such as the chemical composition, the physical state and texture, and the temperature of the material. Wall et al. (29) divide the ash deposits into four categories:

- relatively loose deposits;
- bonded deposits;
- slag deposits, and
- bonded slag deposits.

Loose deposits consist of mechanically adhered ash particles that can easily be removed. Bonded and bonded slag deposits are formed over a long period of time and usually have layers of non-uniform matter that has varying thermal conductivity.



Wall (28) reports an estimation of a decrease of up to over 15% in the furnace efficiency resulting from the deposit growth, as shown in Figure 28.

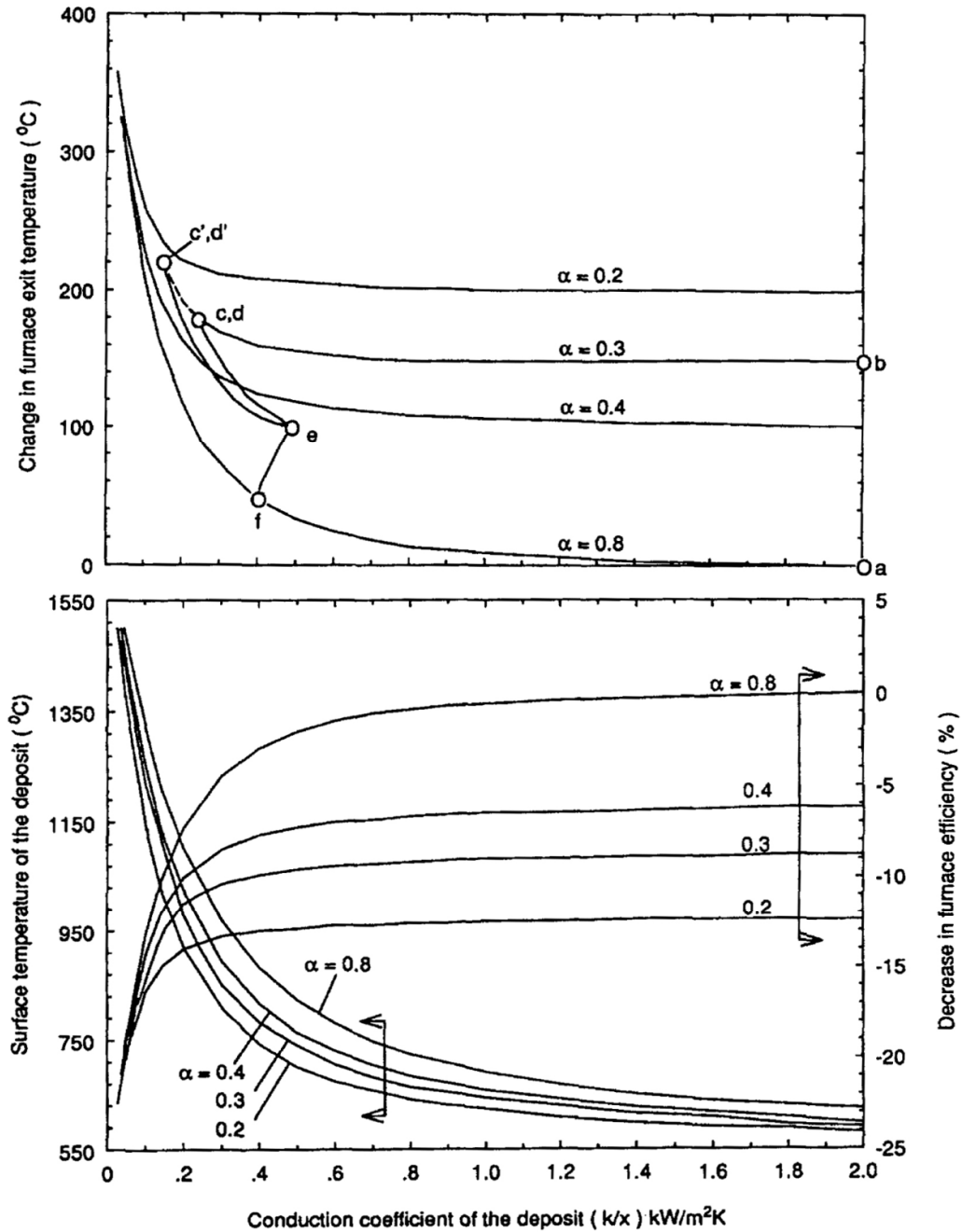
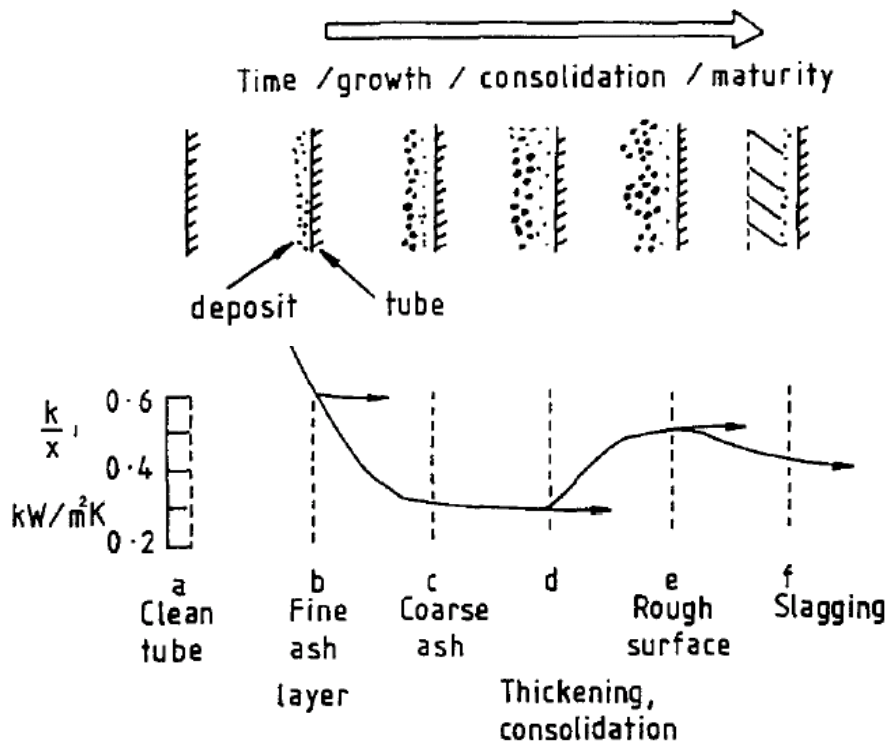


Figure 28. Prediction of the changes in the performance of furnaces and deposit temperature during the changes in deposit properties. ( $\alpha$ =absorbance)(28)

Wall et al. (29) investigated the possibility of correlating the ash deposit thermal conductivity results with packed-bed heat transfer models. The packed-bed models were, however, unsuccessful in predicting the thermal behaviour of ash. The main difficulties were the assumptions that the models use a uniform particle size, packing, and porosities. The ash samples have large local variations in these properties, along with unknown solid-phase thermal conductivity and surface emissivity. The packed-bed model can nevertheless be useful in explaining qualitatively some of the observed trends in the thermal behaviour of ash deposits.

## 2.5 The deposition mechanism of fouling layers

Wall et al. (28-29) have suggested a growth mechanism for fly ash deposition, which is demonstrated in Figure 29.



**Figure 29.** Expected trends in deposit properties and thermal conductance during their growth. (28)

They suggest that the initial deposit (a) consists of fine condensable salts or fine ash transported by the thermophoresis mechanism. In the second stage (b) the fine layer thickens and results in the collection of larger particles, developing into a layer of coarse ash (c). In the third stage the layer thickens (d) and sinters, leaving a rough surface (e). Finally, a liquid slag develops on the surface (f). The suggested thermal conductivity values for the deposit vary from 0.3 to 0.6  $\text{kW/m}^2\text{K}$ .

Wall et al. (30) suggested a mechanism for the build-up of deposits. They listed the following requirements for the deposit formation:

1. volatiles or fly ash must come into contact with the tube surface;
2. the materials have to adhere to the surface, and
3. sufficient cohesion must take place to allow deposit growth without it shedding under its own weight, vibration, temperature cycling etc.

Materials are likely to be conveyed onto the surface by either diffusion or direct impact. Particles of a diameter of 3  $\mu\text{m}$  or less are likely to diffuse onto the surface. Vapour condensation includes several types of diffusion mechanisms, such as molecular diffusion, Brownian motion, and eddy diffusion. The inherent surface roughness, electrostatic attraction, and the presence of sticky compounds all affect the fouling process.

The surface roughness may be attributed to iron oxide whisker growths, possibly aided by crystalline growths of desublimed alkali salt vapours. A sticky coating of condensing vapours may form on the tube walls at temperatures of around 500  $^{\circ}\text{C}$ , near the melting point of the eutectics of the  $\text{NaCl-KCl-Na}_2\text{SO}_4\text{-K}_2\text{SO}_4$  system. The supercooling of condensing droplets in the thermal boundary layer of the tubes may also contribute to a sticky coating. Fly ash particles with alkali-rich surfaces may result from the reaction between silica fly ash or submicron silica fumes and the alkali vapours present in the gas.

The interaction between particulates and fluid flow is very complex, especially in a turbulent flow field. The presence of a temperature gradient between the flow field and the heat exchange surface makes the prediction of a theoretical fouling model very difficult. (37) The temperature gradient causes the deposition mechanism known as thermophoresis. With thermophoresis small particles with a diameter of less than 0.1  $\mu\text{m}$  move towards the cooler region of the gas. Thermophoresis is further enhanced by increasing the thermal gradient and deposition distance and is reduced by increasing the particle size (38). Other deposition mechanisms include irregular particle motion caused by random collisions, known as Brownian motion (39), drag, gravity, convection (38), and crystallisation (40).

Abd-Eldhady et al. (41) investigated heat exchanger tube fouling and discovered that the smallest particles attach to the furnace tubes first. Those particles found closest to the tube surface had a diameter of 1 to 10  $\mu\text{m}$ . In their experiments with copper, bronze, and glass particles over steel tubes, they discovered that small particles have the highest sticking velocities, as shown in Figures 30 and 31. The coefficient of restitution indicates the ratio of particle velocities before and after the collision. Particles with low coefficients stick to the surface, whereas the particles with coefficient close to one bounce back from the surface.

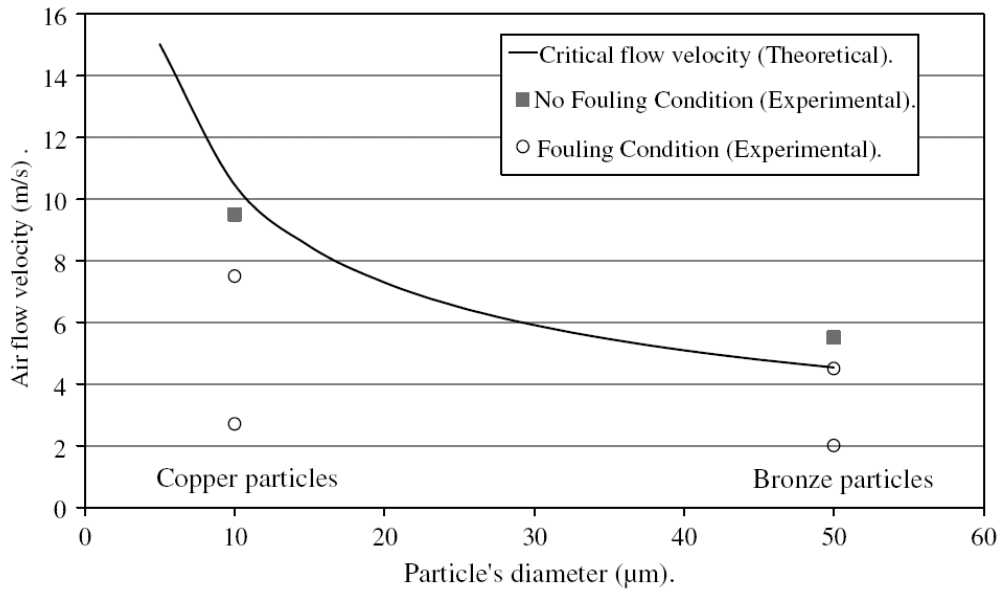


Figure 30. The critical flow velocity and limiting fouling speed versus particle diameter. (41)

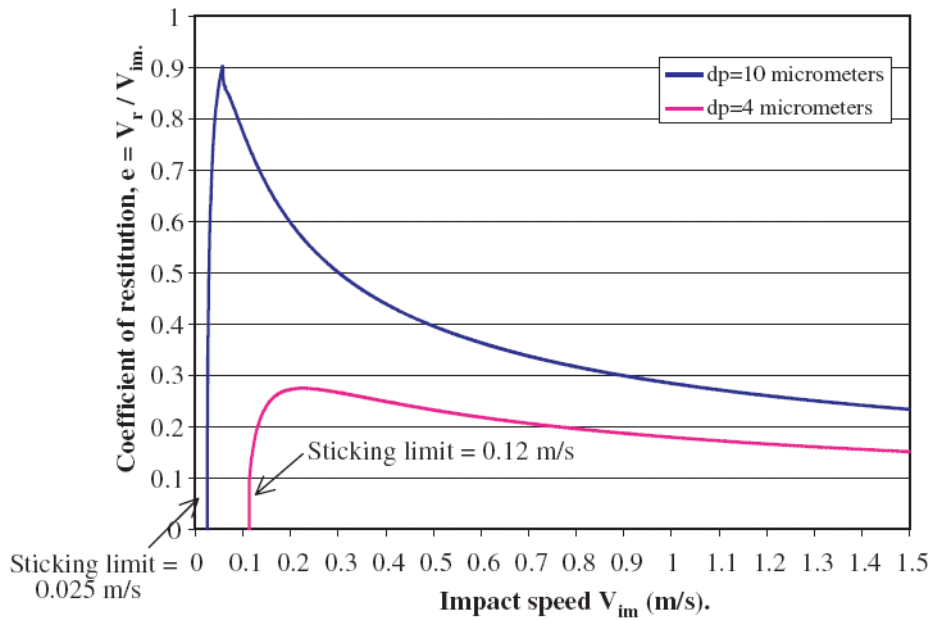
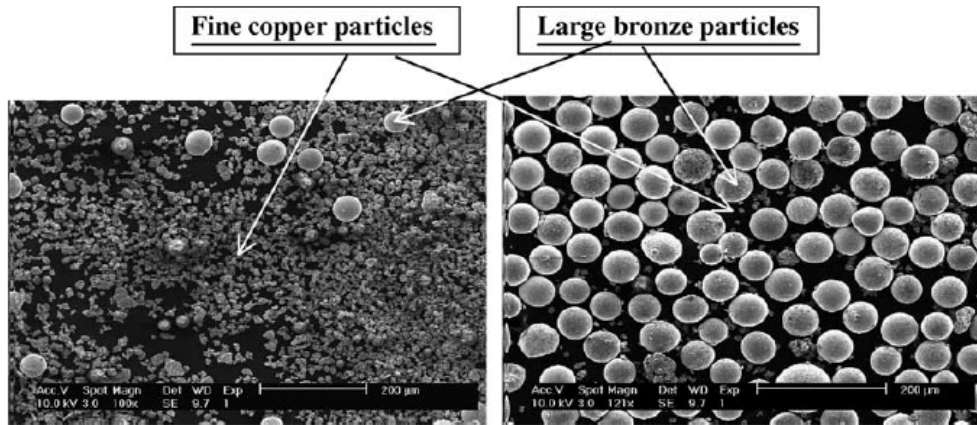


Figure 31. Coefficient of restitution versus impact speed for copper particles hitting a solid steel surface. (41)

Larger particles roll over the surface until they are stopped by a heap of smaller particles. Once the small particles have attached to the surface, the larger ones are also able to deposit, as shown in Figure 32.



**Figure 32.** SEM photos for the particles at the bottom and top of the fouling layer, composed of copper and bronze particles. (41)

Some particles also start to deposit at intermittent and distant positions, allowing radial fouling of the surface, which is evident in Figure 33.

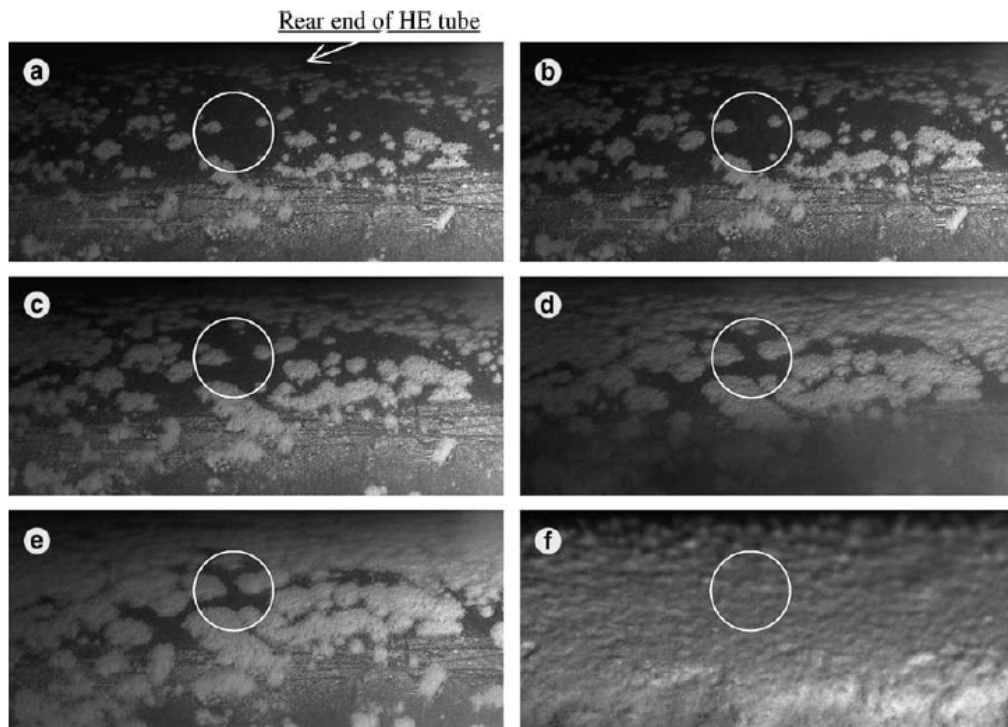


**Figure 33.** Progress of the fouling layer over the heat exchange tube within 9 hours of operation. Spherical glass particles of  $21 \pm 16 \mu\text{m}$ . (a) 1 h (b) 1.5 h (c) 2 h (d) 2.5 h (e) 3 h (f) 9 h. (41)

Walsh et al. (42) and Lee et al. (43) report a strong particle size dependency for the sticking probability of sulphate coated particles, as shown in Figures 34 and 35. If the interfacial

energy of the area over which contact is established between the particle and the surface is greater than the kinetic energy of the particle, the particle will stick onto the surface; otherwise it will not. Large particles have a higher inertia force and are less likely to stick. The deposition rate is proportional to the impact angle of the particle on the surface. Small particles are more likely to stick, even with small contact angles.

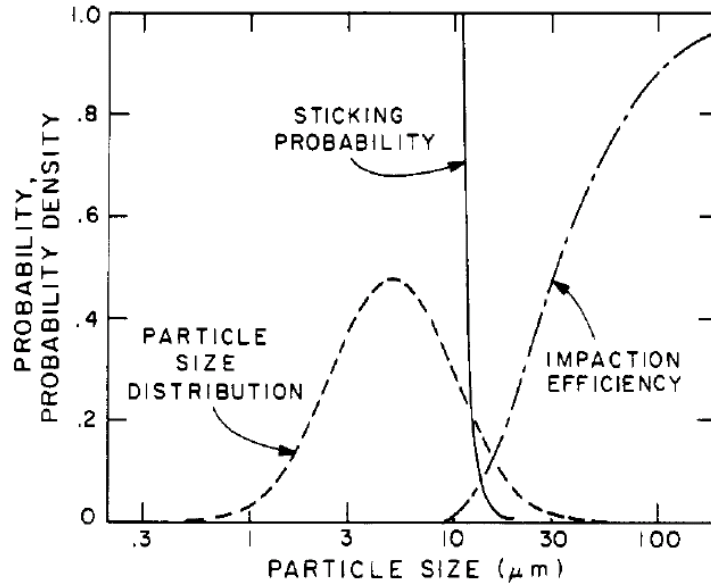


**Figure 34.** Comparison of particle size distribution, impact efficiency, and sticking probability for sodium sulphate-coated calcium aluminosilicate particles. (42)

The effect is more pronounced for clean surfaces, as shown in Figure 35.

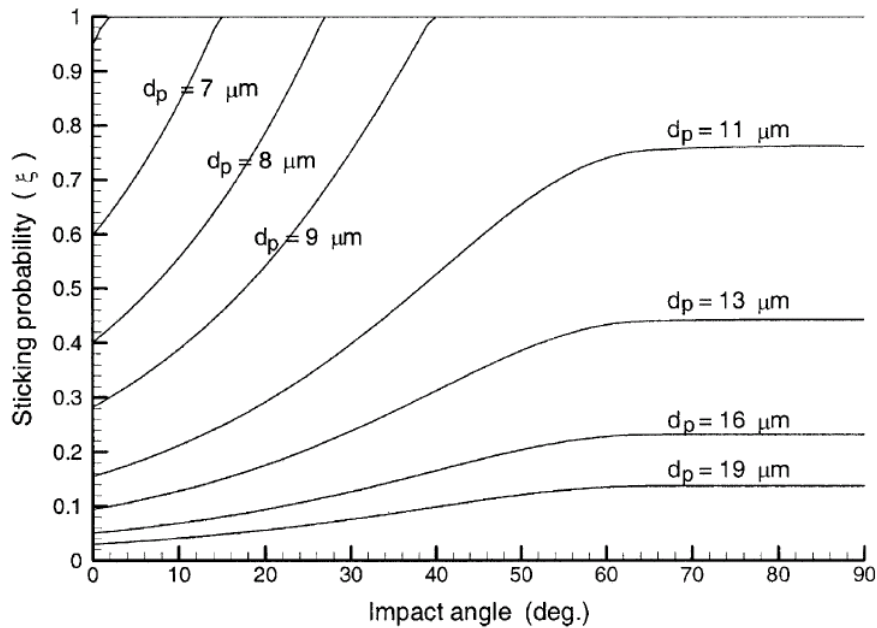


**Figure 35.** Sticking probabilities of sodium sulphate-coated particles colliding with a clean tube surface. (43)

Once the surface is covered with deposited particles, the larger particles also have a higher probability of sticking as a result of the surface roughness causing more irregular bouncing and multiple impactions. The sticking probabilities of different particle sizes on a deposit surface are presented in Figure 36.

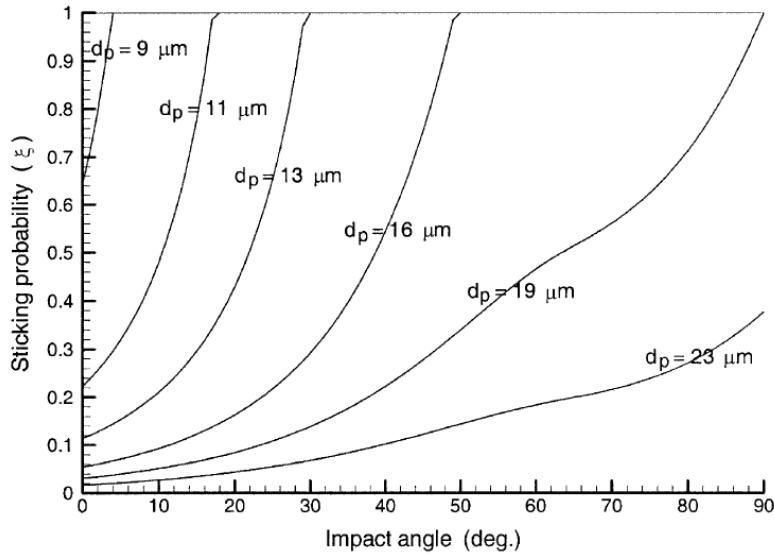


**Figure 36.** Sticking probabilities of sodium sulphate-coated particles colliding with a deposit surface. (43)

The stickiness of the surface may also contribute to increasing deposition rates, as shown in Figure 37.

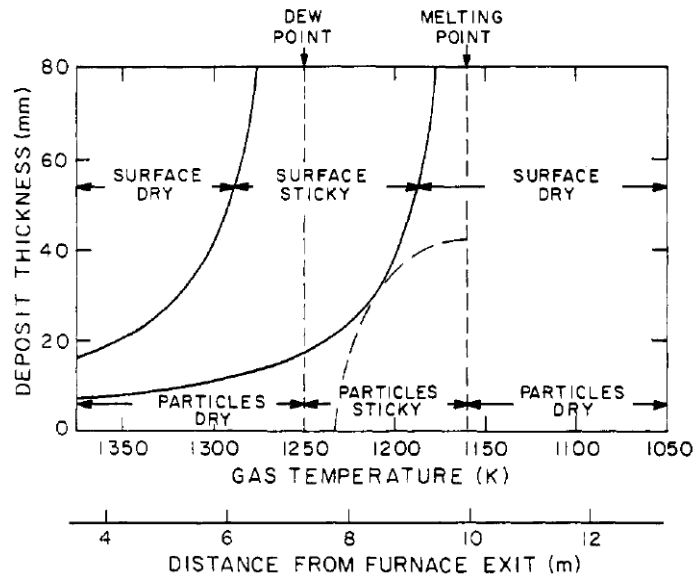


**Figure 37.** Regimes of deposit formation resulting from the influences of the sodium sulphate dew point, the melting temperature of the calcium-magnesium-sodium sulphates, and the increase in deposit surface temperature with increasing thickness. (42)



Figure 38 presents the expected thickness of a coal ash deposit after 3 to 12 months of operation. The thickest layer is formed in the zone of the highest sodium sulphate vapour concentration.

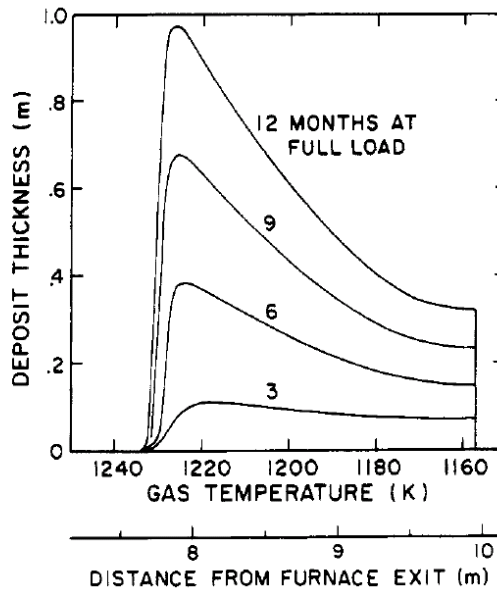


**Figure 38.** Thickness of deposits expected in regions of the convective section after 3-12 months of continuous full-load operation. (42)

Once the fouling has started and particles accumulate to build up the fouling layer, sintering takes place. Sintering changes the fouling structure from a weak powdery layer into a solid stable structure. (41, 44-45)

Anthony et al. (46-50) have investigated the causes for sulphate agglomeration in circulating fluidised bed combustion (CFBC) boilers. They noticed that agglomeration may take place through the sulphation process alone in the absence of low-melting-point alkalis. The following mechanisms were suggested as the causes of sulphate agglomeration:

1. sintering of particles. Solid state sintering that will bind particles together at sufficiently high temperatures;
2. chemical hardening. Chemical reactions that form compounds at the junction of particles;
3. molecular cramming. The effect of filling empty available spaces in masses of material restricted to a given volume by the increase in molar volume of reacting compounds. Interstitial space between particles will be filled with the reaction product, increasing the contact area between particles and producing a denser material, and
4. particle swelling. Swelling can cause particles to mechanically weld onto one other.

They suggest that the CFBC boiler deposits may result from chemical hardening assisted by the cramming effect. The deposit location may enable  $\text{SO}_2$  to diffuse slowly through the



material, resulting in complete sulphation of the particles. The gas atmosphere within the deposit layer may be very different from the standard atmosphere of the boiler.

Typically fouling layers develop in three stages, shown in Figure 39:

1. nucleation;
2. growth, and
3. asymptotic (40).

Overall, the fouling exhibits an S-curve, where initially the growth is fast but after a while the growth rate reduces. The thermal resistance of the fouling layer is at first negligible or even negative as a result of the increase in the surface area through increased surface roughness. As the deposition proceeds, significant thermal resistance also develops. At some point, the resistance ceases increasing and levels off at a constant value.

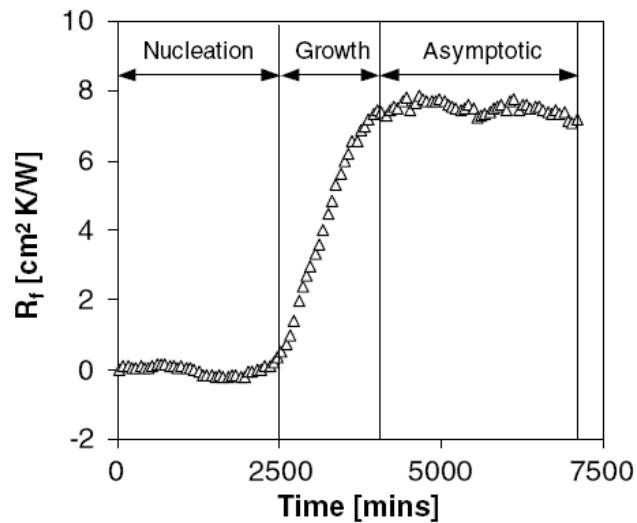


**Figure 39.** Fouling thermal resistance curve showing the different time regions of crystallisation fouling. (40)

Similar S-curve behaviour has been detected in the sintering process and thermal conductivity of coal ash depositions, as shown in Figure 40 (45).

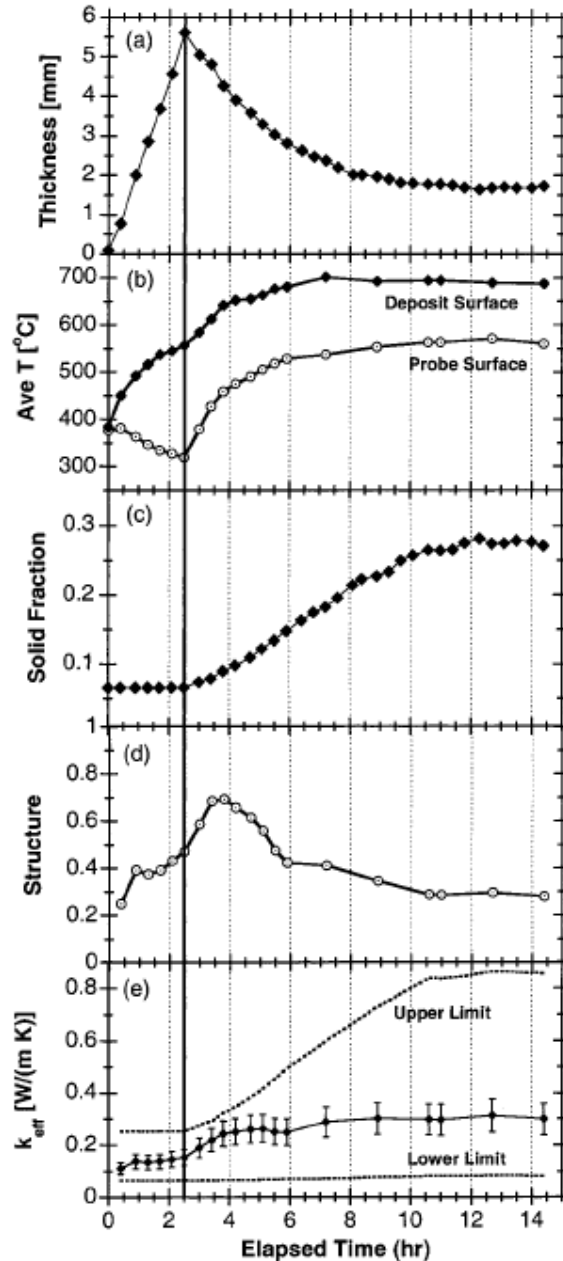


**Figure 40.** Measurements of: (a) average deposit thickness; (b) average probe and deposit surface temperature; (c) deposit solid fraction; (d) deposit structural parameter, and (e) deposit effective thermal conductivity as a function of time. (45)

Robinson et al. (44-45) reported that the initial stage of sintering causes a substantial increase in the thermal conductivity of the deposit. Subsequent sintering has relatively little effect on the overall thermal conductivity of the deposit. Their analysis showed a layered microstructure in the deposit. They suggest that the layers with the lowest thermal conductivity largely determine the overall thermal conductivity of the deposit. The porosity or density of the layer cannot directly be used as the measure of the effects of sintering on the thermal conductivity of the deposit. Changes in microstructure are likely to radically alter the thermal conductivity of layers with similar densities.

Over time a mature deposit structure consisting of an inner, primary, and secondary layer may occur. A presentation of the schematic layer structure is shown in Figure 41.

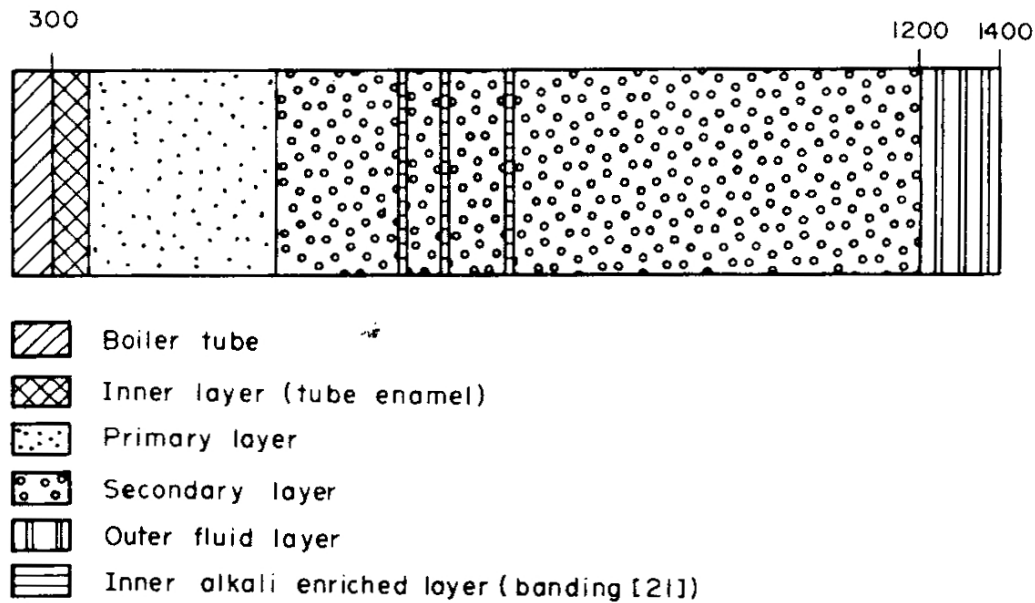


*Figure 41. Generalised section through a mature thick fireside deposit with approximate temperatures indicated in °C. (44)*

The inner layer usually reacts with the tube surface, producing “tube enamel”. The primary deposit consists of fine particles of less than 3  $\mu\text{m}$  and is highly enriched in alkalis. It is formed by the diffusion of vapours and fine fly ash particles onto the surface. The growth of the primary deposit is enhanced by the increasing surface temperature of the deposit and retarded by the decomposition of complex sulphates with temperature.

As the layer grows and the temperature increases, a secondary layer starts to form. The secondary layer consists of coarser particles (1-100  $\mu\text{m}$ ) and contains fewer alkalis. The formation of the secondary layer is usually much slower than the primary one. It is believed that the secondary layer is formed by the collection of fly ash from the gas stream by virtue of the sticky nature and roughness of the outer surface and consolidation of the deposit layer. The consolidation takes place in several steps:

1. growth of a cementing matrix of interlocking crystals and compounds such as  $\text{CaSO}_4$ ;
2. sintering of fly ash particles aided by the formation of low melting point reactive alkali components such as  $\text{Na}_2\text{O}\cdot\text{SiO}_2$ ;
3. the migration of compounds towards the cooler inner parts of the deposit, producing enriched bands, and
4. sintering of the outer deposit layer resulting from increasing deposit surface temperature with deposit growth.

Deposit build-up may also result in an increase in the gas temperature, allowing further deposition mechanisms to occur.

## 2.6 Discussion

Copper Flash Smelting flue dust accretions consist of a complex mixture of components, usually including  $\text{CuSO}_4$  and  $\text{Fe}_3\text{O}_4$ , as well as various ferrites. Condensed particles of volatile components such as As, Pb, and Zn are also often found. In the hot areas of the gas trail dust particles tend to be in oxide or sulphide form, but usually react into sulphates at lower temperatures.

The interconnected dust particles form porous layers of accretion on the heat recovery boiler walls and on the tube banks, reducing the heat transfer efficiency of the boiler. The thermal transportation properties of the Copper Flash Smelting flue dust accretions have not previously been reported and it is the aim of this work to produce such data to be used in modelling and optimising the process and in the dimensioning of boilers.

Boiler accretions can be regarded as composite materials, consisting of a solid and a gas phase. The layers that consist of separate particles have large heat-barrier resistances within the material and thus low thermal conductivities. For mature layers that have undergone sintering and grain growth the conductivity is likely to be enhanced. Several models have been suggested to describe the thermal transportation properties of porous systems and packed beds. Their applicability to modelling the thermal conductivity of a flue dust accretion layer must be considered rather challenging because of the heterogeneity of the layers and the assumptions made in the models.

The real-life systems most similar to the Copper Flash Smelting accretions can be found in coal combustion boilers, where fly ash tends to form similar layers. The deposition mechanisms and thermal transportation properties of the ash layers have been studied and may bear a resemblance to the ones found in copper smelting processes. Layers tend to be initiated by the condensation or thermophoresis of particles smaller than  $10\ \mu\text{m}$ . After the initial layer has formed, larger particles are able to deposit, mainly through impaction. Sintering, grain growth, and other structural changes cause changes in the mechanical and thermal properties of the layers, usually resulting in denser, mechanically stronger layers with higher thermal conductivities. Most ash deposit layers have fairly low thermal conductivities, of less than  $0.5\ \text{W/mK}$  for particulate layers and less than  $2\ \text{W/mK}$  for sintered material.

### 3. EXPERIMENTAL

The aim of the experimental part of this work was to characterise Copper Flash Smelting dust and accretion samples and to determine the thermal properties of the samples. Pure sulphates were used as reference materials. The samples were characterised with scanning electron microscope image analysis and energy dispersive X-ray spectroscopy (EDS), particle size distribution measurements, thermal gravimetry, and differential scanning calorimetry. Thermal diffusivity measurements were conducted with laser flash analysis and thermal conductivity measurements with transient plane source measurements.

#### 3.1 Characterisation of materials

##### 3.1.1 Sample materials

The following samples collected from Harjavalta copper smelter heat recovery boiler were used in the investigation:

**Sample I** Loose flue dust gathered from the dust hoppers of the radiation section.

**Sample II** Loose flue dust sampled by suction from the radiation section.

**Sample III** Loose flue dust gathered from the dust hoppers of the convection section.

**Sample IV** Dust build-up collected from the radiation screens, shown in Figure 42.

**Sample V** Dust build-up collected from the convection section, shown in Figure 43.



**Figure 42.** Flue dust build-up sample from the radiation section of the boiler. **Sample IV**



**Figure 43.** Flue dust build-up sample from the convection section of the boiler. **Sample V**

In addition, pure  $\text{CuSO}_4$  and  $\text{Fe}_2(\text{SO}_4)_3$  powders from Sigma-Aldrich were used in the measurements as reference materials.

### 3.1.2 SEM Characterisation

Loose flue dust from the Harjavalta boiler and dust build-ups from two locations were investigated with a scanning electron microscope. The loose dust seemed to be composed of mainly separate particles of varying sizes. In addition, some connected particles were detected. A majority of the particles had an inner core consisting of oxide phases such as  $\text{CuFe}_2\text{O}_4$  and  $\text{Fe}_2\text{O}_3$ , with an outer crust consisting of sulphates such as  $\text{CuSO}_4$ , indicating that most of the particles had not been thoroughly sulphatised at this stage. Figure 44 shows a sample taken from the dust hoppers of the Harjavalta copper smelter.

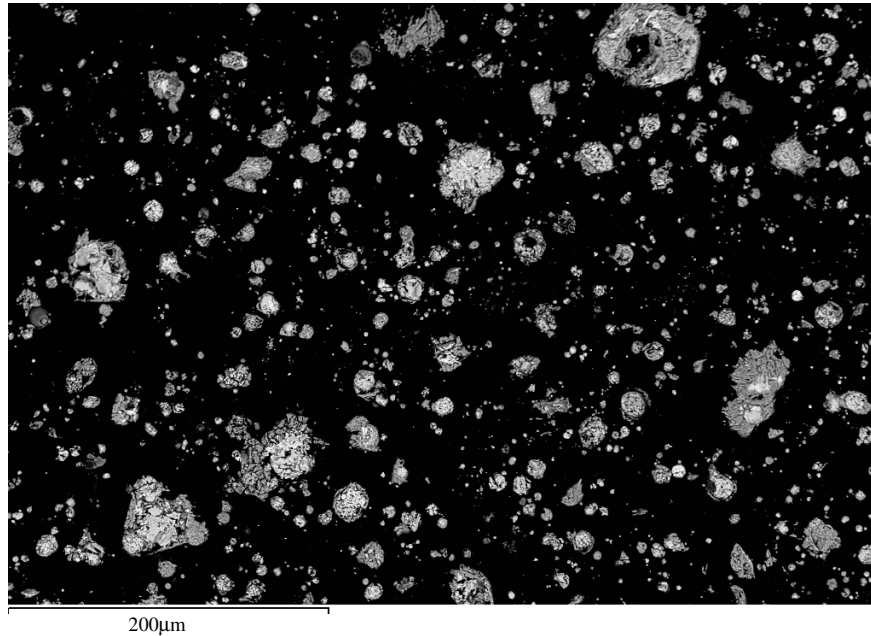


**Figure 44.** Loose flue dust from the dust hoppers of the radiation section of the Harjavalta copper smelter heat recovery boiler. **Sample I.**

In the picture, the oxide-rich inner parts of the particles are shown in lighter shades, whereas the darker shades of sulphate phases are visible on the outer edges of the particles. The particle sizes vary from a few microns up to over 50  $\mu\text{m}$ .

Figure 45 shows the characteristics of the in-flight particles taken from the radiation section of the Harjavalta boiler.



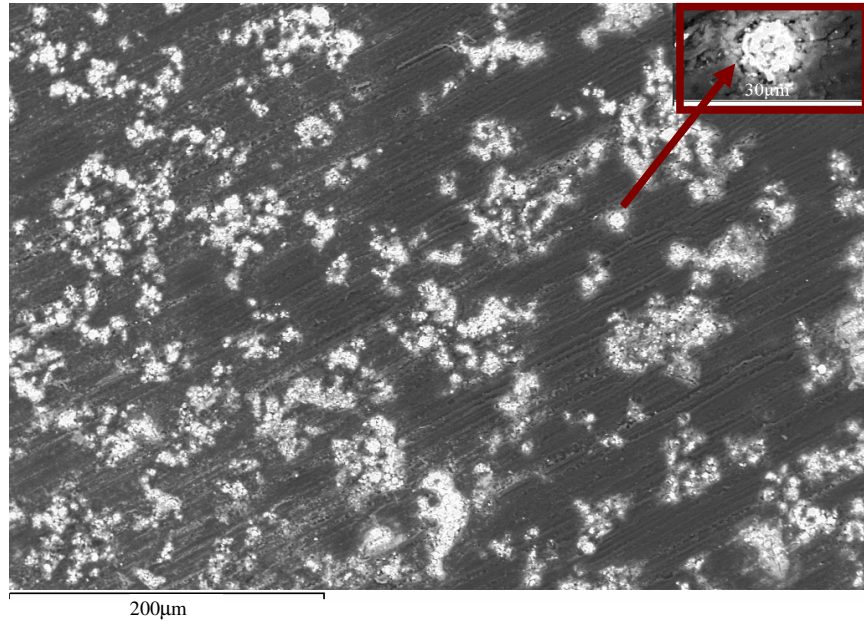


**Figure 45.** *In-flight particle sample from the Harjavalta copper smelter heat recovery boiler radiation section. Sample II.*

The in-flight particles seem to consist of very small particles clustered into larger ones. The sole particles have an average size of a few micrometres, and the clusters have a size of approximately 50-100  $\mu\text{m}$ . In these particles, particularly in the close-up of the top right-hand corner, a lighter oxide inner core and a darker outer core can be seen. Additionally, the close-up of a cluster, shown in Figure 46, shows lighter oxide cores and darker sulphate areas. It is difficult, however, to determine whether the agglomerates have formed in flight or during the sampling process.

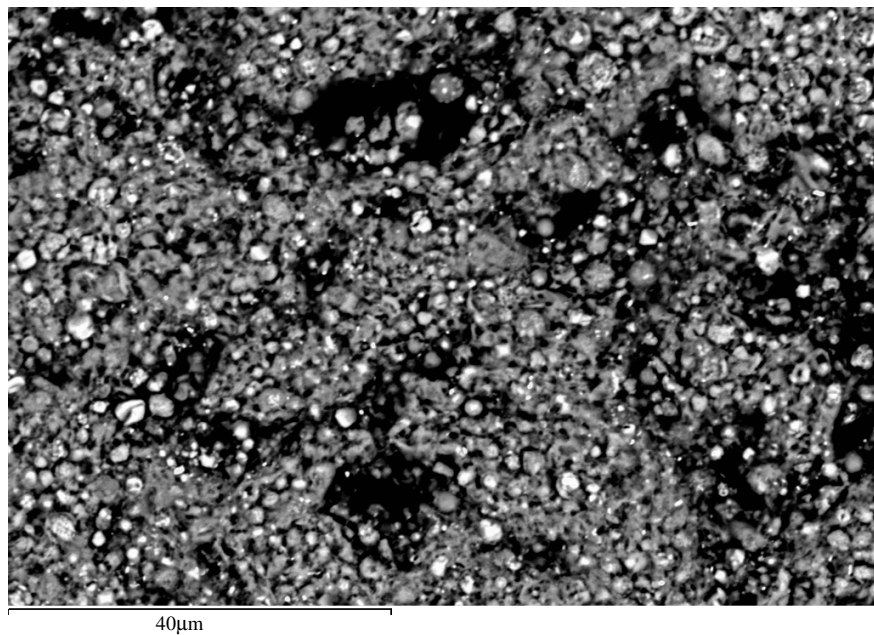


**Figure 46.** *A flue dust cluster formed from the in-flight particles. Sample II.*



Figure 47 shows a sample taken from the dust hoppers of the convection section of the Harjavalta heat recovery boiler.

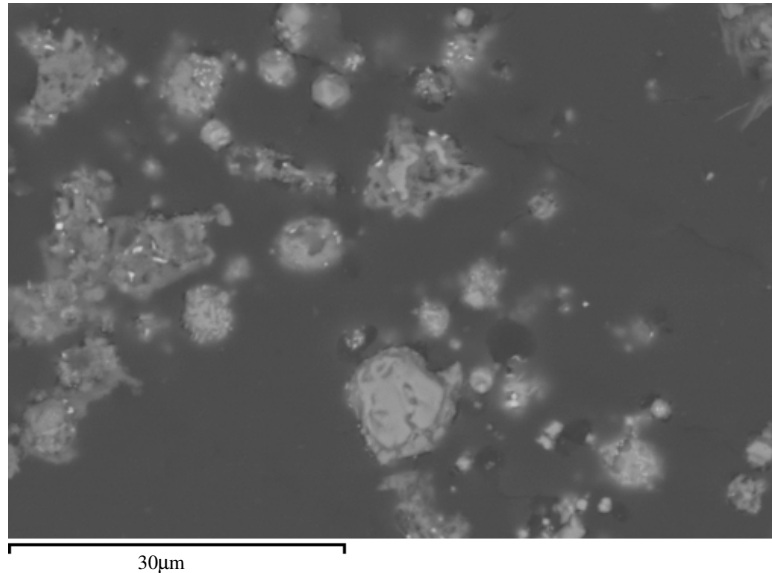


**Figure 47.** *Loose flue dust from the dust hoppers of the convection section of the Harjavalta copper smelter heat recovery boiler. Sample III.*

The convection section flue dust seems to consist of small particles (<20 µm) and particle agglomerates. The particles are larger than the in-flight particles, but smaller than the radiation section particles.

In addition to separate particles, a number of build-up dust layers were investigated. A large lump of build-up from the radiation section of the Harjavalta boiler had a size of approximately 20 cm by 20 cm by 50 cm and consisted of several layers of materials, each having visibly different characteristics. Figure 42 shows the layered structure of the deposit sample. The layer closest to the radiation screen surface consisted of brittle soft bluish material. The EDS investigation suggests that the phase is thoroughly sulphatised material, mainly consisting of copper sulphate and lead sulphate. An example of the material can be seen in Figure 48.

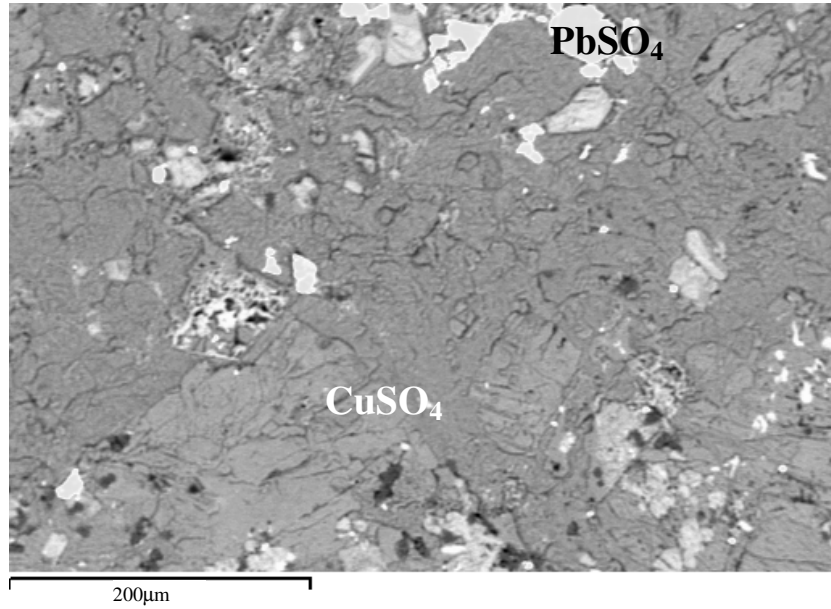


**Figure 48.** Dust build-up from the radiation section of the Harjavalta boiler, near a radiation screen tube surface. **Sample IV.**

Areas containing  $CuAsO_2$  and  $CaSO_4$  were also detected, as shown in Figure 49. In addition, traces of K, Al, and Zn were detected in the first layer.

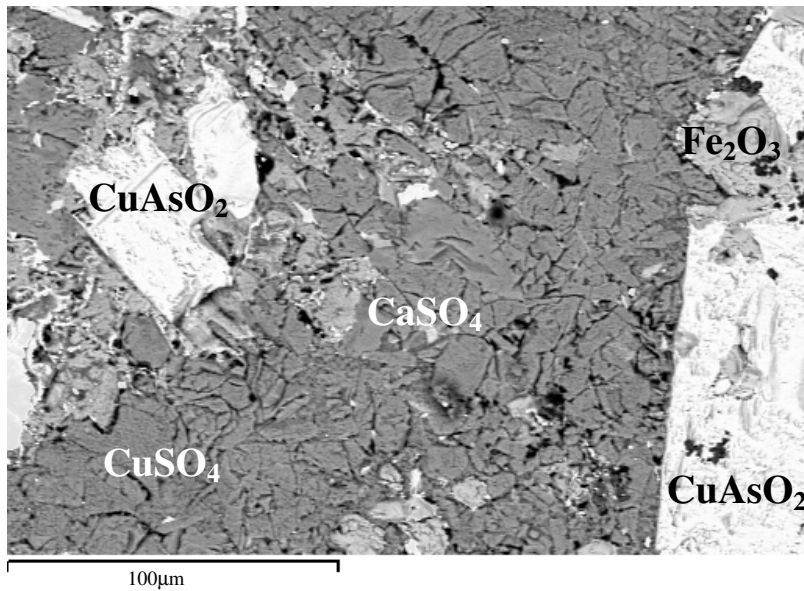


**Figure 49.** Dust build-up from the radiation section of the Harjavalta boiler, near a radiation screen tube surface. **Sample IV.**

The material has gone through extensive consolidation, re-crystallisation, and grain growth and no traces of the original flue dust particle shapes can be detected. Arsenic has probably been deposited on the particle surfaces and in the interstitial spaces between the particles through condensation: later on it may also have migrated through diffusion to form larger particle structures.

The middle layers in the radiation section deposit consisted of very hard and dense material, as shown in Figure 50.

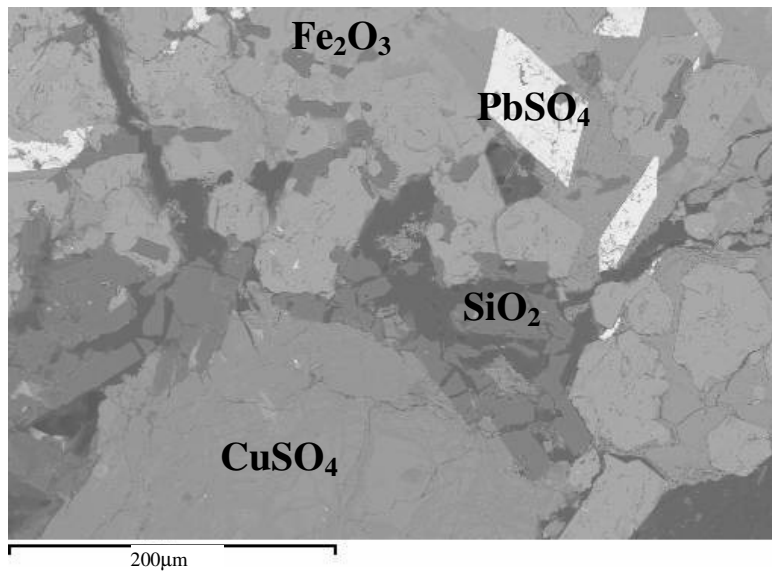


**Figure 50.** Dust build-up from the radiation section of the Harjavalta boiler, middle layer.  
**Sample IV.**

The dense material consisted of condensed and recrystallised particle structures, with vaporisation- and condensation-originated phases of Pb and As, that have gradually diffused into larger crystals.

The layers closest to the boiler gas phase in the same deposit consisted of less sulphatised particles connected together mainly by sulphate phases. An SEM image of the inner layers of the deposit is presented in Figure 51.

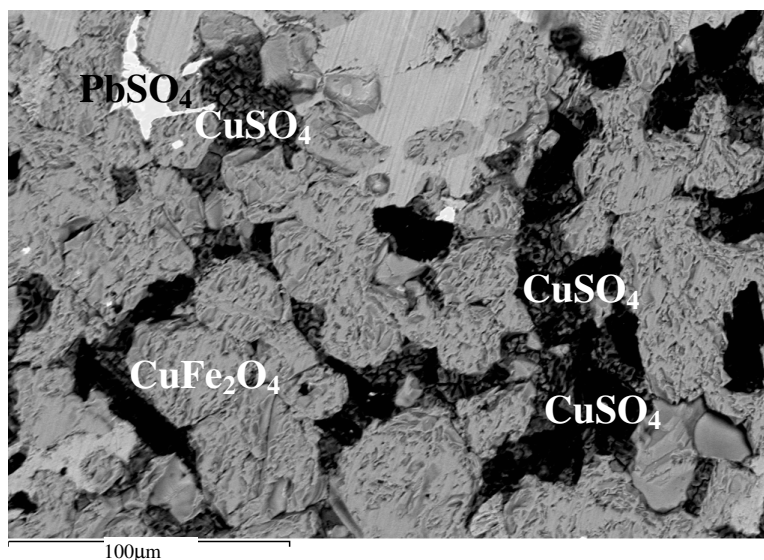


**Figure 51.** Dust build-up from the radiation section of the Harjavalta boiler, near gas phase.  
**Sample IV.**

In the inner layer oxide particles are bound with sulphate bridges between them. The original shapes of the particles can still clearly be detected and no major sintering or melting has taken place.

The dust build-up from the convection section consisted of more brittle material with an approximate thickness of seven centimetres. The build-up consisted of layers of thoroughly sulphatised matter and of a layer with larger particles containing oxide cores. SEM images of both layers are presented in Figures 52 and 53, respectively.

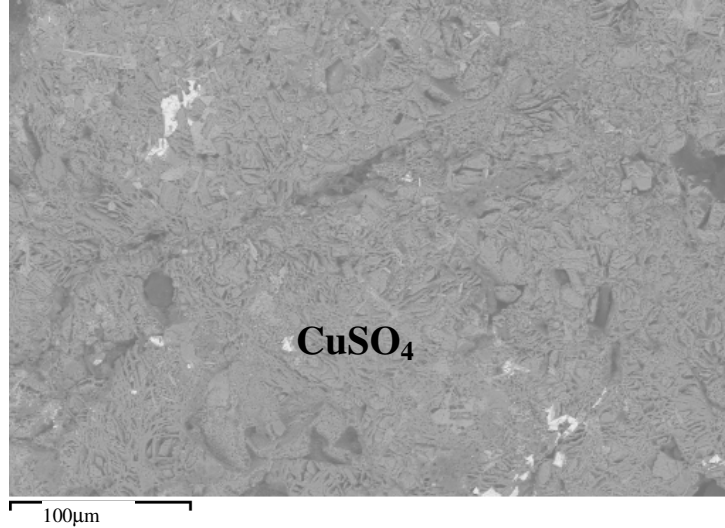


**Figure 52.** Thoroughly sulphated dust layer from the Harjavalta boiler convection section. **Sample V.**

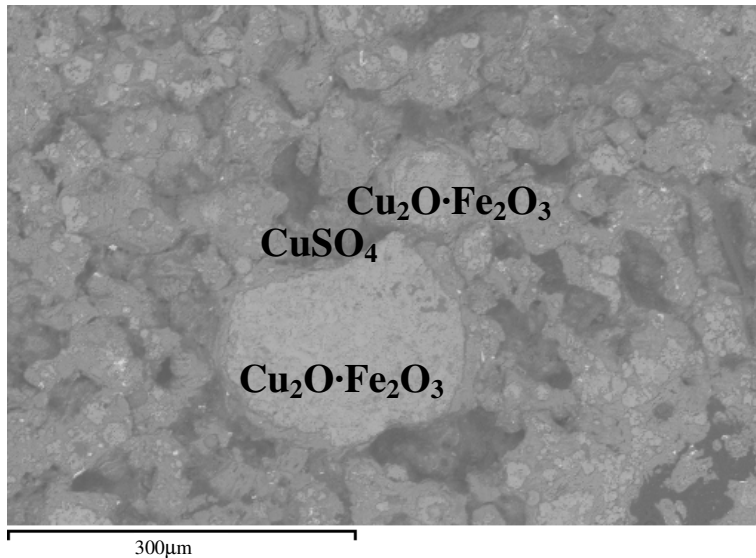


**Figure 53.** Dust build-up containing oxide particle cores from the Harjavalta boiler convection section. **Sample V.**

The elemental composition map obtained using EDS for the large particles shown in Figure 53 is presented in Figure 54.

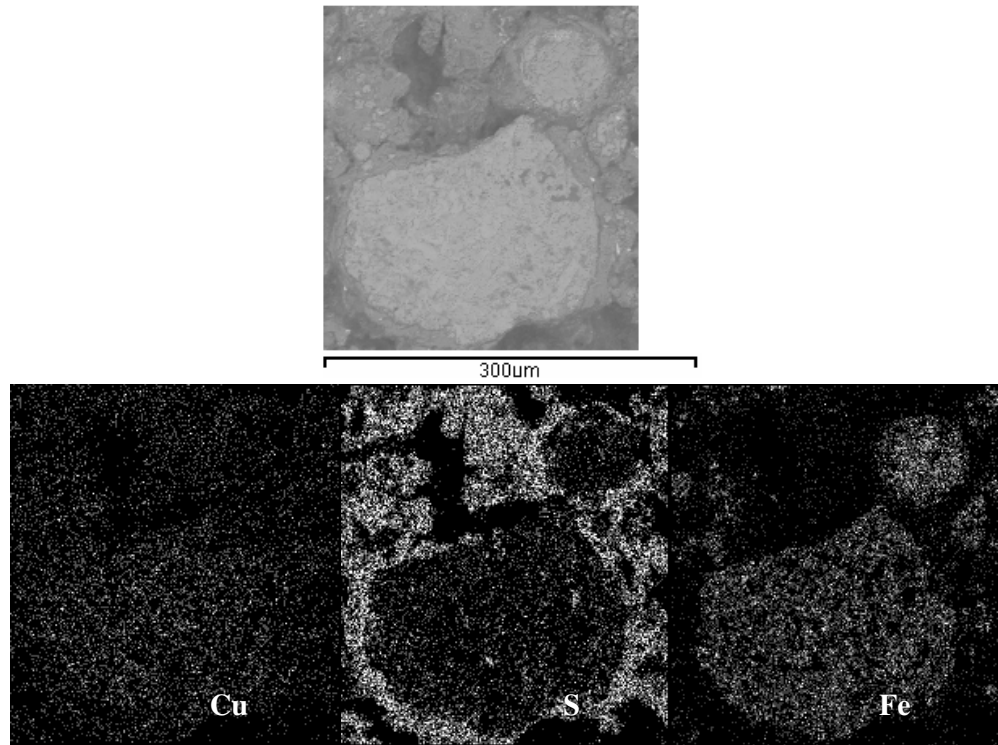


**Figure 54.** Elemental maps of Cu, S, and Fe of dust layer particles in the Harjavalta HRB convection section. *Sample V.*

The elemental distribution clearly shows that the sulphate phases are present on the outer surface of the particles and seem to be the phase connecting the particles. The elemental distribution also shows that whereas copper is present in both the oxide core and on the sulphate shell, iron is more concentrated on the oxide phase. This kind of behaviour indicates that iron oxides may not react into sulphates as readily as copper oxides. Similar observations have been reported by Lastra-Quintero et al. (16)

Similar chemical compositions can be detected in all the samples. The dominant phases seem to be  $\text{CuSO}_4$ ,  $\text{Cu}_2\text{O}\cdot\text{Fe}_2\text{O}_3$ , and  $\text{Fe}_2\text{O}_3$ , which have earlier been reported by many researchers (4, 10-18).

### 3.1.3 Particle size distribution

The particle size distributions of the loose dust samples and pure  $\text{CuSO}_4$  and  $\text{Fe}_2(\text{SO}_4)_3$  samples were measured with a MalvernMastersizer 2000 laser diffraction particle size analyser. The measurements were performed in ethanol to avoid sulphate dissolution. The particle size distributions for  $\text{CuSO}_4$ ,  $\text{Fe}_2(\text{SO}_4)_3$ , and radiation section and convection section flue dust are presented in Figures 55 to 58 respectively.

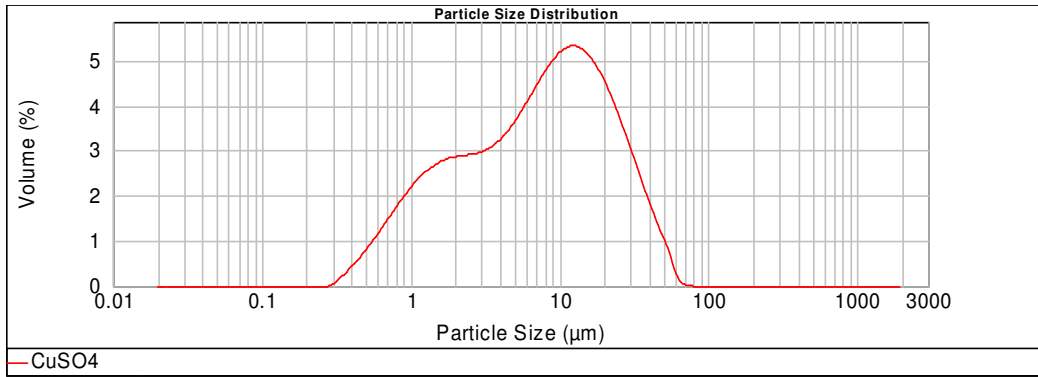


*Figure 55. Particle size distribution of CuSO<sub>4</sub>.*

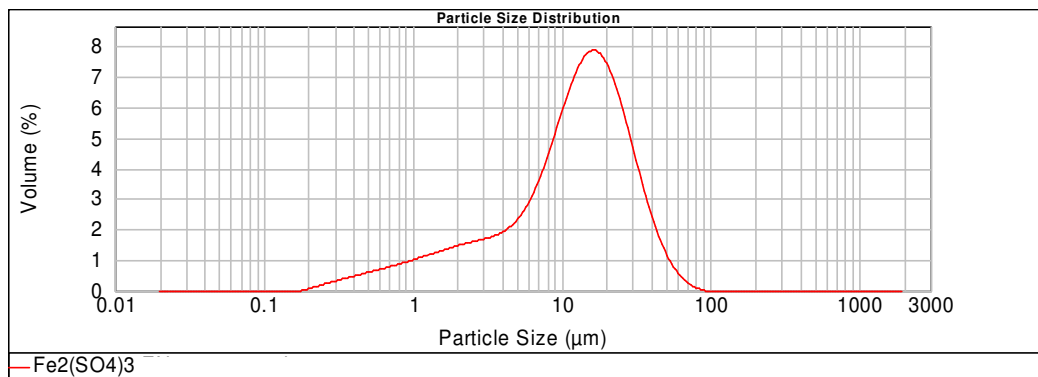


*Figure 56. Particle size distribution of Fe<sub>2</sub>(SO<sub>4</sub>)<sub>3</sub>.*

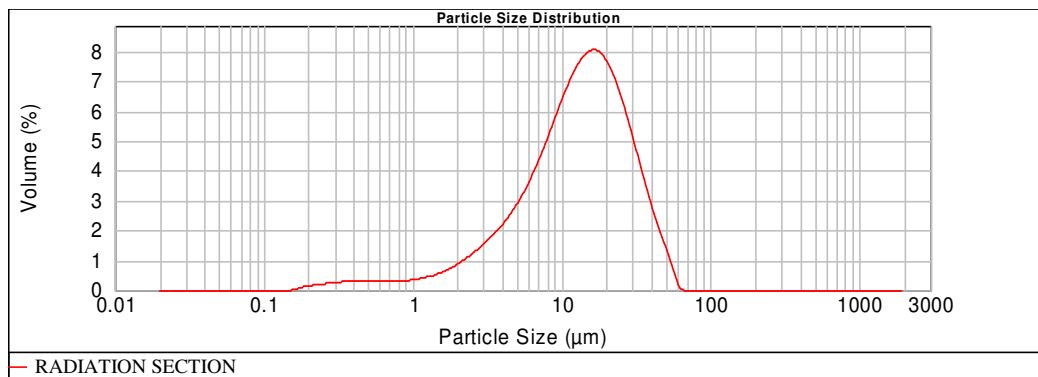


*Figure 57. Particle size distribution of the radiation section flue dust. Sample I.*

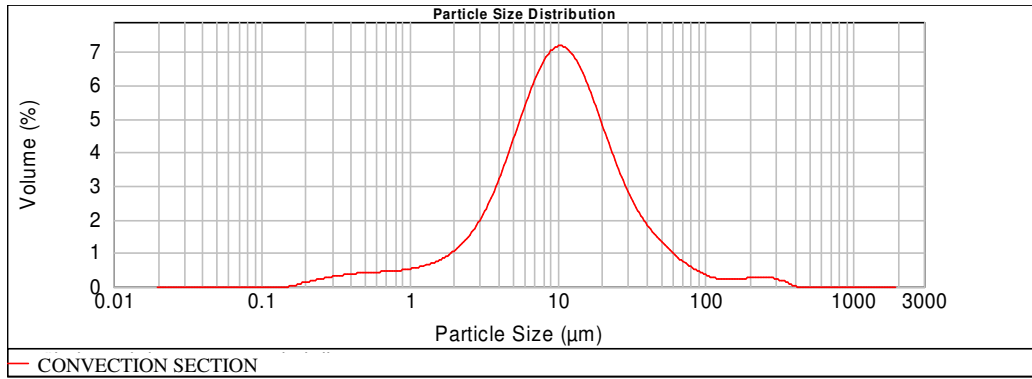


**Figure 58.** Particle size distribution of the convection section flue dust. **Sample III.**

For all of the materials the majority of the particles lie within the 10-20- $\mu\text{m}$  size range. The  $\text{CuSO}_4$  sample has more very small  $<5\text{-}\mu\text{m}$  particles than the other three materials.

### 3.1.4 Particle density

The particle density of the sample materials was measured to determine the sample porosities. The particle densities were determined using an Accupyc 1330 helium pycnometer. The results of the particle densities are shown in Figure 59.

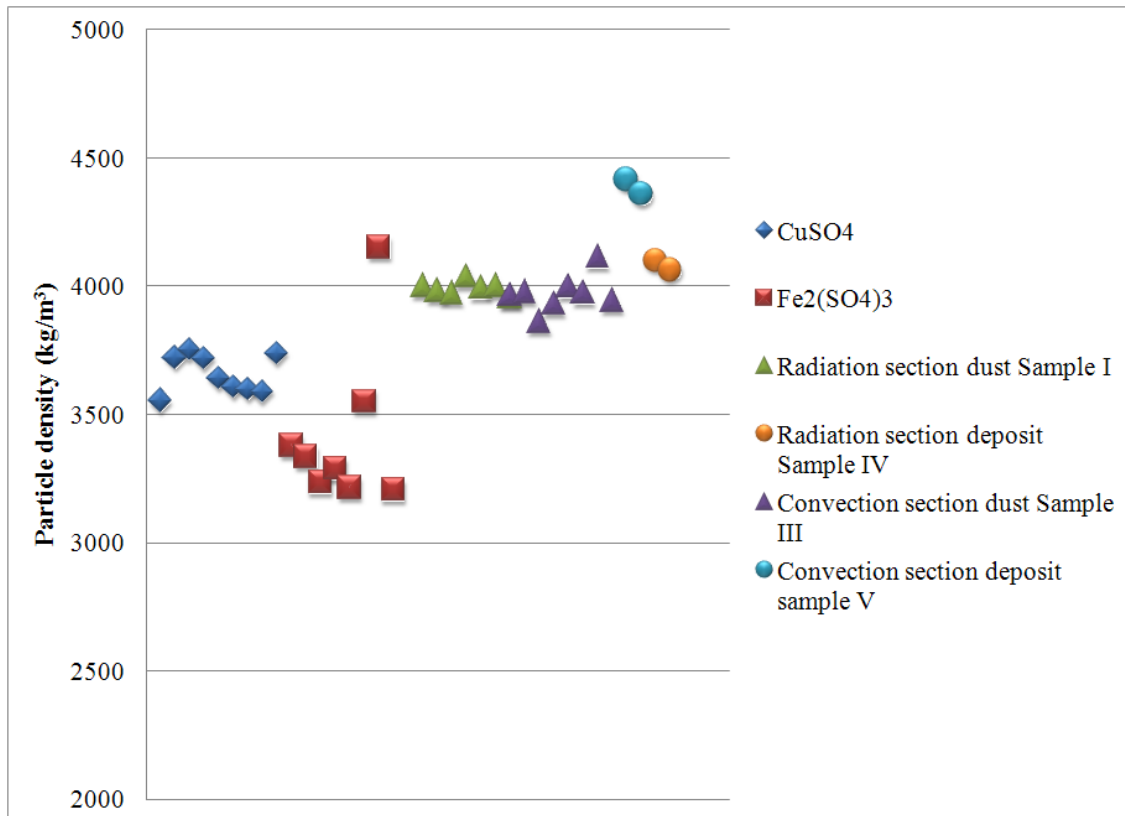


**Figure 59.** Particle densities of the test materials.

The pure sulphates have a slightly lower particle density than the flue dust samples. Most flue dust samples have very similar values, with the convection section deposit sample showing slightly higher values.

### 3.1.5 TGA-DSC experiments

To determine the stability of the components in the flue dusts, thermal gravimetry was applied to the materials used in the thermal conductivity and thermal diffusivity measurements. The stability of the sulphate phases established the upper boundary of the further measurements. Information concerning sulphate stability also helps in determining the temperature history of the flue dust deposits.

The thermal analysis results from TGA-DSC experiments for cupric and ferric sulphate, as well as flue dust decomposition, are presented in Figures 60, 61, and 62 respectively.

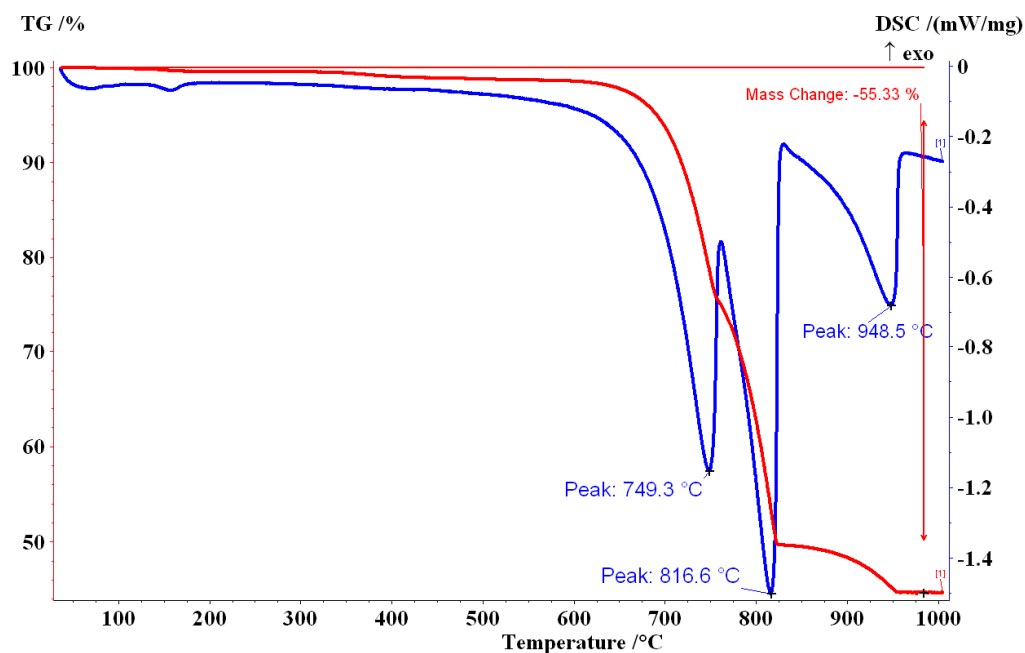


**Figure 60.** TGA-DSC curves in Ar for thermal decomposition of cupric sulphate.

The thermal decomposition of cupric sulphate takes place through an intermediate basic sulphate compound,  $\text{CuO}\cdot\text{CuSO}_4$ . This can be clearly distinguished in the analysis curves. The first decomposition reaction from sulphate into the basic copper sulphate starts at around 700 °C. The calorimetric peak is at 749 °C, indicating an endothermic reaction around that temperature. The decomposition of the basic copper sulphate into copper oxide begins at 760 °C. The endothermic calorimetric peak is at 817 °C. The entire decomposition reaction has taken place by the temperature of 824 °C. The third peak at 949 °C indicates the reaction from  $\text{CuO}$  into  $\text{Cu}_2\text{O}$ . The calculated mass changes are equivalent to the molecular masses of the compounds.



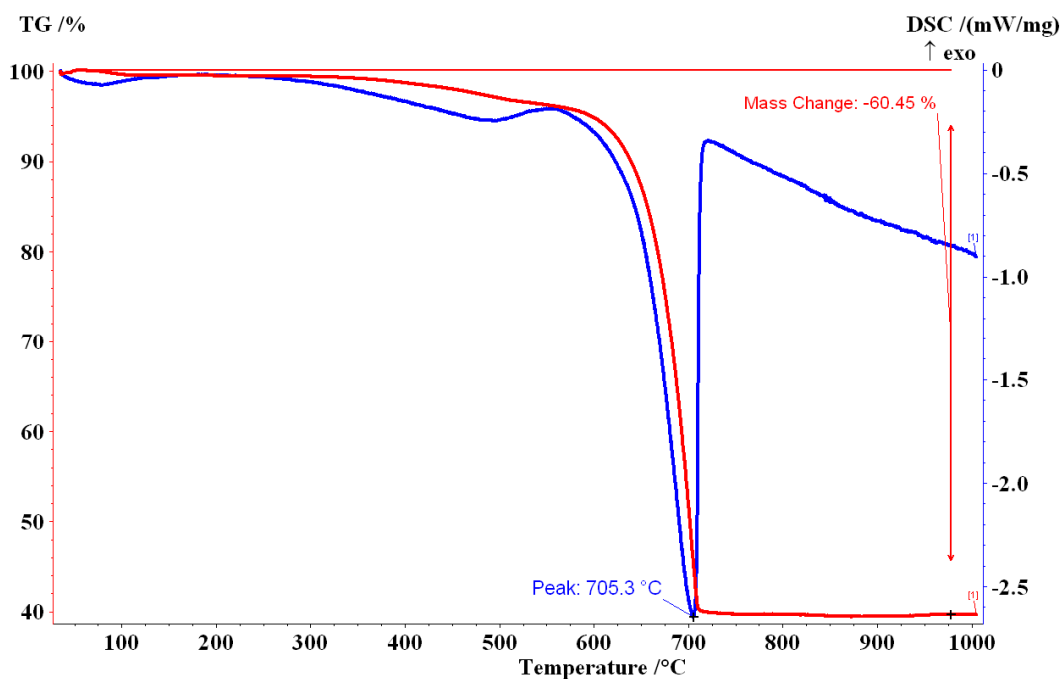


**Figure 61.** TGA-DSC curves in Ar for thermal decomposition of ferric sulphate.

The thermal decomposition of ferric sulphate takes place directly in one step, without intermediate compounds. The decomposition reaction from ferric sulphate into hematite starts at around 660 °C and the calorimetric peak is at 705 °C. The entire decomposition reaction has taken place by 720 °C. All temperatures are lower than in cupric sulphate decomposition; thus ferric sulphate is less stable at high temperatures than cupric sulphate. The calculated mass changes in the ferric sulphate decomposition curve are equivalent to the molecular masses of the compounds.

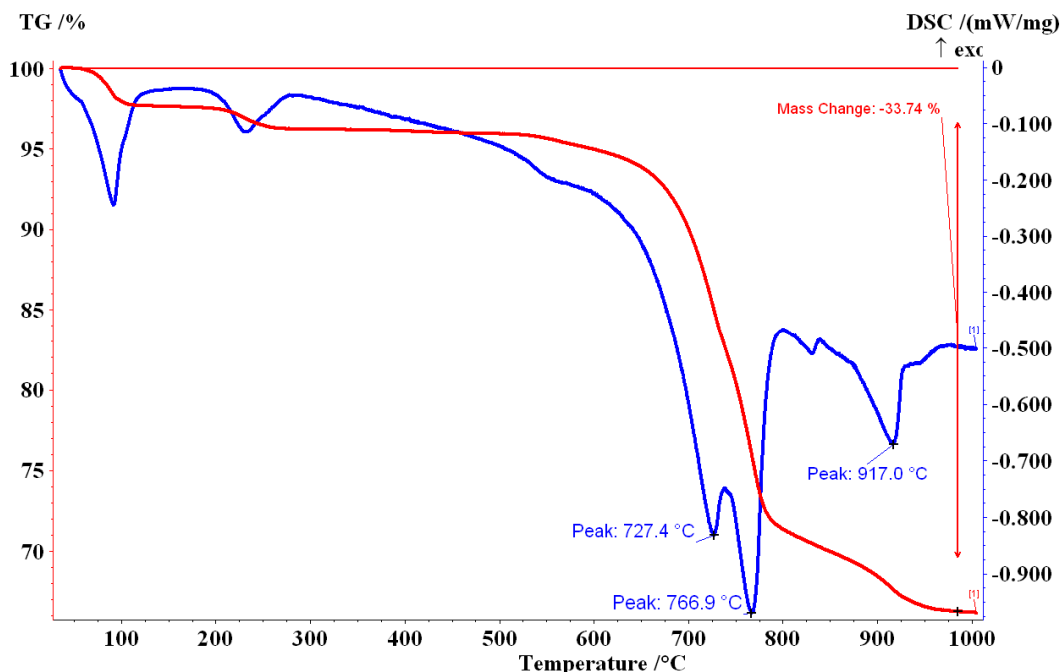


**Figure 62.** TGA-DSC curves in Ar for thermal decomposition of flue dust. **Sample I.**

The decomposition curve of Copper Flash Smelting flue dust shows several clearly distinguishable peaks. The first peaks at temperatures below 300 °C are likely to indicate the dissociation of some crystal water in the sample. The first actual decomposition reaction starts at around 710 °C. A clear endothermic peak is detected at 727 °C and the break in the curve around 730 °C may indicate the completion of this reaction. A second reaction starts after that, with an endothermic peak at 767 °C and finishing by 800 °C. Yet another peak is visible at 917 °C.

Both sulphates and the flue dust samples begin decomposing at temperatures over 600 °C. Ferric sulphate is thermally the most unstable, having its endothermic decomposition peak at 705 °C in comparison to those for cupric sulphate and flue dust, at 749 °C and 727 °C respectively. Ferric sulphate decomposes in one step, finishing the reaction by 720 °C. Both cupric sulphate and flue dust show a second decomposition peak, at 817 °C and 767 °C respectively, and the finishing of this double reaction takes place at 820 °C and 800 °C respectively. The similar double reaction most probably indicates the decomposition of cupric sulphate into basic sulphate and further into cupric oxide. The peaks at 949 °C and 917 °C are likely to indicate the reaction from cupric oxide (CuO) to cuprous oxide (Cu<sub>2</sub>O). The decomposition behaviour of flue dust is very close to that of cupric sulphate, confirming that a large amount of the flue dust is composed of cupric sulphate. The lower decomposition temperatures are probably due to the effect of various impurity compounds in the dust.

The TGA results indicated that the thermal diffusivity and thermal conductivity measurements should be conducted at temperatures well below 600 C degrees to avoid sulphate decomposition. The results also indicate that any deposits with sulphate phases present have not been subjected to temperatures higher than 600-700 °C after sulphatation.

## 3.2 Equipment

### 3.2.1 Transient Plane Source

A Hot Disk thermal constants analyser was used for the thermal conductivity measurements. The Hot Disk device applies a transient plane source method (TPS) that can be used to measure the thermal conductivity and thermal diffusivity of a large variety of solid and liquid materials. The method is able to determine both thermal conductivity and thermal diffusivity from a single transient measurement. The experimental apparatus consists of a flat sensor that is placed between two sample pieces. The sensor consists of a continuous double spiral of an electrically conducting nickel metal foil, protected by Kapton or Mica insulation. (51)

The resistive sensor element is used both as a heat source and as a temperature sensor. In the experiment the voltage change over the sensor is measured, while its temperature is increased by an electrical current pulse. (51) The generated heat advances through the sample on both sides of the sensor, depending on the thermal characteristics of the material.

By passing the electrical current through the sensor and simultaneously measuring the increase in resistance, the average temperature increase of the double spiral as a function of time is obtained and the thermal conductivity and diffusivity can be determined. (51)

The time-dependent resistance of the sensor may be expressed as:

$$R(t) = R_0 \left( 1 + c_t \overline{\Delta T(\tau)} \right), \quad (17)$$

where  $R_0$  is the initial electrical resistance and  $c_t$  is the temperature coefficient of resistivity of the probe.  $\overline{\Delta T(\tau)}$  is the mean temperature increase of the double spiral and may also be expressed as:

$$\overline{\Delta T(\tau)} = \frac{P_0}{rk\pi^{3/2}} D(\tau) \quad (18)$$

The dimensionless time in Eq. (17)

$$\tau = \left( \frac{t}{\theta} \right)^{1/2}, \quad (19)$$

incorporates the time scale given by:

$$\theta = \frac{r^2}{\alpha}, \quad (20)$$

where  $t$  is the real time of the measurement,  $\alpha$  is the thermal diffusivity of the sample,  $r$  is the radius of the spiral,  $k$  is the thermal conductivity of the sample, and  $P_0$  the total output of power during the transient.

If all the heat transfers through the sample, the following equation (21) applies between the thermal conductivity quantities:

$$\alpha = \frac{k}{\rho C_p}, \quad (21)$$

where  $\rho C_p$  is the specific heat of the sample across a volume unit. (51-54)

In comparison to other, especially static, thermal conductivity measurement methods, Transient Plane Source is fast and accurate and it is not affected by the contact resistant between the sensor and the sample.

### 3.2.1.1 Experimental procedure

The Transient Plane Source (TPS) method was applied into the measurement of Copper Flash Smelting flue dust thermal conductivity. Three materials were measured: anhydrous copper sulphate ( $\text{CuSO}_4$ ) powder from Sigma-Aldrich; dried ferric sulphate ( $\text{Fe}_2(\text{SO}_4)_3$ ) powder from Sigma-Aldrich, and process flue dust collected from Boliden Harjavalta's heat recovery boiler (Sample II). Measurements were also conducted on flue dust deposits collected from the radiation and convection sections of the boiler (Samples IV and V). The pure sulphate powders were selected as reference materials to get information about the effect of the chemical composition on the thermal conductivity. The powder materials were dried in a furnace to remove the absorbed crystal water. It is likely that although the materials were dried at 100 °C and stored in a desiccator, some crystal water was absorbed back into the specimens during the preparation of the samples or during the experiments, and may therefore have affected the results.

All the powdery samples were measured both in powder and pellet form. The pellets were prepared by hydrostatic pressing with a force of about 200 MPa. The diameter of the pellets was 22 mm and the height was about 20 mm.

The deposit samples consisted of blocks of approximately 5 cm x 5 cm x 5 cm, with one side ground even to establish good contact with the sensor.

In the experiments the transient plane source sensor was placed between two equally-sized pellet samples or it was embedded in loose powder. A schematic presentation of the experimental apparatus and the set-up is shown in Figure 63.

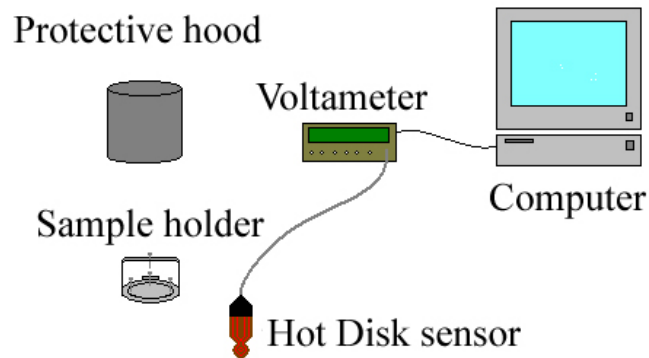


**Figure 63.** Schematic presentation of the experimental apparatus using the Transient Plane Source method (Hot Disk<sup>®</sup> Thermal Constants Analyser by Hot Disk AB).

The measurement times for the sulphate and dust samples varied from 10-40 seconds and the electrical power used ranged between 0.01 and 0.5 W. The temperature increase in the samples during the measurements was of the order of magnitude of a few degrees. The experiments were repeated between five and ten times for each sample and the results were calculated as an average of the observations. In addition, the standard deviation was calculated to determine the repeatability of the experiments.

### 3.2.2 Laser Flash Analyser

An Anter Flashline 5000 measurement unit was used for the thermal diffusivity measurements. The device is illustrated in Figure 64.

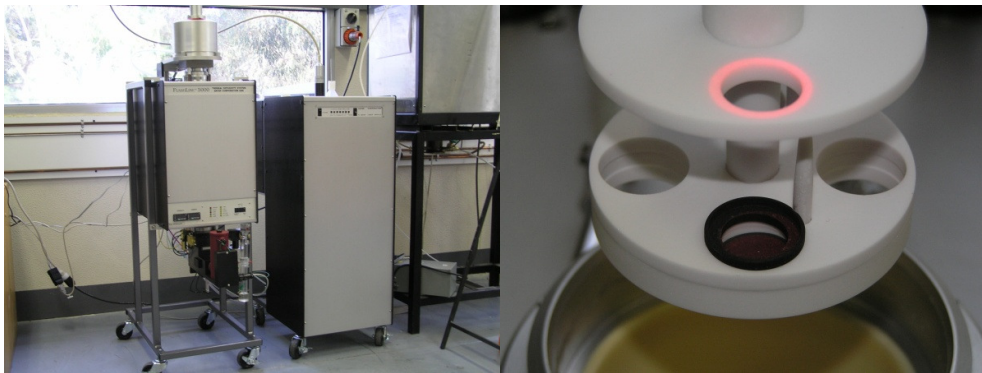


**Figure 64.** Anter Flashline 5000.

In the laser flash technique a very short burst of energy, a laser pulse, is applied to the front of the sample. A detector on the rear side of the sample is used to record the temperature change of the material. The detector shows the actual temperature rise, disregarding the initial temperature of the sample. The sample is a small disc of known thickness ( $L$ ) and by

determining the half-max-time ( $t_{1/2}$ ) of the temperature rise, the thermal diffusivity can be calculated:

$$\alpha = \frac{1.38L^2}{\pi^2 t_{1/2}} \quad (22)$$

The method was first introduced in 1961 by Parker (55).

A schematic presentation of the method is shown in Figure 65.

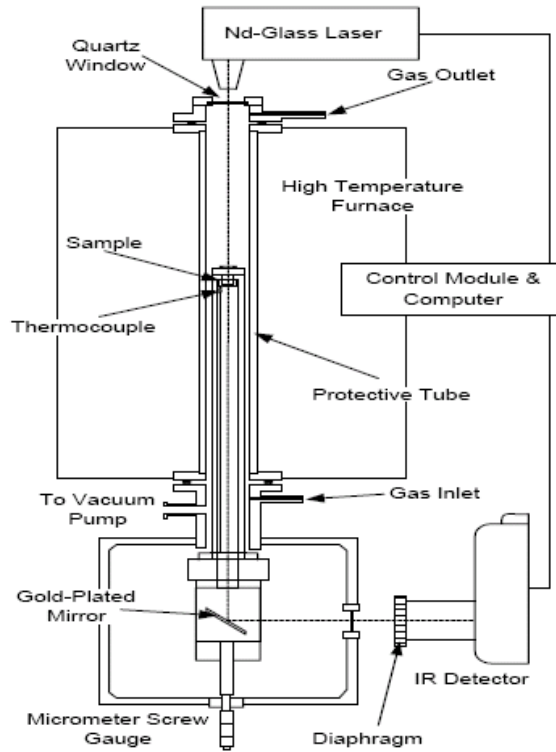


**Figure 65.** Schematic presentation of the laser flash analysis. (56)

The temperature distribution within a thermally insulated solid with thickness  $L$  is given by:

$$T(x,t) = \frac{1}{L} \int_0^L T(x,0) dx + \frac{2}{L} \sum_{n=1}^{\infty} \exp\left(\frac{-n^2 \pi^2 \alpha t}{L^2}\right) \cos \frac{n\pi x}{L} \int_0^L T(x,0) \cos \frac{n\pi x}{L} dx \quad (23)$$

where  $\alpha$  is the thermal diffusivity of the material.

The calculations assume one-dimensional heat flow, no heat losses, uniform absorption, infinitely short pulse duration, absorption in a very thin layer, material isotropy and homogeneity, and a stable sample temperature. Since samples usually do not meet these requirements, a number of correcting models have been introduced to produce more accurate results.

The method has been shown to produce acceptable results when used with porous samples. The magnitude of porosity, pore shapes, sizes, and parameters of pore distribution influence the behaviour of the thermal diffusivity and the results must thus be analysed with care.

### 3.2.2.1 Experimental procedure

The Laser Flash Analysis (LFA) method was used for the measurement of the samples thermal diffusivity. The measurements were performed at the CSIRO Minerals Clayton site, using an Anter Flashline 5000 device. Three different materials were measured: anhydrous copper sulphate ( $\text{CuSO}_4$ ) powder from Sigma-Aldrich; dried ferric sulphate ( $\text{Fe}_2(\text{SO}_4)_3$ ) powder from Sigma-Aldrich, and process flue dust collected from Boliden Harjavalta's heat recovery boiler (Sample III). The powder materials were dried in a furnace at  $300^\circ\text{C}$  to remove the absorbed crystal water.

The powders were pressed into pellets of varying densities using hydrostatic pressing with different loads. The diameter of the pellets was approximately 12 mm and the height about 2 mm. The bulk densities of the  $\text{CuSO}_4$  pellets varied from 2100 to 2600  $\text{kg/m}^3$ , from 2230 to 2350  $\text{kg/m}^3$  for  $\text{Fe}_2(\text{SO}_4)_3$ , and from 2600 to 2800  $\text{kg/m}^3$  for the flue dust. The practical limit for the density variation was the mechanical strength of the pellets.

A thin layer of carbon paste was applied to the surfaces of the sample to enhance energy absorption. A laser voltage of 1600V was applied in the measurements. The temperature increase was recorded for 15-20 seconds and the half max. time was determined either by automatic analysis of the equipment or, in a few cases, when the automatic fit was poor, it was done manually. Each result is an average of three similar measurements at the same temperature. The temperatures used in the measurements varied from  $23^\circ\text{C}$  up to  $400^\circ\text{C}$ . Typically, in the low-temperature measurements, the noise of the signal was very high and for all the samples it was not possible to get acceptable results below  $100^\circ\text{C}$ . The higher end of the temperature range was determined by the thermal stability of the samples.

### 3.2.3 Differential Scanning Calorimeter

A Netzsch STA 449C differential scanning calorimeter (DSC) was used to determine the specific heat of the samples. The DSC module of the device measures the heat flow into the sample as it is heated. The specific heat capacity is determined by comparing the thermal response of the sample to the thermal response of a known standard, in this case aluminium oxide.

## 3.3 Comparison of the measurement techniques

The main advantages of the Hot Disk technique are its simplicity and relatively low cost. The main disadvantages include a relatively large sample size and the need for two similar samples. Hot Disk measurements are most suitable for moderate temperatures, but at temperatures above  $400^\circ\text{C}$  the sensor lifetime is fairly limited. The Hot Disk device is able to measure thermal conductivity, thermal diffusivity, and specific heat capacity values simultaneously.

## EXPERIMENTAL

---

The main advantages of Laser Flash Analysis are its high precision and proven performance. It is more suitable for the high-temperature measurements than Hot Disk, but its low-temperature performance may be fairly poor. The disadvantages of LFA include its high cost and the need for a specific sample size. It is also only able to determine thermal diffusivity values. To obtain thermal conductivity values, one needs further information on the density and specific heat capacity of the material

.



## 4. RESULTS

### 4.1 Thermal Diffusivity

The results of the Laser Flash thermal diffusivity experiments for  $\text{CuSO}_4$ ,  $\text{Fe}_2(\text{SO}_4)_3$ , and process flue dust are presented in Figures 66, 67, and 68 respectively. The graphs show the results as a function of temperature for various porosities/bulk densities.

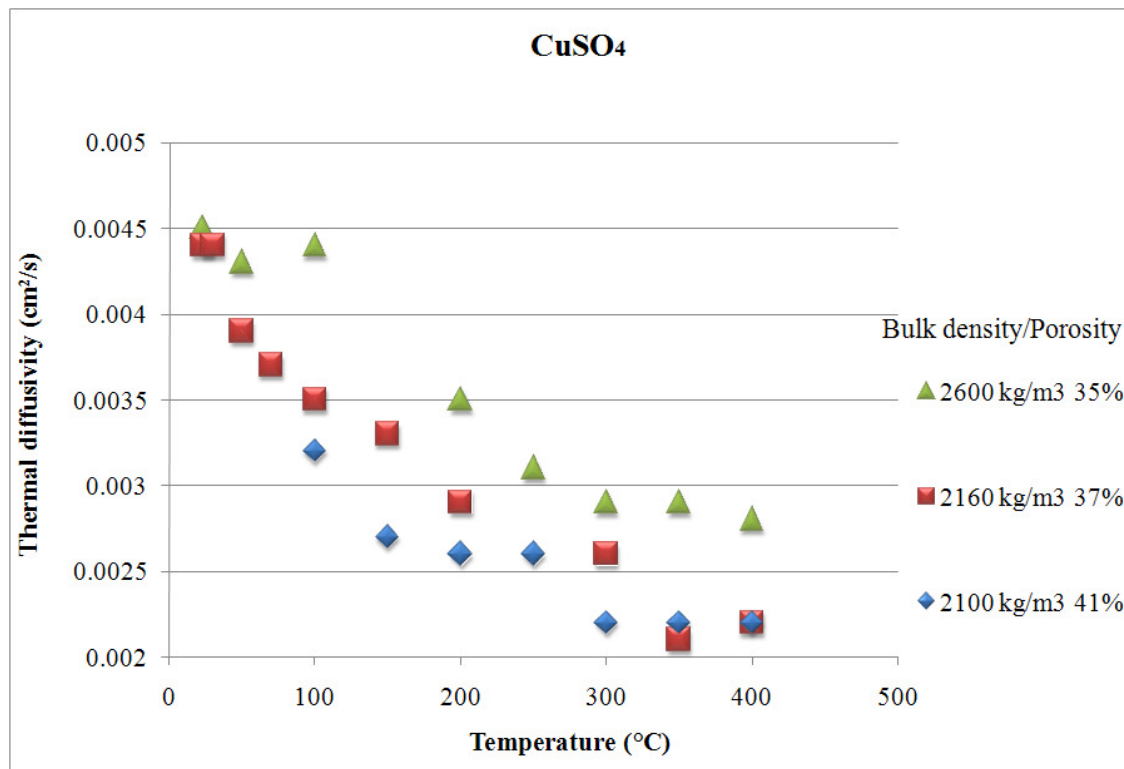


*Figure 66. Thermal diffusivity of copper sulphate pellets. (57-58)*

The thermal diffusivity values of copper sulphates are highest at 0.0045 cm<sup>2</sup>/s at room temperature and lowest at 0.0021 cm<sup>2</sup>/s at 350 °C. The values are higher for the samples containing the highest bulk density.

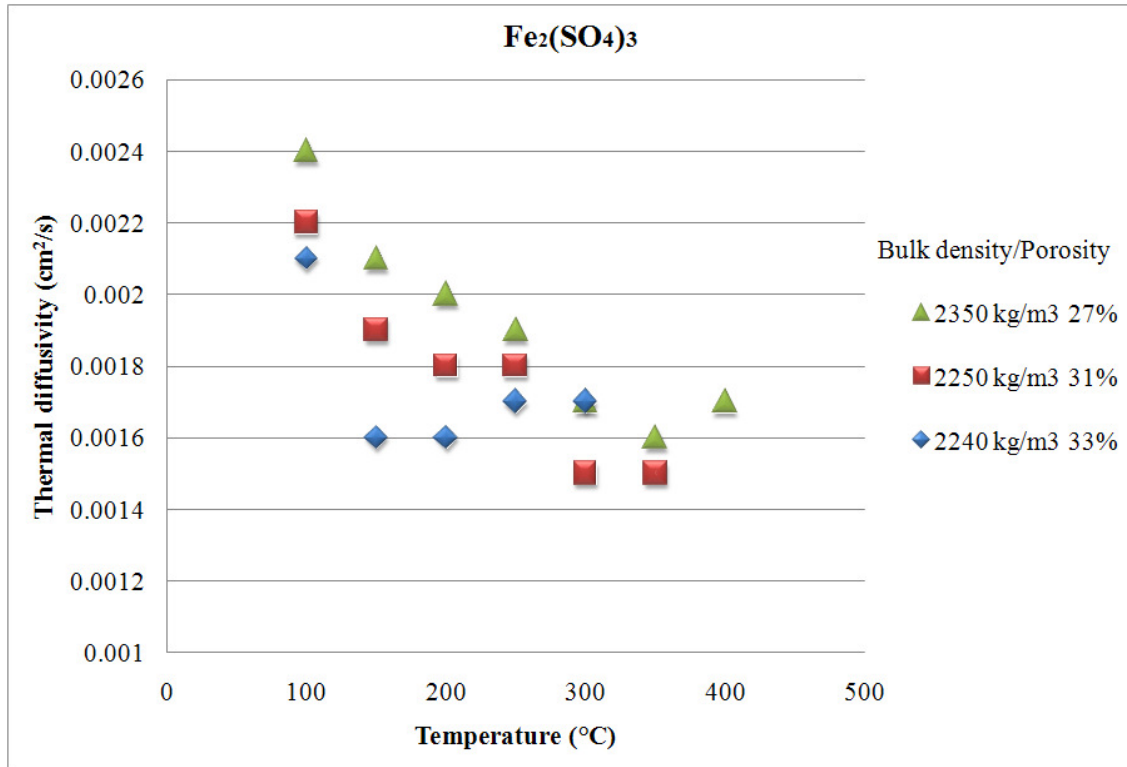


**Figure 67.** Thermal diffusivity of ferric sulphate pellets. (57-58)

The thermal diffusivity values of ferric sulphate are slightly lower than those for copper sulphate. The highest values can be seen at 100 °C at 0.0027 cm<sup>2</sup>/s and the lowest ones at 300 °C at 0.0015 cm<sup>2</sup>/s. As seen with the copper sulphate samples, the ferric sulphate sample with the highest bulk density also has the highest thermal diffusivity values, even though some scattering can be seen.

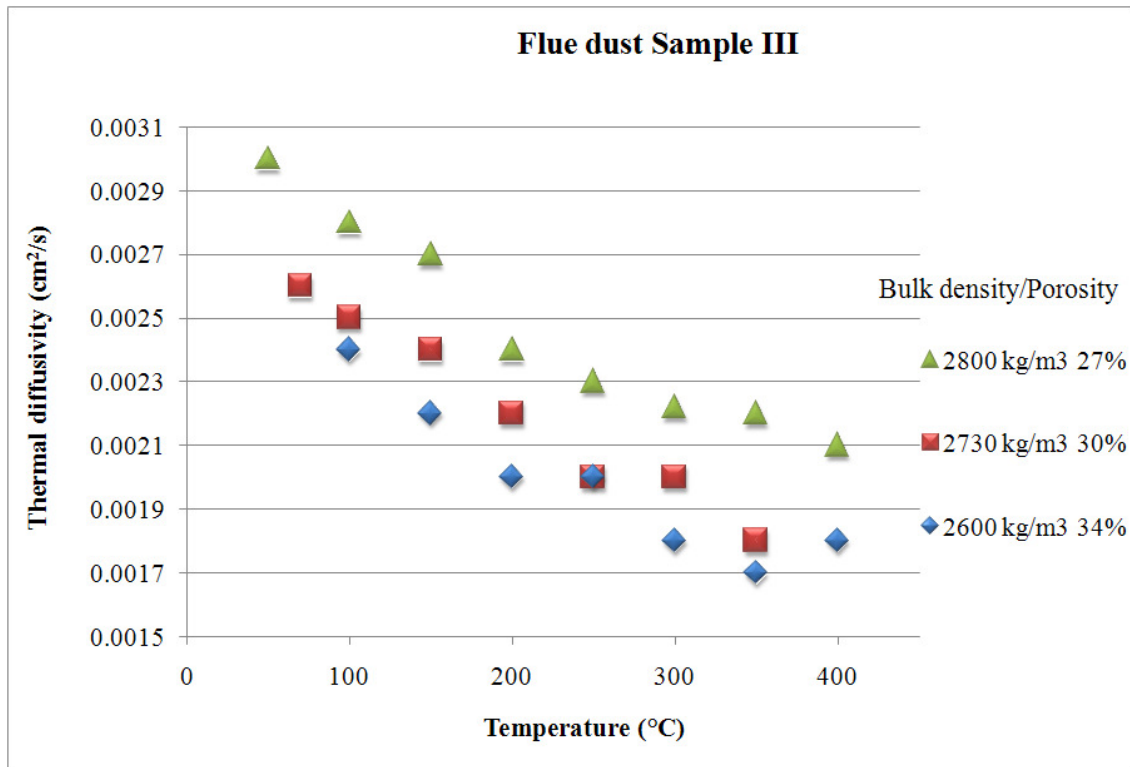


**Figure 68.** Thermal diffusivity of copper flash smelting flue dust. **Sample III.** (57-58)

The thermal diffusivity values of the flue dust are slightly lower than those of copper sulphate and fairly similar to those of ferric sulphate. The highest values can be seen at 50 °C at 0.0030 cm<sup>2</sup>/s and the lowest at 350 °C at 0.0017 cm<sup>2</sup>/s. As seen for both copper and ferric sulphates, flue dust samples with a higher bulk density result in higher thermal diffusivity values.

Figure 69 compares the thermal diffusivity measurement results of different materials and methods. The graph shows the diffusivity values of CuSO<sub>4</sub>, Copper Flash Smelting flue dust from the Harjavalta boiler convection section dust hoppers, and the dust deposit from the same boiler (approximate bulk density 2030 kg/m<sup>3</sup>). The dust deposit was measured with both the Laser Flash technique and the Hot Disk instrument.

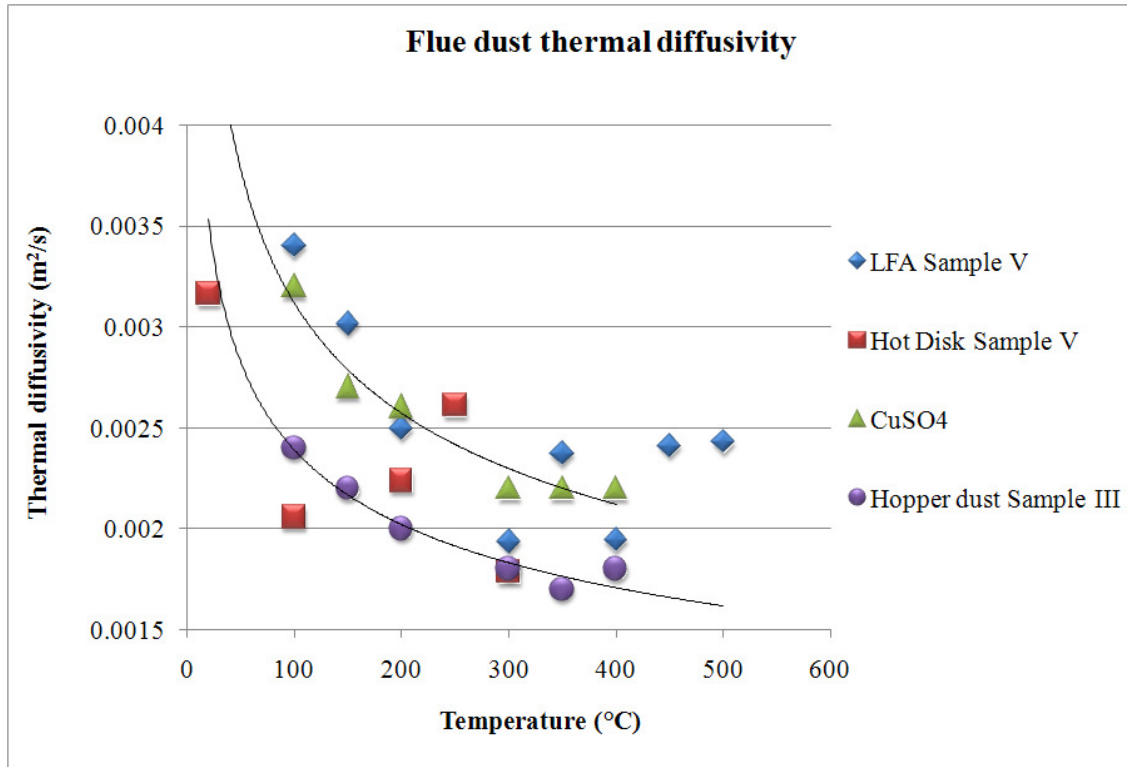


*Figure 69. Comparison of materials and measurement method in thermal diffusivity measurements. (56-57)*

The results show that all the samples show fairly similar results, with all having a decreasing temperature dependence and fairly low values. The Hot Disk results show a greater scatter and the temperature dependence trend is not as clear.

## 4.2 Thermal Conductivity

Thermal conductivity measurements were performed with the Hot Disk device for pellets compressed with different pressures of  $\text{CuSO}_4$ ,  $\text{Fe}_2(\text{SO}_4)_3$  powders, loose flue dust gathered from the radiation section of the Harjavalta boiler, and dust build-ups from both the radiation and convection sections of the Harjavalta boiler.

The results of the thermal conductivity measurements for copper sulphate, ferric sulphate and Copper Flash Smelting flue dust are presented in Figures 70 to 72 respectively (59-60). The graphs show the results as a function of temperature for various densities.

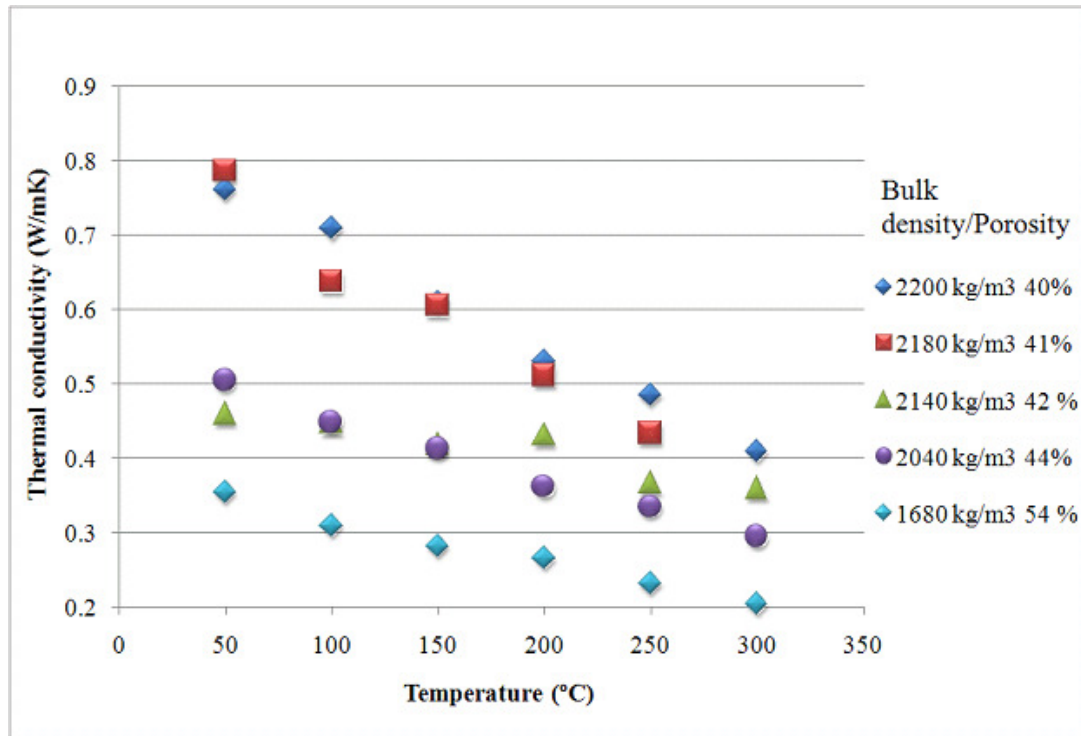


**Figure 70.** Thermal conductivity of cupric sulphate as a function of temperature and bulk density/porosity. (59-60)

The thermal conductivity results for copper sulphate show a decreasing temperature dependence ranging from 0.8 W/mK at 50 °C to 0.2 W/mK at 300 °C. The trend is more pronounced in dense samples. The thermal conductivity values of most samples lie around 0.3-0.4 W/mK at high temperatures.

## RESULTS

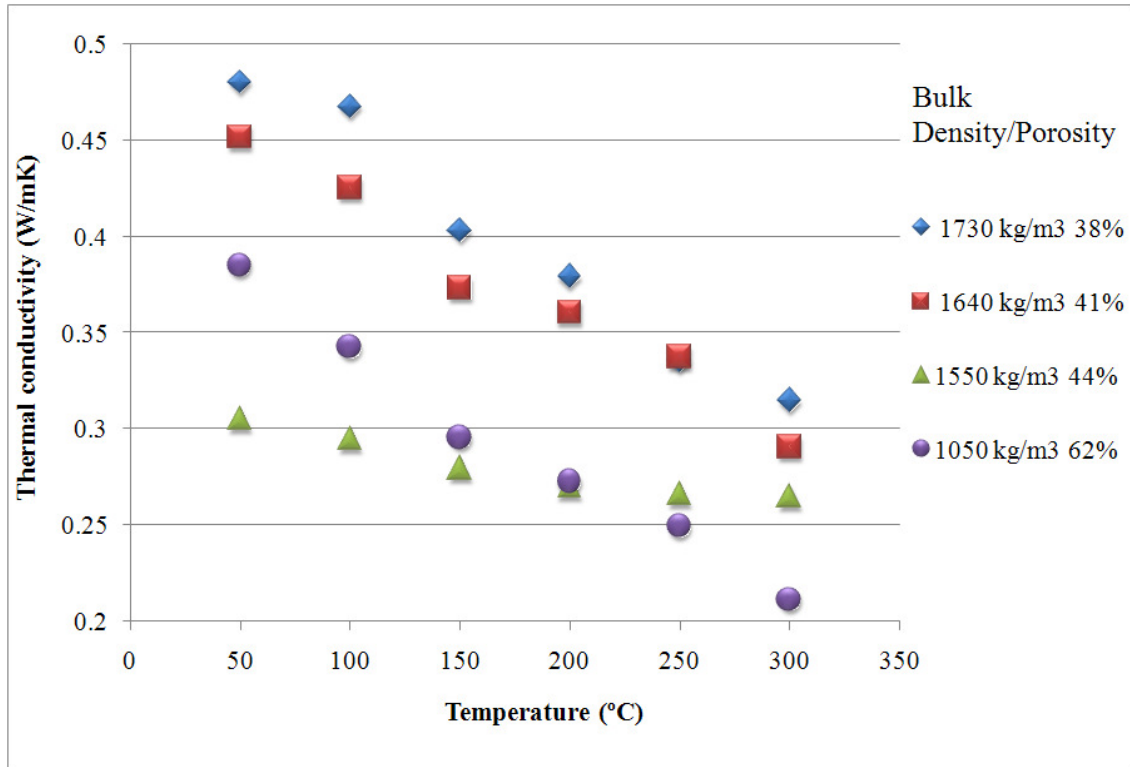


**Figure 71.** Thermal conductivity of ferric sulphate as a function of temperature and bulk density/porosity. (59-60)

The thermal conductivity values for ferric sulphate are slightly lower than those for copper sulphate, ranging from 0.5 W/mK at lower temperatures to 0.2 at 300 °C. The density of the ferric sulphate samples is, however, lower than the density of the copper sulphate samples. At higher temperatures the values of all the samples are very close to those for copper sulphate. In addition, the values for ferric sulphate show a decreasing temperature trend, which is more pronounced in dense samples. The sample with 44% porosity varies from the trend, due to particularly high scatter in the high temperature measurement results. The scatter may be caused by defects in the measurement sensor, such as foil oxidation, or by changes in the sample structure due to crystal water vaporisation.

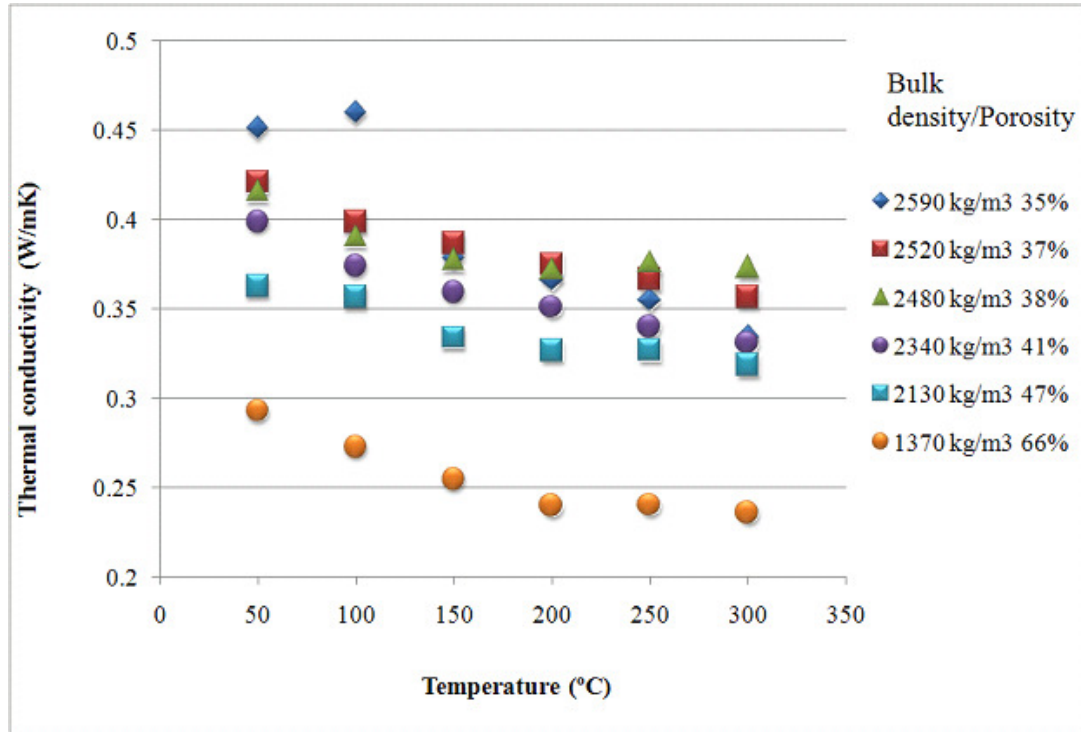


**Figure 72.** Thermal conductivity of flue dust as a function of temperature and bulk density/porosity. **Sample I** (59-60)

The thermal conductivity values of the flue dust range from 0.45 to 0.25 W/mK and have much less variation than the values of the pure metallic sulphates. This can be explained by the fact that there are no large differences in the sample densities, except for one sample. A slight decreasing temperature trend can be detected and the values at 300 °C are very close to those of the copper and ferric sulphate samples.

The thermal conductivity measurement values for the dust build-up of the Harjavalta radiation section are presented in Figure 73, while those for the convection section build-up are presented in Figure 74. Contrary to the results with the compressed dust pellets, the thermal conductivity dependence of the dust deposits follows an increasing temperature trend. This type of behaviour is typical of ceramics containing silica or glass components.

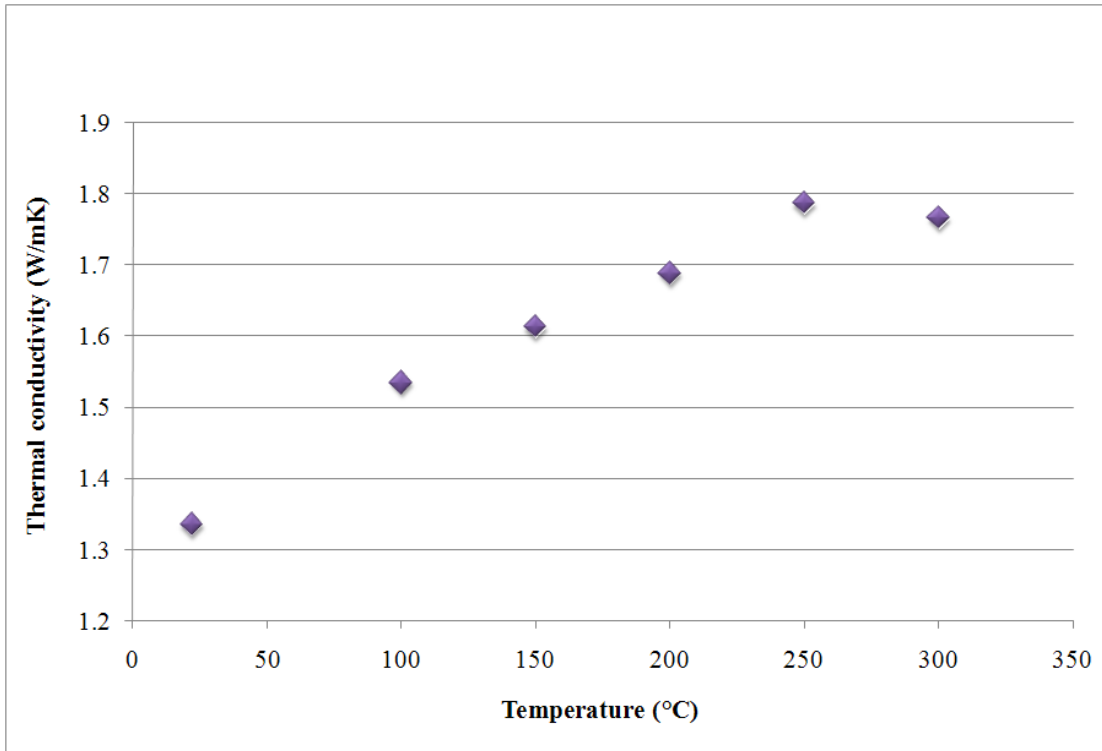


*Figure 73. Thermal conductivity of the radiation section dust build-up from the Harjavalta boiler. Sample IV*

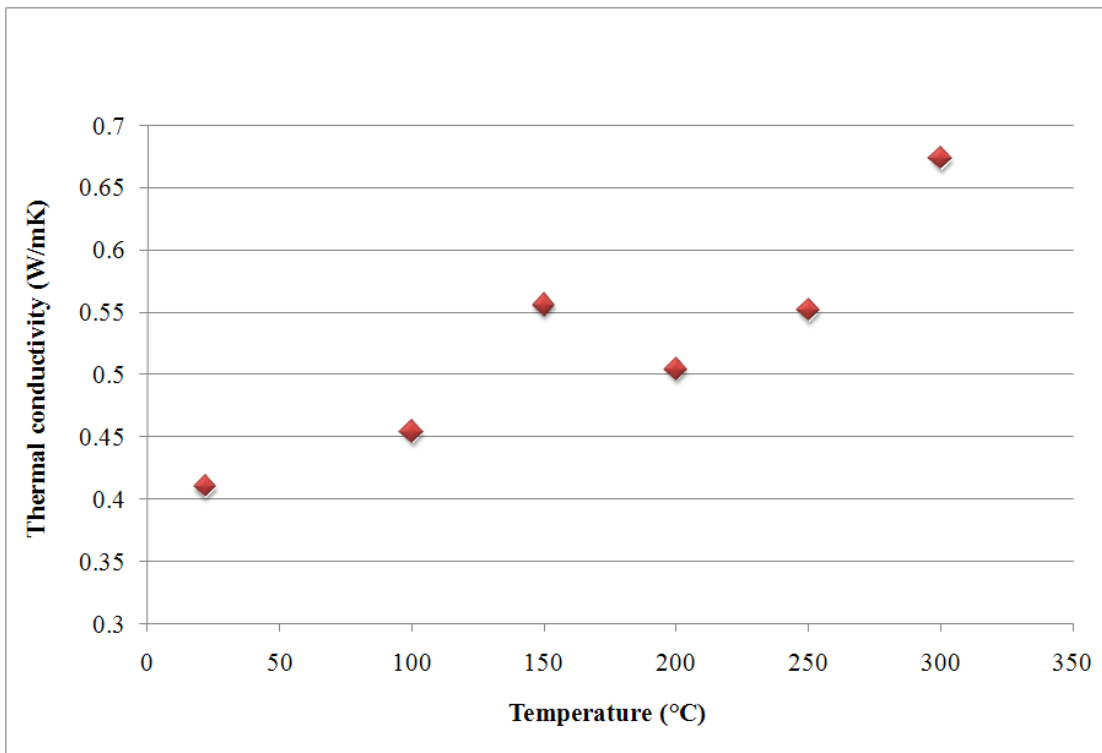


*Figure 74. Thermal conductivity of the convection section dust build-up from the Harjavalta boiler. Sample V*



### 4.3 Specific heat

The results of the Differential Scanning Calorimeter (DSC) specific heat capacity measurements for the two pure sulphate standards and the two flue dust materials are presented in Figure 75. The specific heat results are very similar for all the measured materials and show an increasing temperature dependence.

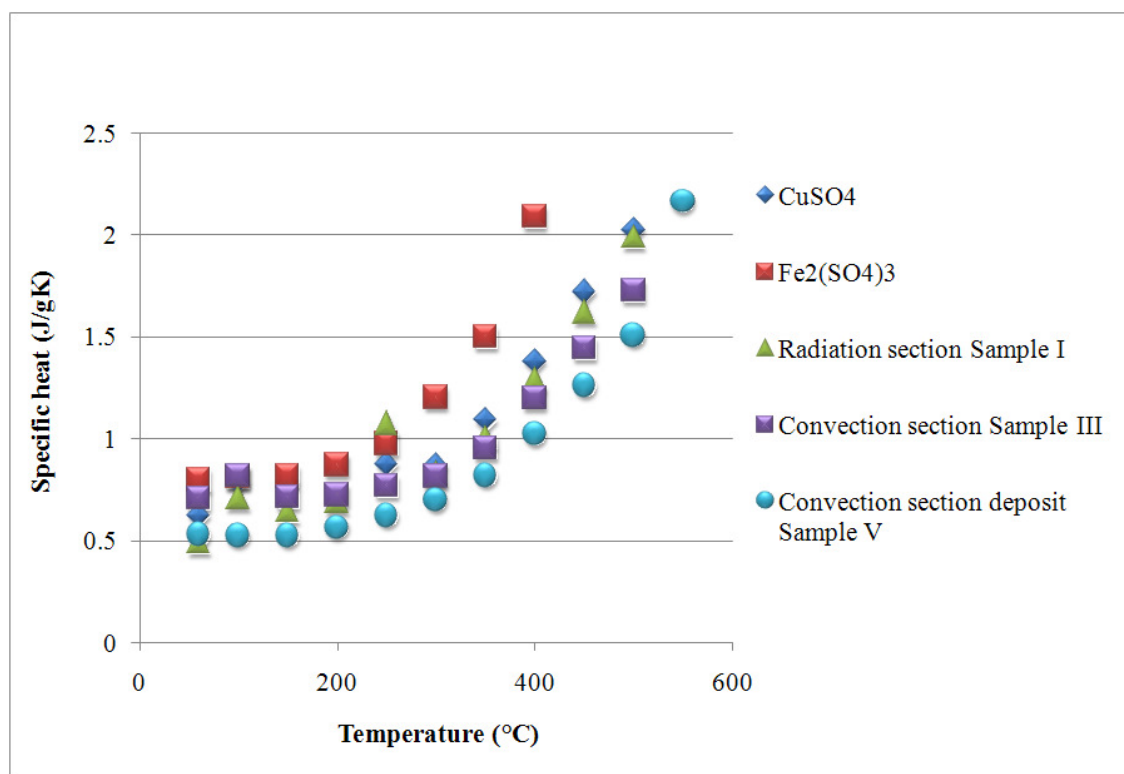


**Figure 75.** The specific heat of  $\text{CuSO}_4$ ,  $\text{Fe}_2(\text{SO}_4)_3$ , and two flue dust samples measured using the DSC method.

The irregularities in the curve of Figure 75 shape are caused by the volatilisation reactions of crystal water and arsenic compounds and the accelerating increase at high temperatures is caused by the decomposition of the sulphates. The room temperature results measured with the Hot Disk device specific heat capacity cell presented in Figure 76 show the decreasing density dependence of the specific heat.

## RESULTS

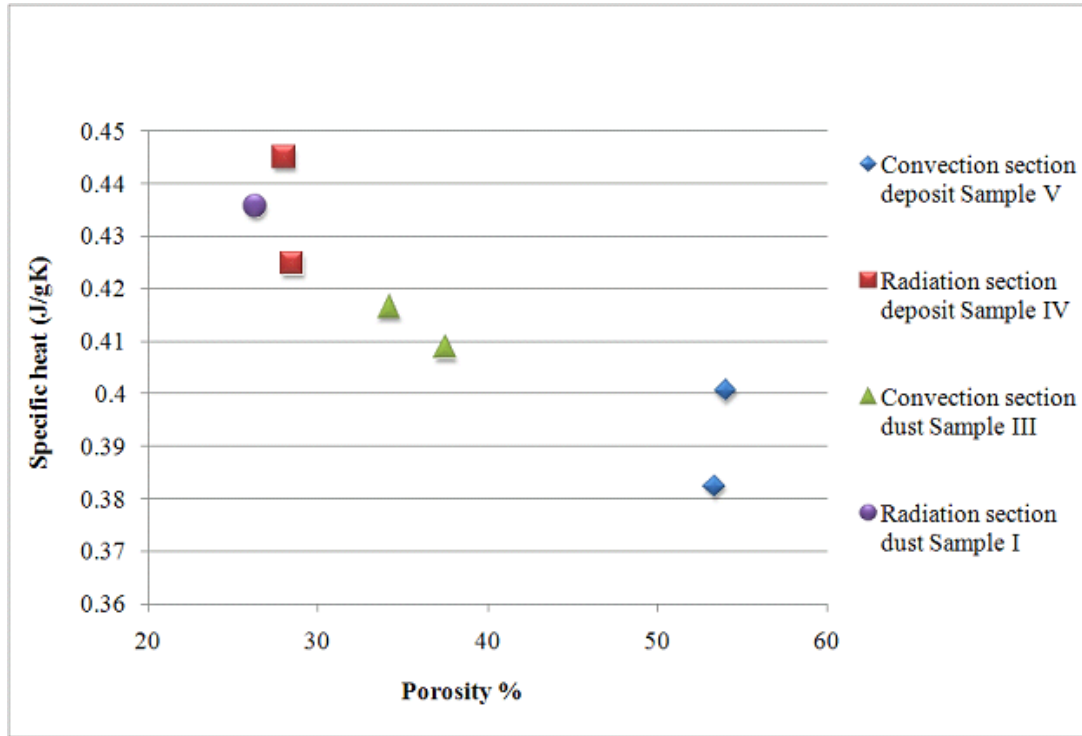


*Figure 76. Room temperature specific heat as a function of the porosity of the sample.*

The results agree well with the values of the results obtained with the DSC method. There is a general trend of decreasing specific heat capacity as a function of increasing porosity. Materials with low density and thus high porosity have lower ability to retain heat. For dense materials, more energy is needed to raise their temperature.

#### 4.4. Conclusions of the results

The thermal conductivity values calculated on the basis of the thermal diffusivity and specific heat capacity measurements are presented in Figure 77. For the sake of comparison, the measurements with the Hot Disk device are also presented in the same figure.

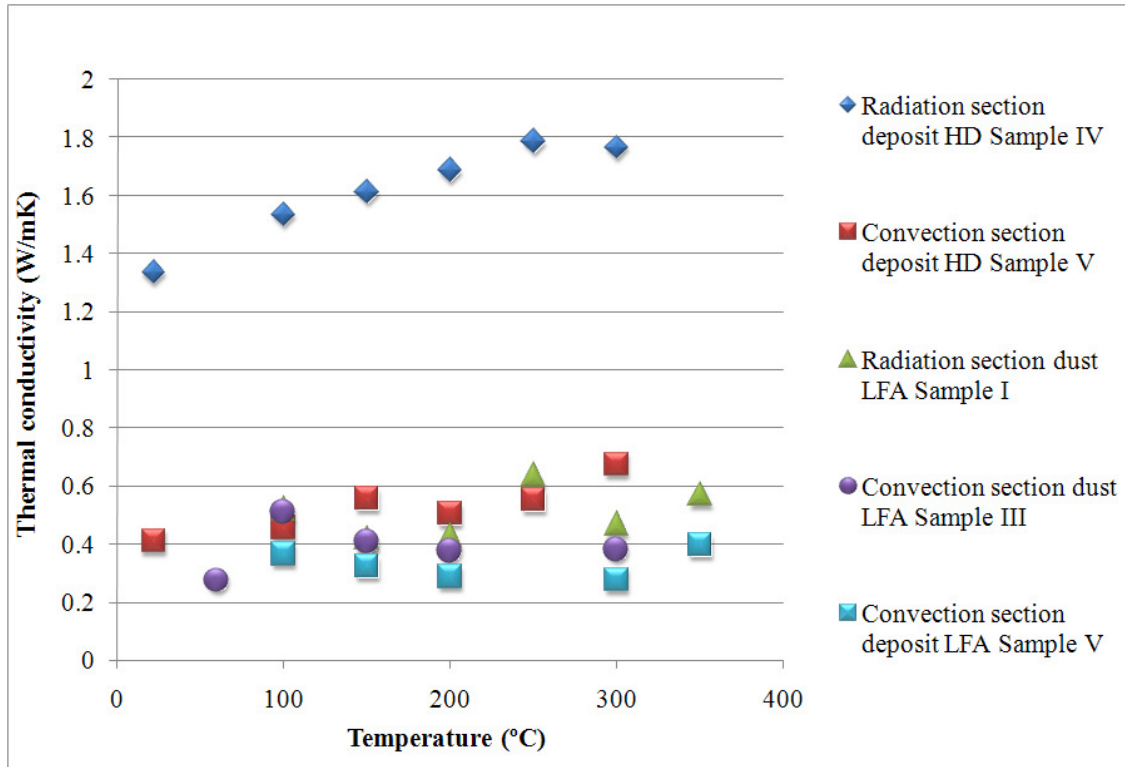


**Figure 77.** Thermal conductivities measured with Hot Disk and calculated from LFA thermal diffusivity and specific heat results.

All the results, except those for the hard, dense radiation section deposit, lie between 0.2 and 0.7 W/mK, indicating that neither material chemical composition nor the measurement technique severely affects the values. Both measurement techniques give fairly similar results for the convection section deposit. The results given by Hot Disk are slightly higher and may result from variations in the sample structure, as making both measurements from the same exact sample was not possible. The results also show that the values measured from the mechanically pressed flue dusts do not vary much from the values of the deposited brittle material from the boiler.

The repeatability of the both measurement devices, LFA and TPS was fairly good. According to the device suppliers the accuracy of the both methods is within 5 % and the standard deviation of the measurements was found to stay within that margin. The thermal conductivity results calculated from the LFA and DSC results obviously contain a larger margin of error due to the add-up effect of various measurements. The error margins in the DSC measurements and in the density measurement cause a combined error margin of 10-15% in the calculated thermal conductivity results.

## RESULTS

---

The microstructure of the material seems to be a significant factor affecting the results. The hard dense deposit from the radiation section showed significantly higher thermal conductivity results in comparison to all other materials. The values of the dense deposit were between 1.3 and 1.8 W/mK. Even though higher than was the case with the other materials, this deposit must also nevertheless be considered as a thermal insulator.

In addition to the effect of condensed microstructure, a larger particle size may increase the thermal conductivity values of the dense deposit in comparison to other materials. When the radiation section dust with a larger average particle size is compared to the convection section dust that has a smaller average particle size, no large difference can, however, be seen.

Temperature seemed to increase the thermal conductivity values of most dust samples slightly. The effect was most pronounced in the dense radiation section deposit.

## 5. DISCUSSION

### 5.1 Flue dust deposition mechanism

The flue dust deposit formation takes place in several stages, as has been documented for coal-fired boilers. In the initial stage a layer of fine particles forms on the surface. The initial deposition takes place by the thermophoresis of fine particles or by the condensation of vapours (28-29). Low-melting-point eutectic components of potassium can act as sticky cohesive particles attaching to the walls. The fine particles landing on the surface quickly go through to complete sulphation and after some maturation time they form a consolidated sulphate layer. Figure 78 shows fine particles from the gas stream that are likely to attach to the initial layer on the tube wall, and an initial layer structure after a longer period of time.

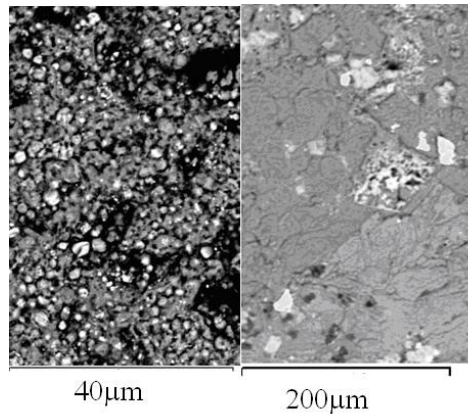


*Figure 78. Schematic initial layer deposition. Samples II and IV.*

Once the primary layer has deposited on the tube wall, it is easier for larger particles to attach. The larger particles often attach to the primary layer through sulphate bridges between the particles. An exothermic sulphation reaction increases the temperature of the particles, causing them to weld together. In addition, the increase in the particle molecular volume resulting from sulphation increases the contacts between particles. Proof of a sulphation-induced agglomeration process has previously been reported by Anthony et al. (46-50), Walsh et al. (42), Hurley et al. (61), and Ranki-Kilpinen et al. (62-64). The vapours of low-melting-point impurities are likely to condense on the surface of the particles and into the spaces between the particles.

The initial layer works as a very thermally insulating layer, enabling the temperature in the deposit layer further from the tube wall to increase. The increase in temperature can cause softening of the material, grain growth, or even melting, while the temperature gradients in the layer cause the migration of elements. Impurity elements may dissolve into the matrix or segregate into self-standing particles. Some elements form liquid phases and some diffuse away from the deposit. The transformations that take place in the particles during a long-lasting exposure at high temperature are shown schematically in Figure 79.

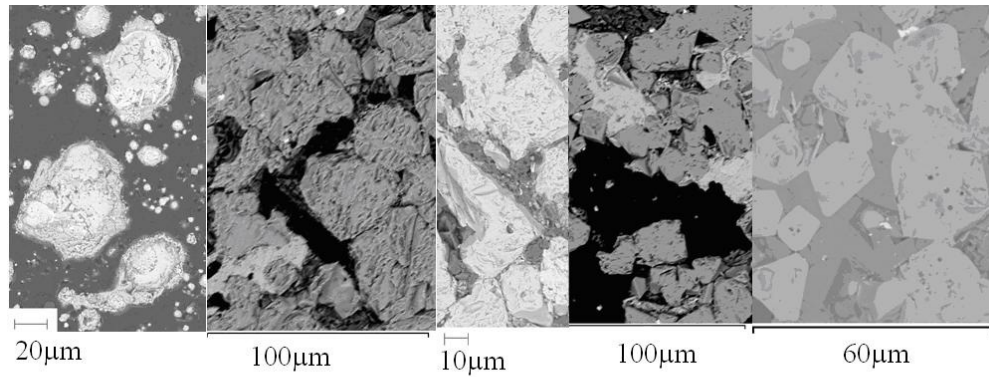


**Figure 79.** Schematic presentation of the particle microstructure transformation.

As the deposit matures, the layers compress and sulphate thoroughly. Softened or molten components re-crystallise and grain growth takes place. New particles are attached to the surface of the layer. These new layers are formed at much higher temperatures and thus form very different kinds of layers. At higher temperatures sulphation may not proceed as far as in the initial layers.

Figure 80 shows a layered structure formed in a radiation section of a heat recovery boiler.

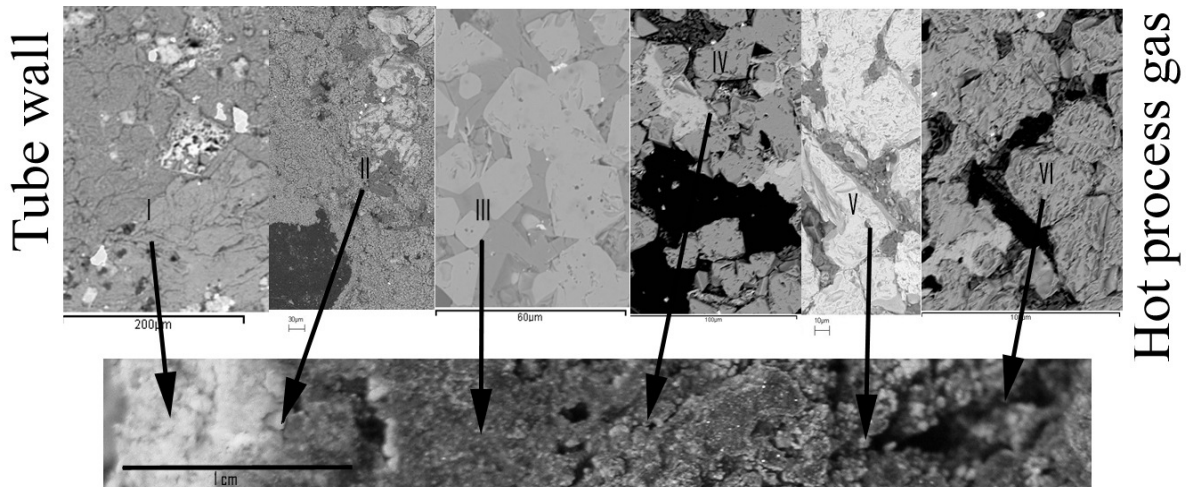


**Figure 80.** Schematic presentation of flue dust deposit layers in heat recovery boiler radiation section.

The layers closest to the tube wall (I & II) consist of consolidated fully sulphated material that is formed of fine particles. Layer III consists of hard dense material that has softened or melted. In this layer segregation and re-crystallisation have also taken place and the migration of condensed elements such as arsenic has formed larger separate crystals. In Layer IV the particles are sintered together, forming solid bridges between them. In the interstitial spaces between the particles, sulphate phases can be detected. Layer V consists of particles slightly sintered together, combined by sulphate phases between the particles. In Layer VI, on the hot face of the accretion and closest to the gas phase, particles are bound together by sulphate



phases, but have not been sintered together. Similar layered structures were also suggested by Wall et al. (28-30) and Abd-Eldhady et al. (41).

In the convection section the temperatures are lower and completely molten and recrystallised phases are very rare. Typical convection section layers are shown in Figure 81.

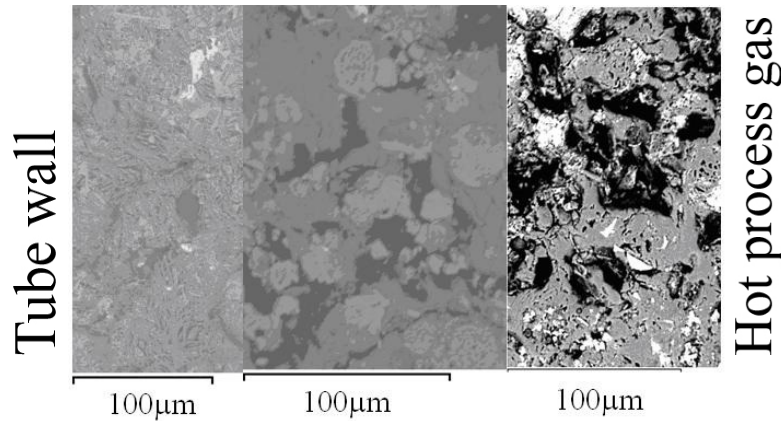


**Figure 81.** Schematic presentation of convection section flue dust deposit layers.

The left-hand layer consists of fully sulphated material, formed of fine particles. The middle layer consists of particles bound together by sulphate phase and the layer on the right consists of particles sintered together and re-crystallised as a result of exposure to hot process gas.

The boiler process gas diffuses very slowly into the porous accretion layer to form a stagnant gas layer within the structure. The composition of the gas layer may differ greatly from the composition of the process gas that is flowing on the surface of the accretion layer. Sulphide particles in the structure are likely to react with the gas, consuming the oxygen in the gas and forming sulphates. Locally, even a reducing atmosphere may form within the layer, allowing new reactions to take place. The local micro-atmosphere may enable metal sulphates to be reduced into secondary sulphides and even metallic components. Within the accretion layer, components may be formed that would not be thermodynamically stable in the process gas atmosphere.

## 5.2 Flue dust deposit thermal properties

According to the results, all the dust components and materials are effective insulators, with thermal conductivity values of less than 2 W/mK and thermal diffusivity values of less than 0.005 cm<sup>2</sup>/s (57-58). There seems to be no significant difference between the thermal conductivities of the different flue dust components. The dense, hard deposit from the Harjavalta radiation section has higher conductivity values of 1.3-1.8 W/mK, while all the other samples show values of less than 1 W/mK. The radiation section deposit has been subjected to fairly high temperatures for a significant time and has undergone sintering and fusing processes, resulting in a dense microstructure and higher thermal conductivity values.

### 5.2.1 The effect of porosity

To study the effect of porosity on the thermal conductivity of the samples, the bulk density and porosity values of the samples were determined.

The bulk density of the materials was calculated with:

$$\rho_B = \frac{m}{V} \quad (24)$$

and the porosity with:

$$\Pi = 1 - \frac{\rho_B}{\rho_P} \quad (25)$$

where  $\rho_P$  is the particle density, determined by helium pycnometer measurements. The particle densities of the materials lay between 3000 and 4500 kg/m<sup>3</sup>.

The different materials have varying grain sizes and densities and a direct comparison of their thermal properties is difficult. The results of this work indicate that the porosity of the sample is a more important factor affecting the thermal transfer properties of the dust layer than the chemical composition of the fouling layer. In all the materials, increasing the bulk density increases the thermal diffusivity and conductivity, as shown in Figure 82.

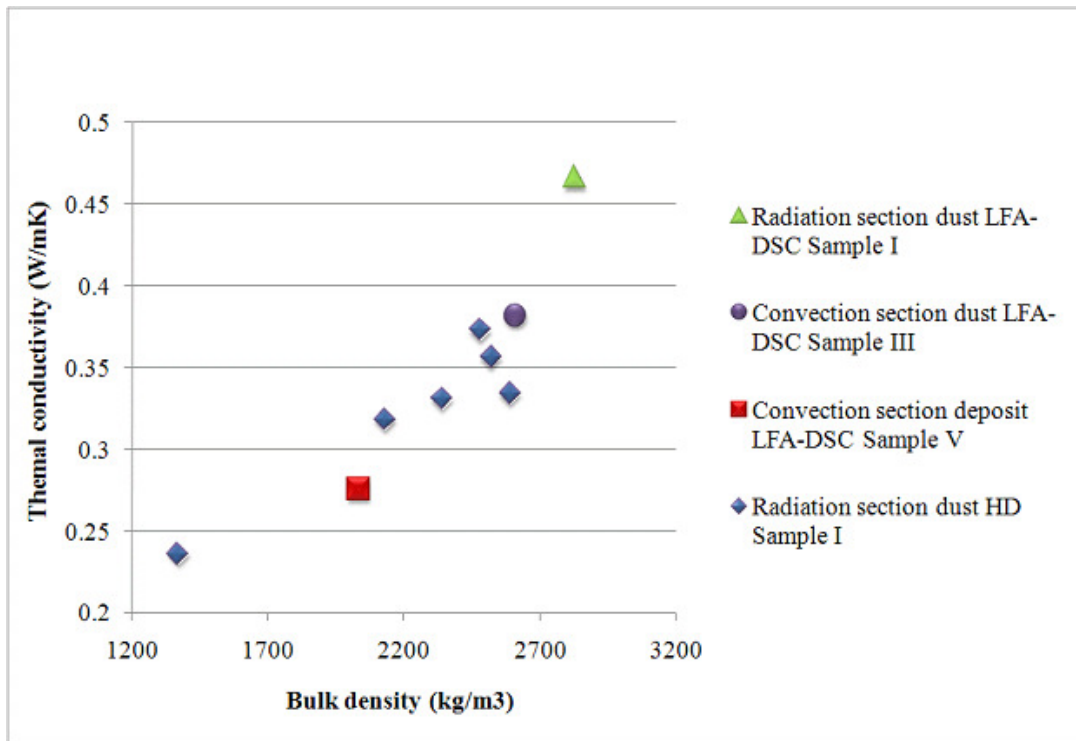


**Figure 82.** Thermal conductivity as a function of sample bulk density for various materials at 300 °C.



Inversely, as shown in Figure 83, increasing porosity clearly reduces thermal conductivity values.

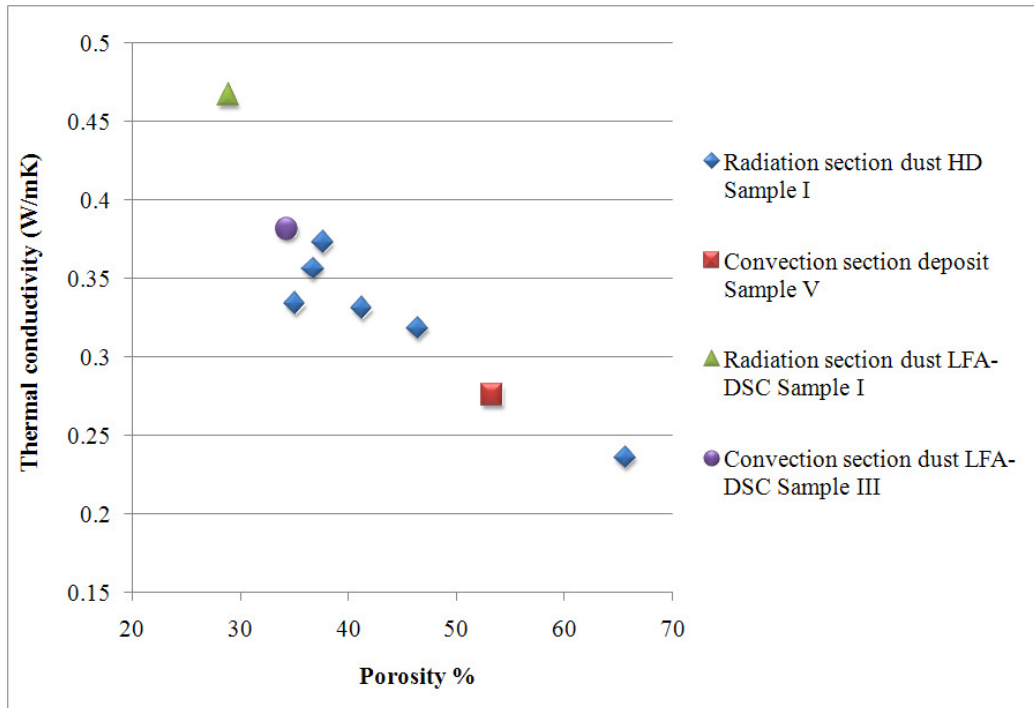


**Figure 83.** Thermal conductivity as a function of sample porosity for various materials at 300 °C.

Rezaei et al. (27) used a modified version of Rayleigh's model (65) proposed by Russel, to successfully describe the thermal conductivity of coal ash deposits. Russel's model is described by Equation 26:

$$\frac{\lambda_{2ph}}{\lambda} = \frac{k_p \psi^{2/3} + (1 - \psi^{2/3})}{k_p (\psi^{2/3} - \psi) + (1 - \psi^{2/3} + \psi)} \quad (26)$$

Where  $\lambda_{2ph}$ =conductivity of packed bed,  $k_p = \lambda_p / \lambda$ ,  $\lambda_p$ =conductivity of air,  $\lambda$ =conductivity of the dense material, and  $\psi$  = bed porosity.

The same model was applied to the experimental values shown in Figure 83. When the results of Figure 83 are extrapolated to zero porosity, an approximate thermal conductivity value of 0.6 W/mK for the dense phase is achieved. Figure 84 shows the application of Russel's (modified Rayleigh's) model to the data in Figure 83. The applied thermal conductivity value for air was 0.04305 W/mK (66).

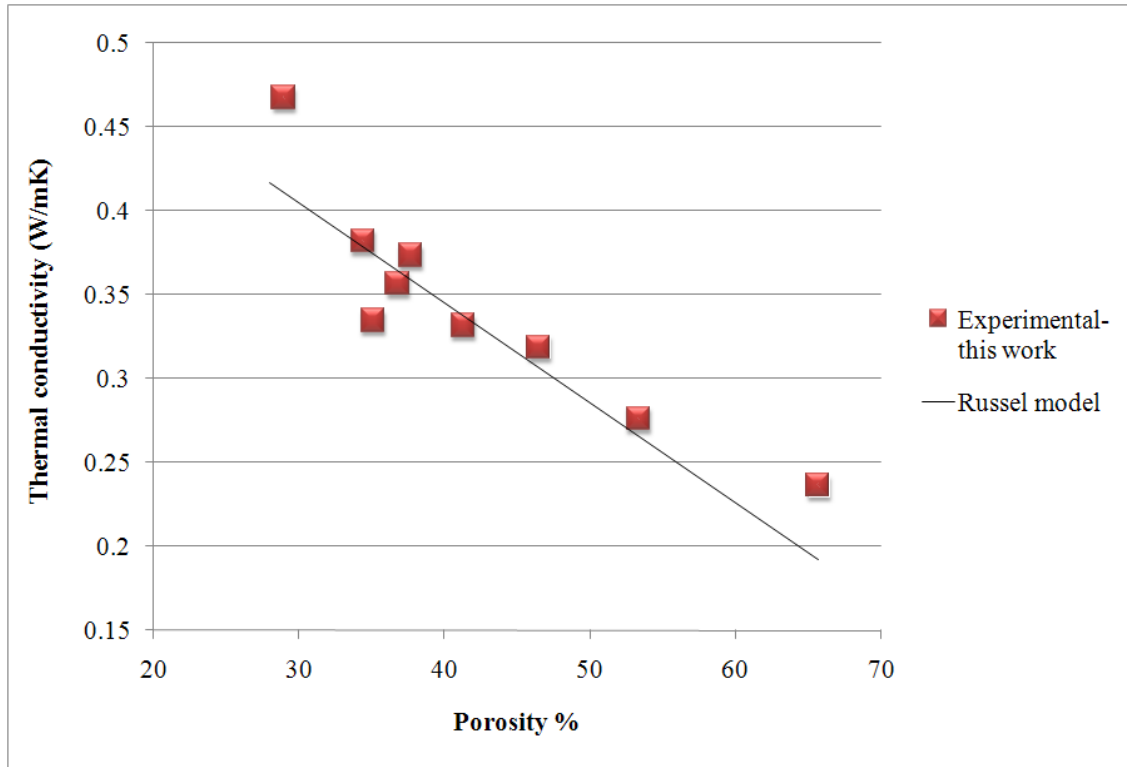


*Figure 84. Comparison of Russel's model and the experimental data.*

Russel's model gives a fairly good fit to the experimental values, although the scatter in the experimental data is quite significant. It is, however, evident that the values for the sintered radiation section deposit would fit this data very poorly. The bulk density and the porosity values of the sintered material do not differ very greatly from the other materials, but the thermal conductivity values are much higher. The most likely cause of this is that microstructural changes have taken place in the deposit as a result of sintering recrystallisation and grain growth, allowing better contact between the particles and thus better conductivity within the material.

## 5.2.2 The effect of temperature

Increasing the temperature reduces the thermal diffusivity values of all the materials fairly rapidly at low temperatures. At temperatures higher than 300 °C the decrease is less dramatic. The initial decrease seems to follow Eucken's law of decreasing thermal conductivity with increasing temperature for crystalline materials (21). It is believed to be caused by increasing phonon-phonon collisions in the material that prevent heat flow (19). In addition, the pores in the material act as an effective cause of phonon scattering. At higher temperatures radiation across the pores may result in the enhancement of thermal energy transportation within the materials. This may be the cause of the slowing-down effect of the thermal diffusivity value decreases at higher temperatures in this work. The thermal diffusivity values are fairly similar to the values reported by Mills et al. (35) for coal ash deposits, as shown in Figure 85. This indicates that chemical composition may not significantly affect the values of thermal diffusivity in particulate deposits. Additionally, the specific heat capacity results are close to

the values reported by Mills et al. (35) and HSC Chemistry (67), further supporting this theory. The comparison of the specific heat capacities is shown in Figure 86.

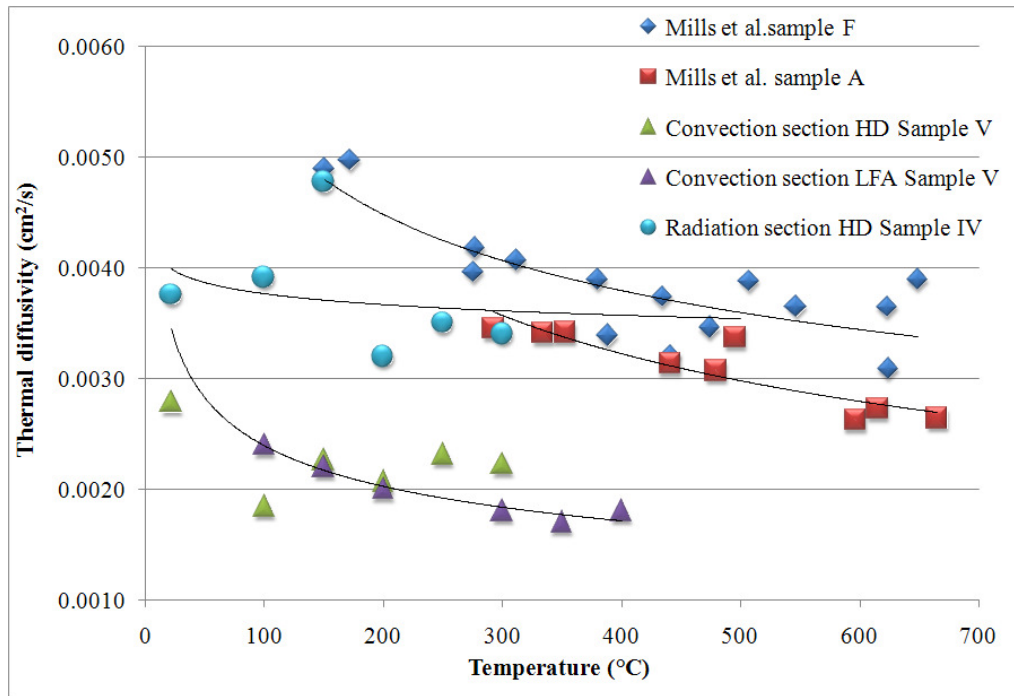


**Figure 85.** Comparison of the thermal diffusivity results with the results of Mills et al. (35) for coal gasifier slags.

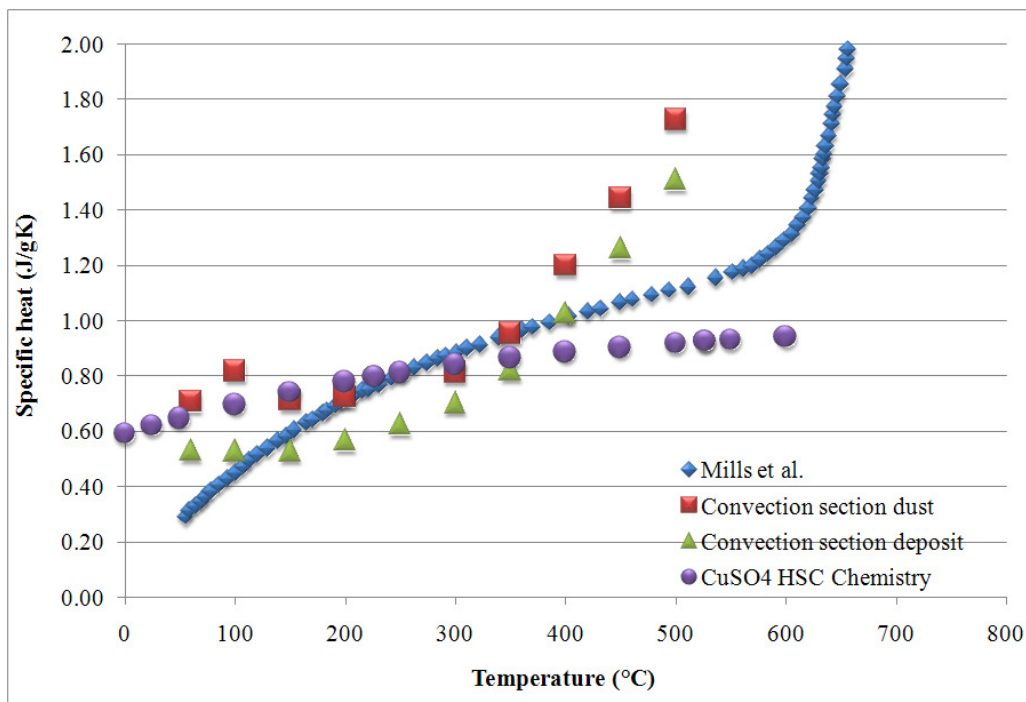


**Figure 86.** Comparison of the specific heat results with the data of Mills et al. (35) for coal gasifier slags and HSC Chemistry database values for  $\text{CuSO}_4$  (67).

## DISCUSSION

The thermal conductivity values of the compressed dust and sulphate pellets show a decreasing temperature dependence (Figures 70-72), which follows Eucken's law for crystalline materials. The dust deposit samples from the boiler, however, have an increasing temperature dependence that resembles more closely the behavior of glass-like materials. It may be that during the considerable time the deposits mature in the boiler, sintering and fusing result in a more glass-like fused structure. The thermal conductivity results for the dust deposits are fairly similar to the results from the coal combustion ash and slag measurements of Rezaei et al. (27) and Mills et al. (35), indicating again that the chemical composition of the samples may not be the determining factor of thermal conductivity. The comparison is shown in Figure 87.

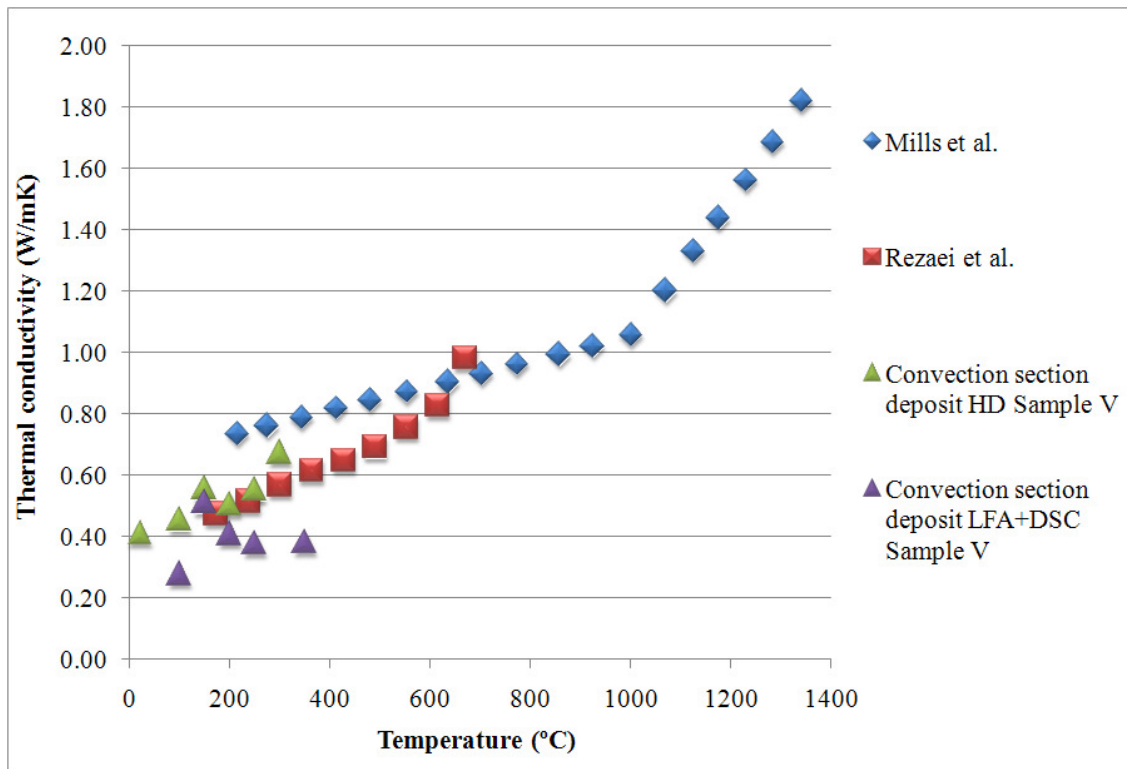


**Figure 87.** Comparison of the thermal conductivity data with the results of Mills et al. (35) for coal gasifier slags and of Rezaei (26) et al. for synthetic coal ashes.

Figure 88 shows suggested changes in the deposit structure and thermal conductivity values and the temperature profile of the deposit as a function of the distance from the wall.

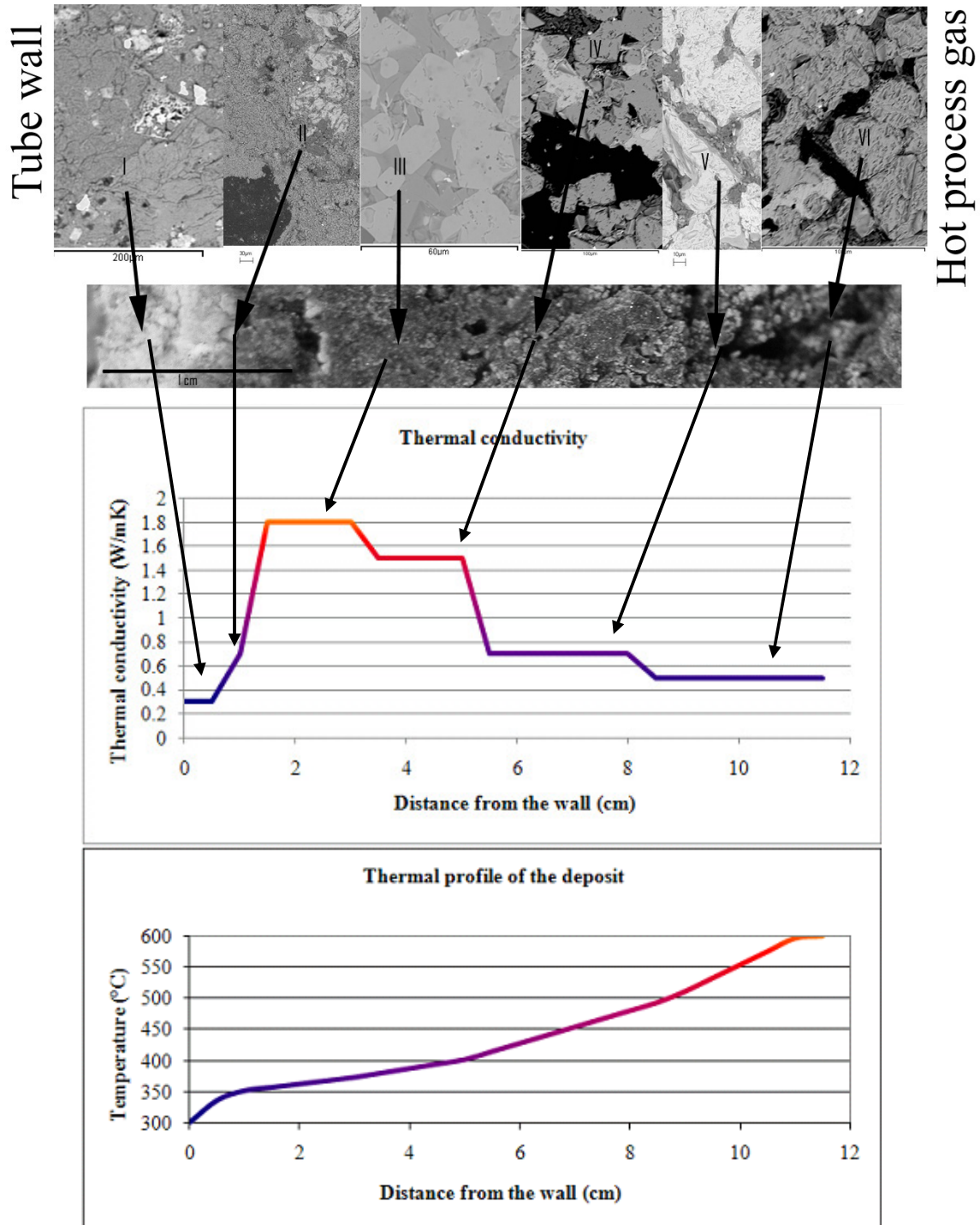


**Figure 88.** Schematic microstructure, thermal conductivity and temperature profiles of a radiation section flue dust deposit.

The thermal conductivity of the initial deposit layer is likely to be fairly low, because of the fine particle size and soft structure. In layers II and III the thermal conductivity is much higher as a result of consolidation and larger particle size. Layers IV-VI then again show lower thermal conductivity values caused by shorter maturation times and fewer sulphate

bridges between the particles as a result of higher temperatures. The suggested structure is likely to prevail in the high-temperature sections of the boiler, whereas in the low-temperature sections only Layers I, V, and VI are likely to be present and the thermal conductivity values are likely to be fairly constant in the range of 0.5 W/mK throughout the deposit.

Figure 89 shows an example of the accretion influence on the heat transfer efficiency of a typical heat recovery boiler convection section. The results are presented as a function of accretion thickness, for varying thermal conductivity values. The results are based on Kruskopf's (68) model for calculating the heat transfer in a 60 bar boiler with a gas handling capacity of 45 000 Nm<sup>3</sup>/h. The gas composition used is 40% SO<sub>2</sub>, 2.5% O<sub>2</sub>, 2% H<sub>2</sub>O and balance N<sub>2</sub>. The Excel-based tool divides the convection section into specific areas covering the tube banks, the walls and roof of the tube bank's immediate surroundings. The tool calculates the off-gas output temperature for each area using an iterative method.

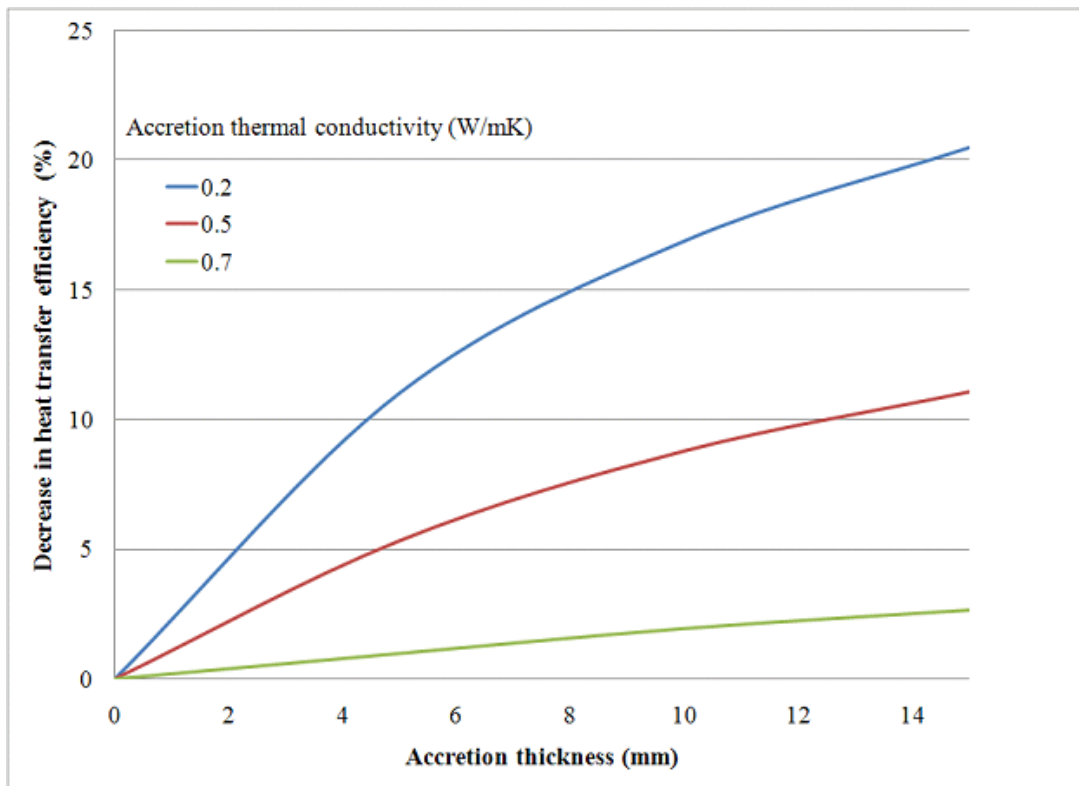


**Figure 89.** The influence of accretion into heat recovery efficiency of a convection section.

The calculations indicate that the heat transfer efficiency may decrease over 40 % if a thick layer of porous dust covers the convection tubes. The typical values near 0.5 reported in this work would reduce the heat transfer efficiency by up to 15 %. This result relates well with results reported for coal combustion furnaces by Wall (28), shown in Figure 28.

## 6. CONCLUSIONS

According to the results of this work, the thermal diffusivities of Copper Flash Smelting flue dust and its components are fairly low, indicating that they are effective thermal insulators. Dust accretion layer on the wall of a heat recovery boiler may dramatically hinder the heat transfer through the boiler wall. The results of the samples in this work are of a similar order of magnitude to the ones earlier reported for coal ash deposits in coal combustors. Despite the differences between the chemical compositions of coal ash deposits and sulphate flue dust deposits, their thermal transport properties seem to be fairly similar; indicating that porosity and the microstructure of the material are more important factors in determining the deposit thermal conductivity than the actual chemical composition is. The influence of the chemical composition on the microstructure of the deposits must be, however, considered, especially in high temperatures and regarding the melting point of the material. The thermal diffusivity of all the examined samples in this work show decreasing temperature dependence and the specific heat capacities an increasing dependence. The thermal conductivity values show slightly increasing values for accretion samples with a high sintering degree and a slightly decreasing trend for the samples compressed of powders. The results may be used in the computer modeling of the process and in process optimisation, as well as in boiler dimensioning.

The flue dust is likely to deposit on the boiler walls as layers of various densities and thermal properties. The initial layers deposit through thermophoresis or condensation and, after the initial deposition, larger particles are able to stick to the surface through the formation of sulphate bridges. Layers subject to adequate time and temperature levels undergo sintering and condensation, resulting in higher densities and larger thermal conductivities. Species migration and segregation may also take place in these layers. The thermal conductivity seems to have a fairly clear decreasing dependence as a function of porosity or the decrease in bulk density of the particulate samples. For the more sintered samples, the microstructural changes cause a significant increase in their thermal conductivity, despite a minor change in the porosity values. The increasing contacts between the particles affect the conductivity of the material without significantly changing the porosity.

The heat transfer efficiency of a heat recovery boiler is proportional to its fouling amount. Highly porous accretions on the tube surfaces have a significant effect on the heat transfer. Deposits with long residence times in the boiler undergo sintering and at high enough temperatures even fusing or melting. Thermal conductivities of fused deposits are higher than the porous ones, but also harder to remove and offer an easy attachment point for further deposit accumulation. For optimal heat transfer efficiency of a boiler, the heat transfer surfaces should be kept as clean as possible.

**REFERENCES**

1. Vartiainen, A. Course material - COM 2007 Short Course Pyrometallurgy of Copper with a Focus on Converting. August 25-26, 2007. Toronto, Canada.
2. Yang, Y. Computer Simulation of Gas Flow and Heat Transfer in Waste-Heat Boilers of the Outokumpu Copper Flash Smelting Process. Acta Polytechnica Scandinavica Chemical Technology Series 242. Doctoral thesis Helsinki University of Technology 1996. p. 135.
3. Samuelsson, C. and Björkman, B. Dust Forming Mechanisms in the Gas Cleaning System after the Copper Converting Process. Scandinavian Journal of metallurgy Vol 27 (1998) pp. 54-63.
4. Samuelsson, C. Controlled Dust Separation, Theoretical and experimental study of the possibilities of controlled dust separation in copper producing processes. Doctoral Thesis. Luleå University of Technology, Luleå 1999. ISSN: 1402-1544.
5. Swinbourne, D.R., Simak, E., and Yazawa, A. Accretion and Dust Formation in Copper Smelting – Thermodynamic considerations. In: Sulfide Smelting 2002. TMS (The Minerals, Metals and Materials Society), 2002. Seattle, Washington, USA, 2002. pp. 247-259. ISBN 0-87339-525-5.
6. Sjöblom, J., Yliheljo, H. and Jokilaakso A. “Studies on Reactivity of Copper and Nickel Mattes under Suspension Smelting Conditions. ”. In: Diaz, C., Landolt, C. and Utigard, T. (eds.) Smelting, Technology Development, Process Modeling and Fundamentals. Vol. VI, Copper-Cobre International Conference, TMS (The Minerals, Metals and Materials Society), 1999pp. 449-461. ISBN 0-87339-440-2
7. Barin, I., Modigell, M., and Sauert, F. Thermodynamics and Kinetics of Cyclone Smelting of Metal Sulphides. In “Advances in Sulfide Smelting”, Volume 1, Basic Principles. The Metallurgical Society of AIME, Warrendale, 1983. pp. 257-273. ISBN 0-89520-464-9.
8. Sohn, H.Y. and Chaubal, P.C. The Ignition and Combustion of Chalcopyrite Concentrate Particles under Suspension-Smelting Conditions. Metallurgical Transactions B, 1993. Vol. 24B, December 1993. pp. 975-985.
9. Wigley, F. and Williamson, J. Coal Mineral Transformations –Effects on Boiler Ash Behaviour. Report No. COAL R278 DTI/Pub URN 05/659. March 2005. Imperial College, London.
10. Swinbourne, D.R., Simak, E., and Yazawa, A. Accretion and Dust Formation in Copper Smelting – Thermodynamic considerations. In: Sulfide Smelting 2002. TMS (The Minerals, Metals and Materials Society), 2002. Seattle, Washington, USA, 2002. pp. 247-259. ISBN 0-87339-525-5.



11. Markova, Ts., Boyanov, B., Pironkov, S., and Shopov, N. Investigation of dusts from waste-heat boiler and electrostatic precipitators after flash smelting furnace for copper concentrates, *Journal of Mining and Metallurgy*. Vol. 36 (3-4)B 2000. pp. 195-208.
12. Kurosawa T, Yagishi, T, Togo, K, and Kato, T. On the Several Problems of Dust in the Copper Smelting. *Transactions of National Research Institute for Metals*. Vol 15 (3), 1973. pp. 34-44.
13. Kim, J.Y., Lajoie, S., and Godbehere, P. Characterization of copper smelter dusts and its effect on metal recovery. In Rao et al. eds. *Waste Processing and Recycling in Mineral and Metallurgical Industries II Vancouver, British Columbia, Canada: CIM, 1995*. pp. 221-234.
14. Whyte, J.R., Geiger, G.H., and Seshan, K. The Nature and Resource of Copper Smelter Particulate Emissions. *Metallurgical Transactions B*. 1984 Vol. 15B. pp. 617-622.
15. Evans, J.P., Mackey, P.J., and Scott, J.D. Impact of Gas Cooling Techniques on Smelter Dust Segregation. In: Smith T.J.A., Newman C.J. ed. *Smelter Process Gas Handling and Treatment*. Warrendale, PA. TMS 1991. pp. 189-214.
16. Lastra-Quintero, R., Rowlands, N., Rao, S.R., and Finch, J.A. Characterization and Separation of Copper Smelter Dust Residue. *Canadian Metallurgical Quarterly*. Vol. 26 (2), 1987. pp. 85-90.
17. Kyllö, A.K., Richards, G.G., and Verhelst, D. Analysis of Copper Smelter Dusts. In: Ramachandran V. and Nesbitt C.C., eds. *Second International Symposium on Extraction and Processing for the Treatment and Minimization of Wastes*, Warrendale, PA. TMS 1996. pp. 823-832.
18. Morales, A., Cruells, M., Roca, A., and Bergo, R. Characterization of Flue Dusts from a Copper Smelter Furnace, Copper recovery and Arsenic Stabilization. *The John E. Dutrizac International Symposium on Copper Hydrometallurgy, Cu 2007 Volume IV (2)* eds. Riveros P.A. et al. Toronto 2007. pp. 177-189.
19. Kingery, W.D., Bowen, H.K., and Uhlmann, D.R. *Introduction to Ceramics*, Chapter 12. Thermal properties. John Wiley & Sons, New York (1967) pp. 583-645.
20. Shapiro, M., Dudko, V., Royzen, V., Krichevets, Y., Lekhtmakher, S., Grozubinsky, V., Shapira, M., and Brill, M. Characterization of Powder Beds by Thermal Conductivity: Effect of Gas Pressure on the Thermal Resistance of Particle Contact Points. *Particles and Particle Systems Characterization*. Vol 21 (2004) pp. 268-275.
21. Litovsky, E. and Shapiro, M. Gas Pressure and Temperature Dependencies of Thermal Conductivity of Porous Ceramic Materials: Part 1, Refractories and Ceramics with Porosity below 30%. *Journal of American Ceramic Society*. 75 (12) 1992 pp. 3425-39.
22. Litovsky, E. Shapiro, M., and Shavit, A. Gas Pressure and Temperature Dependencies of Thermal Conductivity of Porous Ceramic Materials: Part 2, Refractories and Ceramics with Porosity Exceeding 30%. *Journal of American Ceramic Society*. 79 (5) 1996 pp. 1366-76.

## REFERENCES

---

23. Tsotsas, E. and Martin, H. Thermal Conductivity of Packed Beds. *Chemical Engineering Processing*. Vol. 22 (1987) pp. 19-37.
24. Maxwell, J.A. *Treatise on Electricity and Magnetism*, Clarendon Press, London, 2<sup>nd</sup> ed. 1959.
25. Bauer, T.H. A general analytical approach toward the thermal conductivity of porous media. *International Journal of Heat and Mass Transfer*. Vol. 32 (1993) no.17 pp. 4181-191.
26. Feng, Y., Yu, B., Zou, M., and Zhang, D. A generalised model for the effective thermal conductivity of porous media based on self-similarity. *Journal of Physics D: Applied Physics*. Vol 37 (2004) pp. 330-3040.
27. Rezaei, H.R., Gupta, R.P., Bryant, G.W., Hart, J.T., Liu, G.S., Bailey, C.W., Wall, T.F., Miyamae, S., Makino, K., and Endo, Y. Thermal conductivity of coal ash and slags and models used. *Fuel*. Volume 79, Issue 13 (2000). pp. 1697-1710.
28. Wall, T.F. The character of ash deposits and the thermal performance of furnaces. *Fuel Process Technology*. Vol. 44 (1995), pp. 143-153.
29. Wall, T.F., Bhattacharya, S.P., Zhang, D.K., Gupta, R.P., and He, X. The Properties and Thermal Effects of Ash Deposits in Coal-Fired Furnaces. *Progress in Energy Combustion Science* Vol. 19 (1993) pp. 487-504.
30. Wall, T.F., Lowe, A., Wibberley, L.J., and Stewart, I.McC. Mineral Matter in Coal and the Thermal Performance of Large Boilers. *Progress in Energy Combustion Science* Vol. 5 (1979) pp. 1-29.
31. Anderson, D.W., Viskanta, R., and Incropera, F.P. Effective Thermal Conductivity of Coal Ash Deposits at Moderate to High Temperatures. *Journal of Engineering for Gas Turbines and Power* Vol. 109 (1987) pp. 215-221.
32. Boow, J. and Goard, P. Fireside deposits and their effect on heat transfer in a pulverized-fuel-fired boiler: Part III. The influence of the physical characteristics of the deposit on its radiant emittance and effective thermal conductance. *Journal of the Institute of Fuel*. Nov. 1969. pp. 412-418.
33. Abryutin, A. and Karasina, E. Thermal Conductivity and Thermal Resistance of Ash Deposits in Boiler Furnaces. *Thermal Engineering*. Vol. 17 (12) 1970. pp. 36-39.
34. Karasina, E., Abryutin, A., and Efimenko, A. Determination of Heat Transfer Resistance of Slag and Ash Deposits on Panel Walls with a Watercooled Heat Flow Meter. *Thermal Engineering*. Vol. 26 (1) 1979. pp. 27-30.
35. Mills, K. and Rhine, J. The Measurement and Estimation of the Physical Properties of Slags Formed During Coal Gasification. 2. Properties Relevant to Heat Transfer. *Fuel*. Vol. 68 July 1989. pp. 904-910.

36. Poulhier, C., Smit, D.S., and Absi, J. Thermal conductivity of pressed powder compacts: tin oxide and alumina. *Journal of the European Ceramic Society* Vol 27 (2007) pp. 475-478.
37. Hashemi, R. and Brown, R. Heat Exchanger Fouling Causes Problems In Gas And Liquid Systems. *American Filtration Society Seminar, Chicago, Illinois, May 11, 1992.*
38. Chang, Y., Ranade, M., and Gentry, J. Thermophoretic Deposition in Flow along an Annular Cross-Section: Experiment and Simulation. *Journal of Aerosol Science.* Vol 26 (3) 1995 pp. 407-428.
39. Chein, R. Thermophoretic effects on nano-particle deposition in channel flow. *Heat and Mass Transfer.* Vol. 42 (2005) pp. 71-79.
40. Mwaba, M., Golriz, M., and Gu, J. A semi-empirical correlation for crystallization fouling on heat exchange surfaces. *Applied Thermal Engineering.* Vol. 206 (2006) pp. 440-447.
41. Abd-Elhady, M., Rind, C., Wijers, J., Steenhoven, A., Bramer, E., and van der Meer, Th.H. Minimum gas speed in heat exchangers to avoid particulate flowing. *International Journal of Heat and Mass Transfer.* Vol. 47 (2004) pp. 3943-3955.
42. Walsh, P. Fouling of Convection Heat Exchangers by Lignitic Coal Ash. *Energy & Fuels* 1992, pp. 709-715.
43. Lee, B.E., Fletcher, A.J., Shin, S.H. and Kwon, S.B. Computational study of fouling deposit due to surface-coated particles in coal-fired power utility boilers. *Fuel.* Vol. 81 (2002) pp. 2001-2008
44. Robinson, A., Buckley, S., and Baxter, L. Experimental Measurements of the Thermal Conductivity of Ash Deposits: Part 1. Measurement Technique. *Energy & Fuels.* Vol. 15 (2001) pp. 66-74.
45. Robinson, A., Buckley, S., Yang, N., and Baxter, L. Experimental Measurements of the Thermal Conductivity of Ash Deposits: Part 2. Effects of Sintering and Deposit Microstructure. *Energy & Fuels.* Vol. 15 (2001) pp. 75-784.
46. Anthony, E. and Granarstein, D. Sulfation phenomena in fluidized bed combustion systems. *Progress in Energy and Combustion Science.* Vol. 27 (2001) pp. 227-230.
47. Anthony, E., Iribane, A., and Iribane, J. A New Mechanism for FBC Agglomeration and Fouling in 100 Percent Firing of Petroleum Coke. *Journal of Energy Resources Technology.* Vol 119 (1997) pp. 55-61.
48. Skrifars, B., Hupa, M., and Anthony, E. Mechanism of Bed Material Agglomeration in a Petroleum Coke-fired Circulating Fluidized Bed Boiler. *Journal of Energy Resources Technology.* Vol. 120 (1998) pp. 215-218.
49. Anthony, E., Preto, F., Jia, L., and Iribane, J. Agglomeration and Fouling in Petroleum Coke-Fired FBC Boilers. *Journal of Energy Resources Technology.* Vol. 120 (1998) pp. 285-292.

## REFERENCES

---

50. Anthony, E., and Jia, L. Agglomeration and Strength Development of Deposits in CFBC Boilers Firing High-Sulphur Fuels. *Fuel*. Vol. 79 (2000) pp. 1993-1942.
51. Bohac, V., Gustavsson, M.K., Kubicar, L., and Gustafsson, S.E. "Parameter estimations for measurements of thermal transport properties with the hot disk thermal constants analyzer", *Review of Scientific Instruments*, 71 (6) (2000), pp. 2452-2455.
52. Gustafsson, S.E. "Transient plane source techniques for thermal conductivity and thermal diffusivity measurements of solid materials", *Review of Scientific Instruments / American Institute of Physics*, 62 (3) (1991), pp. 797-804.
53. Anis-ur-Rehman, M. and Maqsood, A. "Measurement of Thermal Transport Properties with an Improved Transient Plane Source Technique", *International Journal of Thermophysics*, 24 (3) (2003), pp. 867-883.
54. Blumm, J. "Measuring Thermal Conductivity", *Ceramic Industry*, 152 (6) (2002), pp. 53-59.
55. Parker, W.J., Jenkins, R.J., Butler, C.P., and Abbott, G.L., "A Flash Method of Determining Thermal Diffusivity, Heat Capacity, and Thermal Conductivity", *Journal of Applied Physics*, 32 (9), 1961, pp. 1679-1684.
56. Abdul Abas, R. "Experimental Studies of Thermal Diffusivities Concerning Some Industrially Important Systems", KTH, Materials Science and Engineering Doctoral thesis, 2006
57. Nurminen, E. and Sun, S. "Thermal Transport properties of Copper Flash Smelting Flue Dust". In: Warner, A., Newman, C., Vahed, A., George, D., Mackay, P., and Warczok, A. (eds.) *The Carlos Diaz Symposium on Pyrometallurgy*. Vol. III, Book 2. Montreal, Canada, CIM pp. 589-596, 2007.
58. Nurminen, E. and Sun, S. "Thermal Diffusivity of Copper Flash Smelting Flue Dust" In: *GDMB Proceedings of the European Metallurgical Conference EMC 2007 Vol. 1 Copper, Sustainable Technologies/Sustainability in Non-Ferrous Metals Production, Waste Effluent Treatment/Biohydrometallurgical Applications*. Clausthal-Zellerfeld, Germany, pp. 135-143, 2007.
59. Nurminen, E., Rouvinen, M., and Järvi, J. "Thermal conductivity of copper flash smelting flue dust" In: Kongoli, F. and Reddy, R.G. (eds.) *Sohn International Symposium 2006 TMS (The Minerals, Metals & Materials Society) Warrendale, USA*, pp. 591-597, 2006.
60. Nurminen, E., Stykki, L., Fagerlund, K., and Taskinen, P. "Thermal conductivity of copper flash smelting flue dust". In: Schlesinger, M. (ed.) *EPD Congress 2005 Edited TMS (The Minerals, Metals & Materials Society), Warrendale, USA*, pp. 429-436, 2005.
61. Hurley, J., Nowok, J., Bieber, A., and Dockter, B. Strength Development at Low Temperatures in Coal Ash Deposits. *Progress in Energy Combustion Science*. Vol. 24. 1998 pp. 513-521.

62. Ranki-Kilpinen, T. Sulphation of cuprous and cupric oxide dusts and heterogeneous copper matte particles in simulated flash smelting heat recovery boiler conditions. Doctoral Thesis Helsinki University of Technology Doctoral Theses in Materials and Earth Sciences. Espoo 2004. p. 55.
63. Ranki-Kilpinen, T., Peuraniemi, E., and Jokilaakso, A., "Sulphation of Synthetic Flue Dust Particles in SO<sub>2</sub>-O<sub>2</sub>-N<sub>2</sub> Atmosphere." In: Kaiura, G., Pickles, C., Utigard, T., and Vhed A. (eds.) Fundamentals of Metallurgical Processing. Proceedings of James M. Toguri Symposium. CIM, pp. 193-206. 2000.
64. Ranki-Kilpinen, T., Peuraniemi, E., and Mäkinen, M. "Sulphation of Cuprous Oxide in SO<sub>2</sub>-rich Atmospheres". In: Stephens, R.L. and Sohn, H.Y. (eds.) Sulfite Smelting 2002, The Minerals, Metals & Materials Society, Warrendale, USA, pp. 261-271, 2002.
65. Laubitz, M. Thermal Conductivity of Powders. Canadian Journal of Physics. Vol. 37 (1959). pp. 798-808.
66. Perry, R. and Green, D. Perry's Chemical Engineering Handbook. 6<sup>th</sup> edition. McGraw-Hill Singapore 1984. pp. 3-247.
67. Roine A. HSC Chemistry 6.0. ISBN-13: 978-952-9507-12-2. Outotec Research Oy.
68. Kruskopf, A., Tool for calculating the heat transfer of the flash smelting process in a heat recovery boiler's convection section. Master's Thesis, Helsinki University of Technology, Espoo 2006, 77p. (in Finnish)